UNIVERSITY OF CASSINO AND SOUTHERN LAZIO

DEPARTMENT OF ELECTRICAL AND INFORMATION ENGINEERING

Radar sensing and communication aided by reconfigurable intelligent surfaces

---

A thesis submitted in fulfillment of the requirements
for the degree of *Doctor of Philosophy* in
Electrical and Information Engineering

January 2026

SUPERVISORS:
Prof. Luca VENTURINO
Prof. Emanuele GROSSI

AUTHOR:
Hedieh TAREMIZADEH

UNIVERSITÀ DEGLI STUDI DI CASSINO E DEL LAZIO MERIDIONALE

CORSO DI DOTTORATO IN METODI, MODELLI E TECNOLOGIE PER L'INGEGNERIA

Date: January 15, 2026

Author: **Hedieh TAREMIZADEH**

Title: **Radar sensing and communication aided by reconfigurable intelligent surfaces**

Department: **DIPARTIMENTO DI INGEGNERIA ELETTRICA E DELL'INFORMAZIONE**

Degree: **PHILOSOPHIAE DOCTOR**

Acknowledgements

I would like to express my sincere thanks to both of my supervisors, Prof. Luca Venturino and Prof. Emanuele Grossi, for their continuous support, encouragement, and valuable feedback during these three years. Their guidance was helpful at every stage of the research process. I am especially grateful to Prof. Venturino, whose expertise, patience, and belief in me helped me stay focused and motivated during the more challenging moments. His dedication and availability made a significant difference, and I truly appreciate the time and effort he generously devoted to my work.

I would also like to thank Prof. Fabrizio Marignetti, for his guidance, support, and kind approach throughout my academic journey.

A heartfelt thank you to Dr. Laura Morone for her invaluable assistance with residency and administrative matters, and for her unfailing kindness.

I would like to thank my family for being part of this journey and for their patience.

I am also thankful to my friends, whose encouragement and good company helped me stay balanced and positive along the way. A special thank you to Elisa Iannarelli, whose support, empathy, and kind presence during both the difficult and joyful times meant more to me than words can say. Her friendship gave me strength when I needed it most, and I will always remain deeply grateful.

Abstract

As wireless communication systems evolve toward the sixth generation (6G), there is a growing need for reliable high-speed connectivity, accurate sensing, and intelligent network adaptability. Meeting these demands introduces several challenges, especially at higher frequency bands, where signal attenuation and limited coverage become significant obstacles. Reconfigurable Intelligent Surface (RIS) have emerged as a promising solution to address these limitations by enabling programmable control over the wireless propagation environment. By adjusting the phase, amplitude, and direction of electromagnetic waves, RIS can improve coverage, enhance link performance, and support new functionalities such as sensing and localization.

This thesis investigates the design and application of advanced RIS architectures, with a focus on low-complexity systems that enhance sensing capabilities in 6G networks. Both active and passive RIS technologies are explored and evaluated in terms of their ability to support radar detection, target tracking, and communication tasks under practical constraints.

The first part of the study focuses on a monostatic radar system assisted by an active RIS. The amplification provided by the RIS helps mitigate path loss in indirect propagation paths. A dual-path signal model is developed, and joint detection and localization are performed using a Generalized Likelihood Ratio Test (GLRT). Simulation results show clear

improvements over passive RIS configurations.

The second part presents a pulse-Doppler radar system using a Simultaneous Transmitting and Reflecting Reconfigurable Intelligent Surface (STAR-RIS). This architecture enables sensing in both reflective and transmissive directions using collocated receive antennas. Direction-dependent slow-time modulation is applied to distinguish echoes from each side, and a model selection method based on the Generalized Information Criterion (GIC) is used for target detection and velocity estimation. Both simultaneous and sequential scanning strategies are evaluated in terms of performance and complexity.

The final part introduces a radar-centric Integrated Sensing And Communication (ISAC) transceiver, combining a passive STAR-RIS with a single-channel radar receiver using a Passive Electronically Scanned Array (PESA). Through joint space-time coding and beamforming design, the system supports transmit sensing and receive data transmission while maintaining low implementation complexity and minimal interference between functions.

These three contributions demonstrate how RIS technology, including active and STAR-RIS configurations, can significantly enhance the functionality, efficiency, and adaptability of future wireless systems. The proposed architectures offer practical and scalable solutions for next-generation networks, particularly in power- and hardware-constrained environments.

Contents

List of Figures

List of Tables

List of Abbreviations

6G	Sixth-Generation
BER	Bit Error Rate
BS	Base Station
CPI	Coherent Processing Interval
CSI	Channel State Information
ES	Energy Splitting
GIC	Generalized Information Criterion
GLRT	Generalized Likelihood Ratio Test
HRIS	Hybrid Reconfigurable Intelligent Surface
IoT	Internet of Things
ISAC	Integrated Sensing And Communication
MIMO	Multiple-Input Multiple-Output
mmWave	Millimeter-Wave
MS	Mode Switching
NCR	Network-Controlled Repeater
PAE	Power-Added Efficiency
PD	Probability of Detection
PESA	Passive Electronically Scanned Array
PFA	Probability of False Alarm
PRI	Pulse Repetition Interval
PSD	Power Spectral Density

RCS	Radar Cross-Section
RF	Radio Frequency
RIS	Reconfigurable Intelligent Surface
RMSE	Root Mean Square Error
SNR	Signal to Noise Ratio
STAR-RIS	Simultaneous Transmitting and Reflecting Reconfigurable Intelligent Surface
TS	Time Switching
UAV	Unmanned Aerial Vehicle

Notation

$\boldsymbol{A}$	Arbitrary matrix
$\boldsymbol{a}$	Arbitrary column vector
$[\boldsymbol{a}]_{m:n}$	Subvector of $\boldsymbol{a}$ containing entries from position m to n
$[\boldsymbol{A}]_{i,j}$	Entry in the i-th row and j-th column of $\boldsymbol{A}$
$[\boldsymbol{A}_1 \ \cdots \ \boldsymbol{A}_n]$	Horizontal concatenations of $\boldsymbol{A}_1, \ldots, \boldsymbol{A}_n$
$[\boldsymbol{A}_1; \ \cdots \ ; \boldsymbol{A}_n]$	Vertical concatenations of $\boldsymbol{A}_1, \ldots, \boldsymbol{A}_n$
i	Imaginary unit
$\mathbb{R}$	Field of real numbers
$\mathbb{C}$	Field of complex numbers
$\mathcal{CN}$	Circularly symmetrical complex Gaussian distribution
$\Re(\cdot)$	Real part
$(\cdot)^*$	Conjugate
$(\cdot)^{-1}$	Inverse
$(\cdot)^{\mathsf{T}}$	Transpose
$(\cdot)^{\mathsf{H}}$	Conjugate transpose
$\lvert\cdot\rvert$	Absolute value
$\lVert\cdot\rVert_F$	Frobenius norm
$\lVert\cdot\rVert_p$	p-norm
$\lVert\cdot\rVert_\infty$	∞-norm
$\mathbb{E}[\cdot]$	Statistical expectation
$diag\{\cdot\}$	Diagonal matrix with $\{\cdot\}$ on the main diagonal
$\mathrm{Tr}(\cdot)$	Trace
$\boldsymbol{I}_M$	$M \times M$ identity matrix
$\boldsymbol{0}_M$	M-dimensional vector with all zero entries
$\odot$	Schur product product operator
$\otimes$	Kronecker product operator
$*$	Convolution operator
x^+	Equal to x, if $x \geq 0$, and to 0, otherwise
$\mathrm{card}(\mathcal{A})$	Cardinality of the set $\mathcal{A}$
$\mathbb{1}_{\mathcal{A}}$	Indicator function of the condition $\mathcal{A}$, i.e., $\mathbb{1}_{\mathcal{A}} = 1$, if $\mathcal{A}$ is verified, and $\mathbb{1}_{\mathcal{A}} = 0$, otherwise

Dedicated to mothers pursuing research,
with gratitude to those who support them

Chapter 1

Introduction

The evolution of wireless communication systems has progressed from the first generation (1G) to the current fifth generation (5G), with each generation bringing significant technological breakthroughs and expanding the scope of supported services. The 1G networks of the 1980s provided basic analog voice connectivity. The advent of 2G introduced digital communication, enabling services such as SMS and improved voice quality. The 3G era marked the beginning of mobile multimedia and broadband services, while 4G significantly enhanced data rates and latency, enabling applications such as high-definition video streaming and mobile cloud computing. The ongoing deployment of 5G networks brings three key communication features: enhanced mobile broadband, ultra-reliable low-latency communication, and massive machine-type communication. These capabilities are considered foundational for use cases such as industrial automation, telemedicine, connected vehicles, and smart cities. An overview of the major features and milestones across generations is illustrated in Fig. 1.1.

With the limitations of 5G becoming increasingly evident in addressing the requirements of future use cases, Sixth-Generation (6G) wireless networks are envisioned as a complete transformation in the way wireless

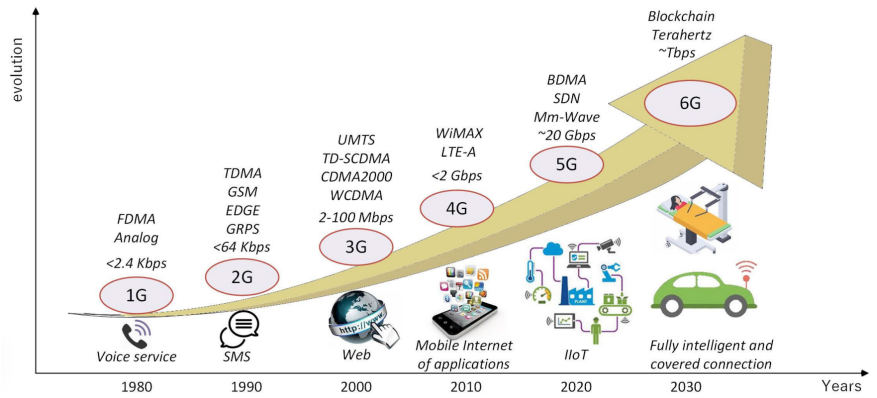

FIGURE 1.1: The evolution of wireless networks [1].

systems are conceptualized and deployed. Rather than merely improving speed or latency, 6G aims to integrate communication with sensing, computing, localization, and environmental awareness to create intelligent, adaptive, and responsive network environments [2], [3]. This transformation is expected to support a wide array of emerging applications, such as autonomous vehicles, large-scale drone operations, smart factories, immersive extended reality, and interconnected smart cities [4].

Development efforts toward 6G are currently guided by a structured research and standardization roadmap that follows the typical evolution cycle of previous mobile generations. The first phase, running from 2020 to 2025, focuses on fundamental research and technology exploration in key areas including ISAC, artificial intelligence embedded at the network core, use of terahertz frequencies, non-terrestrial network integration, and

sustainable system design. Between 2025 and 2028, international standardization organizations and industry alliances are expected to conduct large-scale trials, establish reference architectures, and begin formulating pre-standard technical frameworks. Formal standardization activities are anticipated to occur between 2028 and 2030 under initiatives such as the ITU-R IMT-2030 program and 3GPP Releases 21 and 22, which will define unified technical specifications and spectrum strategies. Following these efforts, commercial deployment is expected to begin after 2030, enabling a broader shift from connecting people and devices to enabling highly distributed and automated systems driven by connected intelligence.

Achieving such an ambitious vision presents several technological challenges. Among the most critical are the need to ensure robust and reliable connectivity in complex environments, enhance spectral and energy efficiency across diverse deployment scenarios, and support high-precision sensing and localization at scale [5]. Overcoming these challenges requires a reimagining of traditional radio access network designs and the adoption of novel physical-layer technologies capable of dynamically adapting to changing operational and environmental conditions.

One particularly promising technology that has emerged in this context is the RIS. RIS enables fine-grained control over the wireless propagation environment by intelligently modifying how electromagnetic signals are reflected, refracted, or scattered. This allows wireless networks to actively shape signal paths to extend coverage in non-line-of-sight conditions, improve energy and spectral efficiency through passive or hybrid beamforming, and aid in precise localization by offering additional signal propagation paths. These capabilities make RIS a strong candidate to support the key performance requirements of 6G networks [2].

FIGURE 1.2: Photograph of a practical reconfigurable intelligent surface prototype.

Given its potential to address some of the most pressing challenges in next-generation wireless systems, RIS is expected to play an essential role in building intelligent, sustainable, and context-aware 6G architectures. A more detailed discussion on the principles, functionality, and applications of RIS will be provided in Section 1.1.

1.1 Reconfigurable intelligent surface

An RIS is a manmade two-dimensional surface, which is equipped with a large number of low-cost passive elements. Each unit cell is designed to manipulate incident electromagnetic waves by dynamically adjusting its response parameters, such as phase shift and amplitude, through electronic tuning. This control enables the RIS to shape and steer electromagnetic wavefronts to achieve desired propagation effects. The physical structure of an RIS typically consists of patterned conductive elements on a dielectric substrate. Integrated within each unit cell are tunable components, commonly PIN diodes or varactor diodes, connected to a control

circuit that programs the surface in real time. Unlike traditional active devices, the RIS itself does not generate or amplify signals but reshapes existing waves with minimal power consumption. Fig. 1.2 shows a photograph of a RIS prototype, highlighting the dense arrangement of unit cells and embedded tuning elements. While conventional RIS architectures typically rely on discrete reflective elements such as metallic patches loaded with PIN diodes or varactors [6], recent advancements have led to the adoption of metasurface-based RIS designs that offer significantly enhanced wave manipulation capabilities [7]. Metasurfaces are engineered surfaces composed of subwavelength-scale unit cells, often referred to as meta-atoms, which can precisely control the phase, amplitude, and polarization of incident electromagnetic waves at a much finer granularity than traditional approaches [8]. Unlike conventional RIS, which usually provides limited binary or quantized phase shifts due to hardware constraints, metasurfaces can achieve more continuous and adaptable control, enabling functionalities such as anomalous reflection, dynamic beamforming, and polarization conversion. The improved configurability and control make metasurface-based RIS a highly promising solution for future wireless communication systems, especially in the development of 6G networks where intelligent and energy-efficient management of the radio environment will be essential [9]. Additionally, metasurfaces can be fabricated using advanced nanofabrication or 3D printing techniques, allowing for compact, lightweight, and seamlessly integrated designs tailored for smart surfaces across various frequency bands, including Millimeter-Wave (mmWave) and terahertz. As the field moves toward programmable wireless environments and holographic Multiple-Input Multiple-Output (MIMO) systems, metasurface-enabled RIS is positioned as a central technology in enabling

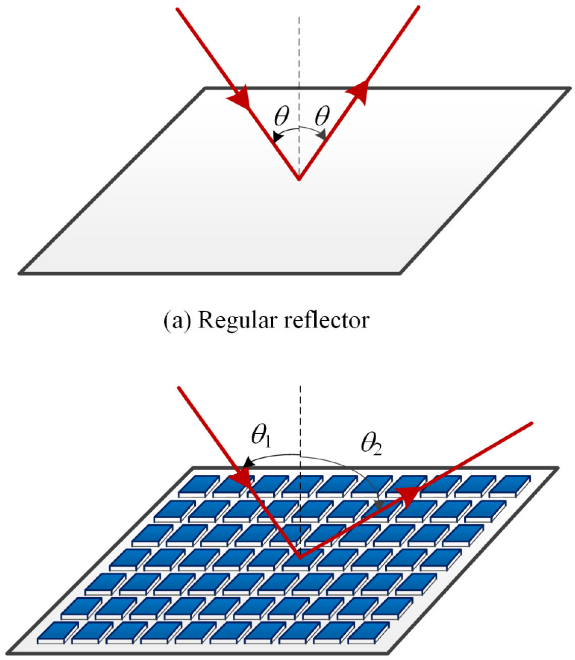

(a) Regular reflector

(b) Reconfigurable intelligent surface

FIGURE 1.3: Regular reflector vs RIS [11].

the next generation of reconfigurable and adaptive communication infrastructures [10].

We are interested in RISs because they offer several key advantages for next-generation wireless networks. They enable non-line-of-sight links to overcome blockages at mmWave frequencies and extend signal coverage through beamforming gains and, for active RISs, additional amplification gains. Moreover, by reusing existing signals, RISs help reduce electromagnetic pollution, while precise control of redirected waves allows for effective interference mitigation.

1.1.1 Operating principle of RIS

The basic idea of RIS is to leverage a large number of passive or nearly-passive reflecting elements that can independently adjust the phase and/or amplitude of the incident electromagnetic wave. By carefully controlling these parameters, RIS can shape the wireless channel in a desirable way, such as enhancing the received signal power, suppressing interference, or enabling new functionalities like joint communication and sensing. To better illustrate this concept, Fig. 1.3 compares the behavior of a traditional reflector and a reconfigurable intelligent surface. In a conventional reflector, the incident and reflected signals strictly follow Snell's law, which states that the angle of incidence equals the angle of reflection. In contrast, RIS introduces programmable control over the reflection process, enabling the reflected wave to be directed toward arbitrary directions, regardless of the incident angle.

To provide a clearer intuition of how RIS operates, let us first consider the effect of a single RIS element. As shown in Fig. 1.4, the wireless link consists of a direct path (blue line) between the Base Station (BS) and the user, and an indirect path (black line). where:

- $s(t)$ is incoming signal;
- $y(t)$ is received signal;
- α_1 and ϕ_1 are the attenuation factor and phase shift of the direct path;
- α_2 and ϕ_2 are the attenuation factor and phase shift of the indirect path;
- θ is controllable phase shift introduced by an RIS element.

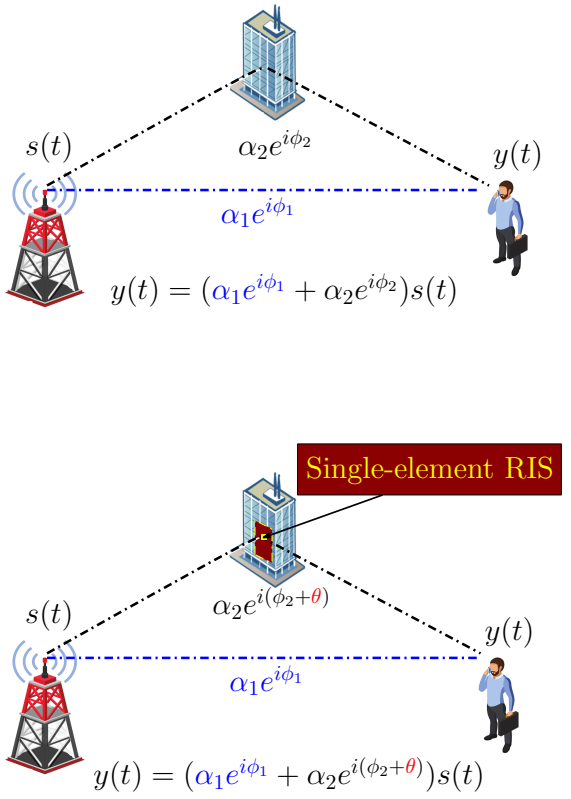

FIGURE 1.4: Single-element RIS introducing a controllable phase shift θ on the reflected path to enhance the received signal.

Without RIS, the phase of the indirect path is fixed by the geometry and material properties of the wall, and thus cannot be controlled. If, instead of the wall, we place a single RIS element, this element can impose an additional controllable phase shift θ on the indirect path. By properly tuning θ, the phase of the reflected signal can be aligned with that of the direct path, enabling constructive combination at the user side. This simple example illustrates the fundamental capability of RIS to reconfigure the wireless propagation environment through programmable phase control.

1.1.2 Types of RIS and their signal models

RISs can be classified based on the element type and the mode of signal propagation. In terms of element type, RISs are passive, where elements control the incident signals without amplification, or active, where elements can additionally amplify the signals. With respect to signal propagation, RISs are categorized as reflecting-only surfaces, which fully reflect incident signals; transmitting-only surfaces, which fully transmit signals; or STAR-RIS, which split the incident signals between reflection and transmission.

Passive RIS

Each element of the RIS can adjust the phase shift and attenuate the amplitude of the incident signal. Passive RISs do not introduce additional energy into the system, making them energy-efficient but limited in compensating for path loss. Basic signal model for a passive reflecting RIS can be written as:

$$y_n = a_n e^{j\theta_n} s_n, \tag{1.1}$$

where

- y_n is the signal reflected by the n-th RIS element;
- $a_n \in [0, 1]$ accounts for the possible signal absorption;
- $\theta_n \in [0, 2\pi)$ is the tunable phase response;
- s_n is the incoming signal.

The response of each RIS element can be dynamically adjusted using variable loads, delay lines, or phase shifters. It should be noted that the RIS-assisted path experiences a multiplicative path loss; therefore, to minimize

the overall path loss, the RIS is ideally positioned close to either the transmitter or the receiver.

Active RIS

Each element includes an active load, enabling not only phase control but also signal amplification. This allows active RISs to boost the incident signal and extend coverage, at the cost of higher power consumption and complex implementation. Basic signal model for a active reflecting RIS can be written as:

$$y_n = a_n e^{j\theta_n} \left(s_n + z_n \right), \tag{1.2}$$

where

- y_n is the signal reflected by the n-th RIS element;
- $a_n > 1$ accounts for the amplification gain;
- $\theta_n \in [0, 2\pi)$ is the tunable phase response;
- s_n is the incoming signal;
- z_n is the internal RIS noise (amplified together with the useful signal).

Here is the comparison of active and passive RIS in Fig. 1.5

STAR RIS

A major limitation of conventional RIS is its one-sided coverage, as it can only reflect or transmit the incident electromagnetic waves toward one half-space. To overcome this drawback, the concept of STAR-RIS has been introduced. A STAR-RIS can split the incident signal into transmitted and reflected components, providing independent control over both to enhance

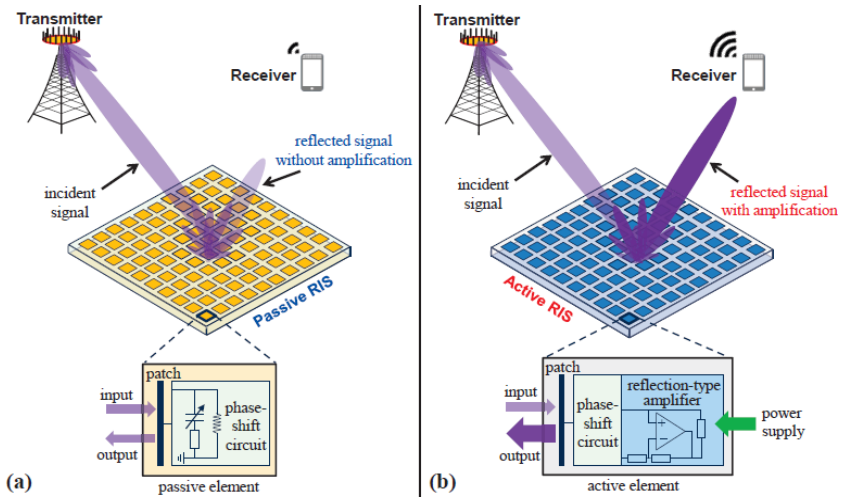

FIGURE 1.5: Passive vs active RIS [12].

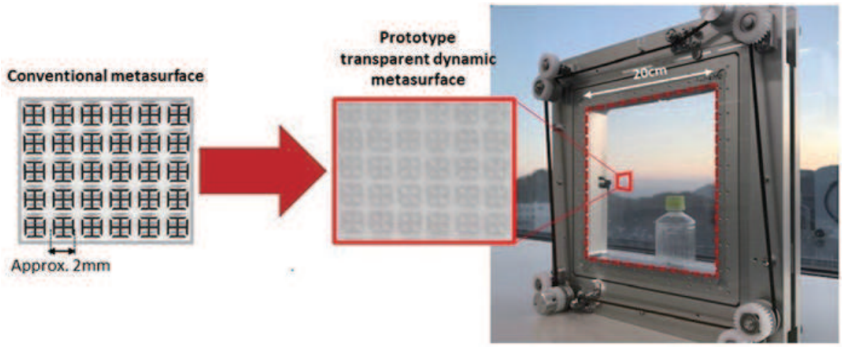

FIGURE 1.6: Prototype of a STAR-RIS [13].

coverage and flexibility in network design. This dual functionality extends the coverage region and making STAR-RIS a key enabler for 6G applications such as extended coverage, joint communication and sensing, and user-centric service provisioning. A prototype implementation of STAR-RIS is shown in Fig. 1.6, demonstrating its feasibility and practical hardware structure.

Basic signal model for a passive STAR-RIS element can be written as:

$$y_{\mathrm{tr},n} = a_{\mathrm{tr},n} e^{j\theta_{\mathrm{tr},n}}, \tag{1.3a}$$

$$y_{\mathrm{re},n} = a_{\mathrm{re},n} e^{j\theta_{\mathrm{re},n}}, \tag{1.3b}$$

where

- $y_{\mathrm{tr},n}$ and $y_{\mathrm{re},n}$ are the signals transmitted and reflected by the n-th STAR-RIS element;
- $a_{\mathrm{tr},n} \in [0,1]$ accounts for the amplification gain in the transmissive half-space;
- $\theta_{\mathrm{tr},n} \in [0, 2\pi)$ is the tunable phase response in the transmissive half-space;
- $a_{\mathrm{re},n} \in [0,1]$ accounts for the amplification gain in the reflective half-space;
- $\theta_{\mathrm{re},n} \in [0, 2\pi)$ is the tunable phase response in the reflective half-space;
- s_n is the incoming signal.

Operating modes of STAR-RIS

One of the key features that differentiates STAR-RIS from conventional RIS is its ability to simultaneously transmit and reflect incident signals. This dual functionality enables the STAR-RIS to provide coverage in both sides of the surface, thereby significantly increasing its flexibility and effectiveness in next-generation wireless networks. Depending on how the transmission and reflection coefficients of the elements are configured, three fundamental operating modes can be defined:

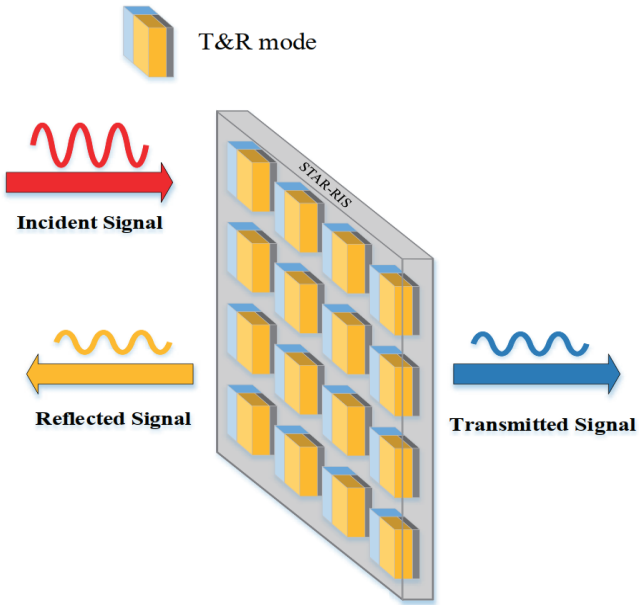

FIGURE 1.7: Energy splitting [13].

- **Energy splitting (ES) mode:** Each RIS element simultaneously reflects and transmits the incident signal by splitting its energy into two portions, typically controlled by adjustable reflection and transmission coefficients. This mode is highly flexible, as it allows a fine-grained trade-off between coverage in the reflection and transmission regions (see Fig. 1.7).

- **Mode switching (MS) mode:** The elements are partitioned into two groups, where one group operates in pure reflection mode and the other in pure transmission mode. This configuration simplifies implementation and reduces hardware complexity, but offers less flexibility compared to ES mode (see Fig. 1.8).

- **Time switching (TS) mode:** All elements alternate between reflection and transmission over different time slots. This ensures full energy

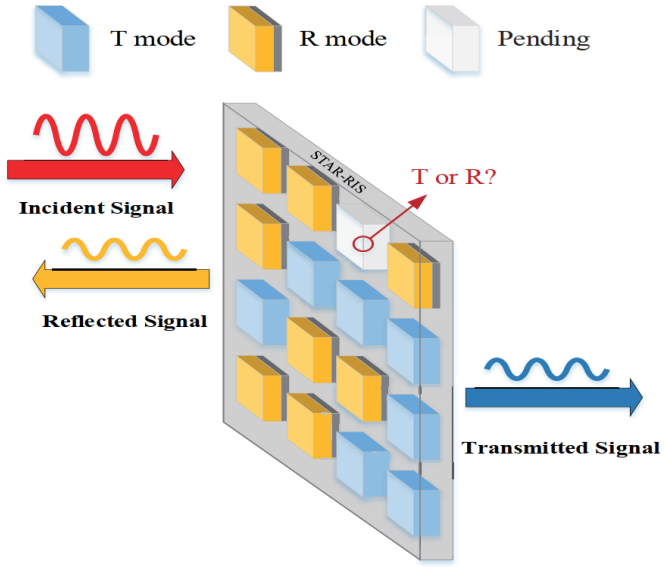

FIGURE 1.8: Mode switching [13].

utilization in either direction at a given time, but introduces latency due to switching (see Fig. 1.9).

1.1.3 Applications of RIS in wireless networks

The potential applications of RISs in future wireless systems are extremely diverse, ranging from enhanced coverage and connectivity to improved security, sensing, and localization. Owing to their ability to dynamically reconfigure the radio environment, RIS can be deployed in a variety of contexts. An overview of key RIS-enabled application scenarios is illustrated in Fig. 1.10.

Unmanned aerial vehicle networks

For Unmanned Aerial Vehicle (UAV) communications, maintaining strong and stable links is often energy-intensive, since drones may need to reposition frequently. RISs can help by forming controllable virtual line-of-sight

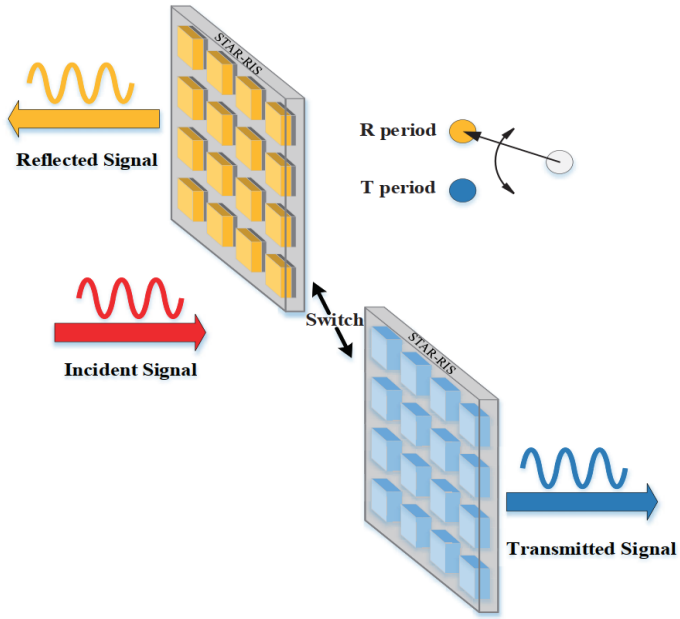

FIGURE 1.9: Time switching [13].

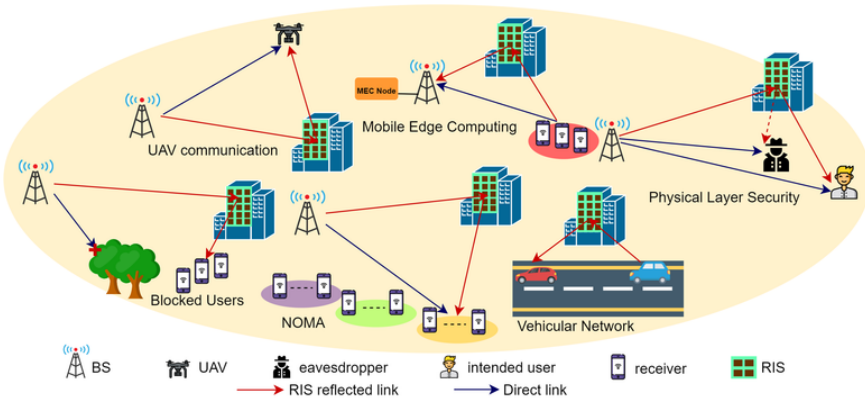

FIGURE 1.10: Emerging applications of RIS for 6G wireless networks [14].

links, which reduces the need for UAVs to constantly move for better coverage. This leads to lower energy consumption and longer flight times. RIS-assisted UAV communication is particularly useful for time-sensitive

applications such as search-and-rescue missions, environmental monitoring, and temporary network deployments in remote areas [15].

Vehicular and transportation systems

Reliable connectivity is crucial for connected and autonomous vehicles, but signals are easily blocked by buildings, trucks, or other vehicles. RISs can be integrated into roadside structures, billboards, or even vehicles themselves to guide signals around obstacles and suppress unwanted interference. By providing a more predictable and programmable channel, RISs make vehicle-to-everything communication more robust, which is a key requirement for road safety, collision avoidance, and real-time traffic management in future intelligent transportation systems [16].

Internet of things and smart environments

Internet of Things (IoT) applications often involve a massive number of low-power devices, such as sensors in agriculture, industry, or smart homes. RISs can help by enhancing the quality of weak links, mitigating interference, and even enabling wireless power transfer. This means that sensors and devices can operate more reliably while consuming less energy. In large-scale deployments such as smart factories or farms, RISs provide a practical way to improve connectivity without the need for costly infrastructure upgrades [17], [18].

Physical layer security

One of the appealing features of RISs is their ability to control how signals propagate in space. This can be exploited to strengthen the received signal at a legitimate user while simultaneously weakening or cancelling it in the

direction of a potential eavesdropper. Such an approach provides an additional layer of security at the physical layer, complementing traditional encryption. RIS-based security solutions are particularly attractive in settings where confidentiality is paramount, such as healthcare systems, finance, or defense communications [19].

RIS-based transmitters and modulation

Beyond acting as a passive channel enhancer, RISs can themselves be part of the transmission process. By configuring their unit cells appropriately, RISs can impose modulations such as phase-shift keying directly on the reflected signal. This opens up the possibility of very low-cost and low-power transmitters, where the conventional burden of modulation is shifted from the transmitter hardware to the surface itself. Such designs are still at an early stage, but they illustrate the broader vision of RISs as active players in the communication chain, not just passive reflectors [20], [21], [22].

Localization and sensing

RISs are expected to play a key role in advancing localization and sensing capabilities in next-generation wireless networks. As 6G moves toward integrating communication and environmental awareness, these functionalities are anticipated to become core features of the network infrastructure. By intelligently controlling how electromagnetic waves are reflected and scattered, RISs can enhance both the coverage and precision of localization and sensing in complex indoor and outdoor environments [23].

In the context of localization, RISs can act as artificial landmarks or passive virtual anchors, enhancing position and orientation estimation in environments where conventional Global Navigation Satellite Systems or

line-of-sight paths are unavailable. This includes industrial sites, underground spaces, and dense urban environments. By engineering controllable multipath components, RISs improve classical positioning metrics such as angle-of-arrival, time-of-arrival, and time-difference-of-arrival, leading to enhanced estimation accuracy. Studies have shown that centimeter-level localization can be achieved under such conditions [24], [25].

Beyond localization, RISs also contribute to radar-based sensing tasks, such as object detection and environment mapping. By reshaping signal reflections through passive beamforming, RISs enable tracking in non-line-of-sight conditions, including scenarios with obstacles like walls or foliage. They improve observability by introducing additional reflection paths, effectively augmenting radar sensing with higher spatial resolution and increased signal diversity.

Despite these promising benefits, several practical limitations remain. Passive RISs inherently suffer from multiplicative path loss, which can significantly weaken reflected signals if the surface is not optimally positioned. Additionally, most conventional RIS designs support only single-sided reflection, limiting their usefulness in dynamic or multi-user scenarios. To address these challenges, advanced hardware architectures have been proposed. Active RISs integrate low-power amplifiers to boost signal reflections and compensate for path loss [12], while STAR-RISs enable simultaneous control over reflections and transmissions, offering bidirectional coverage and improved adaptability in complex sensing environments [13].

Integrated sensing and communication

ISAC is an emerging concept that aims to unify wireless communication and sensing into a common framework using shared hardware, spectrum,

and waveforms. Instead of treating sensing and communication as separate functions, ISAC systems combine the two. RIS fits naturally into this concept by serving both as a beamforming tool for communication and as a reflective surface for directing sensing signals. For instance, an RIS can be used to send a communication signal to a nearby user while simultaneously reflecting part of that signal toward a target for sensing or tracking purposes. This dual use greatly improves spectral efficiency and hardware utilization, especially in 6G systems where space, power, and bandwidth are limited [17], [26], [27].

1.2 Motivation and research challenges

With the foundational principles and designs of RISs elucidated in previous sections, this part of the thesis focuses on the specific research gaps related to their application in sensing and ISAC systems. As RIS technologies evolve from passive reflectors to more sophisticated active and STAR-RIS architectures, their potential role extends beyond channel enhancement to becoming central components in configurable radar systems and dual-purpose ISAC platforms.

Despite substantial progress, several critical technical limitations, trade-offs, and architectural constraints remain unaddressed in the context of RIS-enabled ISAC. Challenges such as signal attenuation in passive configurations, limited directional coverage in radar applications, and system complexity in joint sensing-communication design continue to hinder practical deployment. These limitations shape the core research questions addressed in this thesis, which progressively investigates and develops active RIS, STAR-RIS-based sensing, and ultimately radar-centric ISAC architectures tailored for low-complexity, next-generation wireless systems.

RIS deployment constraints and path loss

Passive RISs are often considered for their low power consumption and hardware simplicity. However, the signal attenuation along the cascaded source-RIS-destination path introduces multiplicative path loss that significantly degrades performance, particularly when the RIS is not optimally positioned near the transmitter or receiver. Many practical deployments do not allow such ideal placement, especially in dynamically changing or constrained environments.

To alleviate this, active RISs incorporate reflection amplifiers to overcome path loss and extend coverage. Nevertheless, active designs introduce new challenges, such as:

- Increased energy consumption and hardware complexity;
- Non-negligible thermal and noise emissions;
- The need for gain control and stability in full-duplex amplification.

Moreover, many existing system models and testbeds still assume ideal gain alignment or neglect hardware impairments, making real-world adoption more complicated.

Limitations of RIS-assisted radar sensing

RISs hold appeal for radar applications, especially monostatic or bistatic setups. However, their sensing capabilities are typically limited by:

- One-sided beamforming (applicable to reflective-only RISs);
- Restricted angular coverage and spatial diversity;
- High reliance on perfectly aligned echo paths or static environments.

Most radar work involving RISs still assumes:

- Ideal propagation;
- Dedicated wide-aperture receivers;
- Discrete signal processing chains for different echo paths.

These setups, while viable in theory, fail to scale down to low-complexity, single-channel radar receivers, and lack flexibility in terms of non-line-of-sight coverage or echo diversity. Additionally, real deployment scenarios often involve multipath-rich or clutter-heavy environments, where the limited angular resolution of passive RIS configurations becomes a bottleneck.

Gaps in practical ISAC with STAR-RIS architectures

ISAC promises a unified platform for data communication and environmental sensing. STAR-RIS architectures, which reflect and transmit simultaneously, seem well-aligned with ISAC goals. However, current STAR-RIS-based ISAC solutions often rely on idealized assumptions such as full Channel State Information (CSI) and perfect synchronization, which are rarely achievable in mobile or distributed environments. Additionally, these systems typically require multichannel digital transceivers, leading to high cost and power consumption, and are often designed with a communication-centric focus, making radar performance secondary or opportunistic.

Hardware constraints further complicate practical adoption. Limitations such as restricted switching speed, approximate phase control, and energy split losses make it difficult to directly apply conventional beamforming and signal processing strategies. As a result, STAR-RIS elements

must be carefully configured through joint design principles, rather than as simple extensions of existing communication frameworks.

Most importantly, there is a lack of unified, radar-centric, and low-complexity ISAC architectures that can bridge the gap between theoretical advances and real-world needs. An effective solution should satisfy several key criteria:

- Compatibility with low-complexity hardware (e.g., single-channel analog receivers, directional feeders);
- Dual-half-space coverage enabled by STAR-RIS;
- Joint waveform and beamforming design for both radar and communication tasks;
- Minimal reliance on CSI, synchronization, or iterative processing.

Designing such a system demands a radar-centric objective function, integrated spatial and temporal modulation, efficient processing at both radar and communication receivers, and careful management of trade-offs between detection reliability, angular resolution, transmission rate, and bit error rate.

The limitations outlined across RIS-assisted radar and ISAC systems reveal a clear gap between theoretical developments and practical, scalable implementations. Addressing these challenges calls for a design approach that balances performance, complexity, and hardware feasibility, particularly in dynamic, cluttered, or resource-constrained environments. This thesis responds to these needs through a sequence of progressively structured contributions, each aimed at overcoming specific barriers in the path toward an integrated, low-cost, radar-centric ISAC architecture. The following section presents these contributions in detail.

1.3 Thesis contributions

In response to the challenges outlined in the previous section, this thesis proposes a structured sequence of three contributions, each addressing specific limitations in the design of RIS-enabled sensing and integrated wireless systems. While the focus and architecture vary across contributions, they collectively aim to advance the development of low-complexity, RIS-assisted sensing and ISAC solutions. The primary contributions of the thesis, based on theoretical modeling and numerical simulations, are summarized below.

Active RIS-assisted radar for enhanced target detection and localization

The first contribution of this thesis, presented in Chapter 2, investigates an active RIS-enhanced monostatic radar system designed to mitigate the severe path loss associated with indirect propagation paths. Unlike conventional RIS-aided radar, where passive surfaces offer limited gain and require very specific placement, the proposed architecture incorporates active elements that amplify the reflected signal. This approach enables the reception of both direct and RIS-assisted echoes at a digital radar receiver, forming a virtual multistatic radar setup without the need for multiple Radio Frequency (RF) chains or separate receiver units.

A detailed signal model is developed to account for the dual-path structure, including independent delay and attenuation parameters for the direct and indirect returns. Based on this model, a GLRT is derived to jointly perform target detection and localization. The analysis further explores how

the RIS amplification gain and spatial placement influence detection performance and estimation accuracy. Additionally, by relaxing the typical architectural constraints found in bistatic systems, the proposed design enables a more compact and hardware-efficient radar implementation. The system's performance is validated through simulations, demonstrating tangible improvements in detection probability and localization accuracy when compared to passive RIS configurations.

STAR-RIS-based pulse-Doppler radars

The second contribution, detailed in Chapter 3, introduces a passive STAR-RIS-based pulse-Doppler radar architecture designed for detecting moving targets within both reflective and transmissive half-spaces. In this configuration, the STAR-RIS is co-located with a radar receiver and operates under a space-time modulation framework tailored to separate echoes originating from each half-space. To achieve this, the system employs direction-dependent slow-time coding across Pulse Repetition Interval (PRI).

Two distinct scanning protocols, simultaneous and sequential, are proposed to provide flexible coverage on both sides of the STAR-RIS while preserving system simplicity. Both schemes enable unambiguous association between detected echoes and their corresponding spatial domains, allowing the radar to operate with a single analog front-end and digital receiver chain. Target detection and radial velocity estimation tasks are performed using a model order selection approach based on the GIC, which accounts for clutter and noise effects. Through simulation studies, the system is shown to maintain effective sensing performance. This contribution demonstrates the practical feasibility of dual-domain radar sensing with minimal RF resources by leveraging programmable metasurfaces.

Radar-centric ISAC system using passive STAR-RIS

The third and final contribution of this thesis, detailed in Chapter 4, introduces a radar-centric ISAC transceiver architecture. This system integrates a passive STAR-RIS, a radar receiver equipped with a PESA and a single digital channel, forming a compact and efficient platform for joint sensing and communication in shared-spectrum environments. Unlike the fully digital phased array system described in Chapter 3, which relies on intensive digital processing, the system presented here prioritizes implementation simplicity, cost efficiency, and low power consumption. This is achieved by shifting system complexity into the analog and electromagnetic domains, enabling a more scalable and energy-efficient ISAC solution.

In this design, a directional analog feeder periodically illuminates the STAR-RIS with pulsed radar waveforms. The STAR-RIS applies space-time modulation to these pulses, enabling dynamic beam steering and signal encoding through programmable metasurface behavior. The joint design of the STAR-RIS spatial response and the radar receiver beamforming pattern allows targeted illumination and sensing in distinct directions on both sides of the STAR-RIS. This dual-sided coverage supports radar surveillance and user communication simultaneously, while effectively suppressing clutter and interference.

To support data transmission without dedicated communication waveforms, the system embeds dual-purpose time-domain codes into the radar pulses. These codes serve both as unique identifiers for radar targets (differentiating echoes from each side of the STAR-RIS) and as carriers of communication data for users. Two modulation schemes are proposed: one enabling simultaneous illumination and another supporting sequential scanning of the two sides, offering flexibility in managing directional coverage

and interference.

Performance evaluation covers both sensing and communication domains, including metrics such as Probability of Detection (PD), Root Mean Square Error (RMSE) in estimating target radial velocity, Bit Error Rate (BER), and transmission rate. The system design enables tunable trade-offs between radar and communication performance by adapting the STAR-RIS and radar PESA beampatterns, as well as by selecting appropriate time-domain encoding schemes. Notably, communication functionality is achieved with minimal degradation to radar performance.

This contribution establishes a scalable and dual-functional sensing platform tailored to the needs of intelligent infrastructure and autonomous systems, where spectrum efficiency, hardware simplicity, and adaptability are critical.

Chapter 2

Active RIS-Assisted Radar for Enhanced Target Detection and Localization

This chapter is based on article published in the *IEEE Signal Processing Letters*, 2023 [28].

2.1 Introduction

RISs are made of tunable elements that reflect the incident electromagnetic signal with a desired phase/amplitude adjustment without using a RF chain or introducing a processing delay. RISs can be either passive [29], [30], [31], [32], [33] or active [12], [34], [35] and allow to control the propagation channel from a source to a destination, thus providing additional degrees of freedom in the design of wireless systems [36], [37]; for example, they can be used to overcome the direct-path blockage or to boost the Signal to Noise Ratio (SNR) when a direct-path is present [38].

Passive RISs have been exploited in several applications, including joint wireless data and power transfer [39], interference mitigation [40], RIS-based modulation [41], ambient backscatter communication [42], user localization and mapping [23], and radar target detection [43], [44], [45], [46].

Since the source-RIS-destination link suffers from a multiplicative path loss, passive RISs can be of limited help if not properly positioned. A main finding is that they should be better placed close to the source or the destination; however, this may prevent exploiting spatial diversity or may not be feasible due to implementation constraints. These limitations can be overcome by resorting to active RISs, which inherit the same hardware structure and full-duplex operation of the passive counterpart, except that active (rather than passive) load impedances are employed to cover longer source-RIS and/or RIS-destination hops [12], [34], [35], [47]. Active RISs make use of reflection amplifiers, wherein the additional DC power provided by a biasing source is exploited to boost the RF impinging signal [48], [49], [50], [51]; remarkably, tunnel diode based reflection amplifiers only have a sub-mW DC power consumption. An active RIS is similar in spirit to a Network-Controlled Repeater (NCR), as both devices rely upon the amplify-and-forward concept [52], [53]: however, their different architectures pose unique challenges. Indeed, the RIS employs a single panel with amplifying and reflecting elements, whereby both the impinging and reflected waves must be in the same half-space [12], [34]. On the other hand, the NCR is made of two back-to-back analog arrays with a signal amplifier in between, whereby limiting the loop-back interference in a full-duplex operation may constrain the reciprocal orientation of the two panels [54], [55].

Leveraging the architecture proposed in [47], in this study we consider a monostatic radar that is equipped with a digital array and whose receiver is assisted by a widely-spaced active RIS. As shown in Fig. 2.1, the radar illuminates a given area and, in the presence of a target, receives two independent echoes, namely, the direct and the RIS-assisted (indirect) echo:

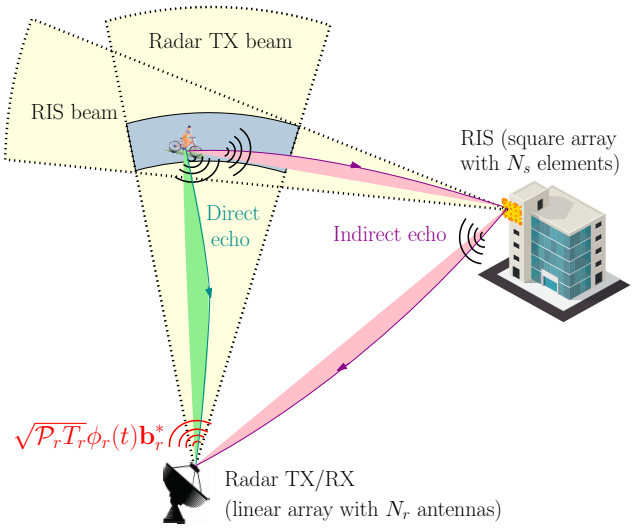

FIGURE 2.1: Graphical description of a monostatic radar and an active RIS assisting the receiver.

this system mimics a distributed multi-static radar; however, rather than having a second receiver with an additional RF processing chain, the RIS redirects the indirect echo towards the same receiver observing the direct echo. While [47] has only focused on target detection, our goal here is to configure the RIS and elaborate the received signal to jointly detect and localize a prospective target; in addition, we remove the assumption that the radar receiver has two separate antennas pointing towards the target and the RIS, respectively. Upon introducing a convenient signal model, we design the array gain factor of the radar transmitter and the RIS to uniformly cover the inspected region; then, the joint detection and localization problem is solved through a GLRT. Numerical examples are provided to assess the achievable performance and to elicit the impact of the RIS amplification gain and of the size of the inspected region.

The remainder of this chapter is organized as follows. Sec. 2.2 contains the system description. Sec. 2.3 illustrates the proposed system design.

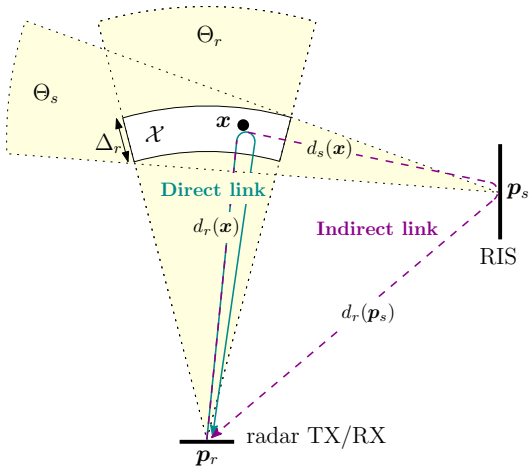

FIGURE 2.2: Considered architecture composed of a monostatic radar and an active RIS assisting the receiver.

Sec. 2.4 contains the numerical analysis. Finally, concluding remarks are given in Sec. 2.5.

2.2 System description

We consider a monostatic radar that employs a carrier wavelength λ, an average radiated power $\mathcal{P}_r$, a pulse repetition time T_r, and a uniform linear array with N_r elements spaced of δ_r. For simplicity, we assume a two-dimensional geometry, as shown in Fig. 2.2. The radar transmitter emits the baseband signal $\sqrt{\mathcal{P}_r T_r}\phi_r(t)\boldsymbol{b}_r^*$, where $\boldsymbol{b}_r \in \mathbb{C}^{N_r}$ is a unit-norm spatial beamformer and $\phi_r(t)$ is a unit-energy pulse with support $[0, \Phi_r]$ and bandwidth W_r. The radar receiver is assisted by an active RIS containing N_s elements arranged into a uniform square array with inter-element spacing δ_s along each axis. We denote by $\sqrt{B_s}\boldsymbol{b}_s^* \in \mathbb{C}^{N_s}$ the RIS response, where $\|\boldsymbol{b}_s\|^2 = N_s$ and B_s is the average element gain. The inspected region $\mathcal{X} \subset \mathbb{R}^2$ is in the radar and RIS far-field; also, radar and RIS are in each other's far-field and

sufficiently spaced to provide independent looks at a prospective target in $\mathcal{X}$ [47].

In the following, $\mathcal{H}$ and $\bar{\mathcal{H}}$ denote the null hypothesis (i.e., no target is present) and its alternative (i.e., one target is present at an unknown location $\boldsymbol{x} \in \mathcal{X}$), respectively. Also, $\boldsymbol{p}_r \in \mathbb{R}^2$ is the position of the radar phase center; $d_r(\boldsymbol{p}) \geq 0$ and $\theta_r(\boldsymbol{p}) \in (-\pi/2, \pi/2)$ are the distance and angle of a point $\boldsymbol{p} \in \mathbb{R}^2$ with respect to the radar phase center, respectively; $\Theta_r \subset (-\pi/2, \pi/2)$ is the angular sector containing the inspected region, as seen from the radar phase center; $\boldsymbol{u}_r(\theta) \in \mathbb{C}^{N_r}$ and $G_r(\theta) \geq 0$ are the array manifold vector and the element gain of the radar towards the angular direction $\theta \in (-\pi/2, \pi/2)$, respectively. For the RIS, $\boldsymbol{p}_s$, $d_s(\boldsymbol{p})$, $\theta_s(\boldsymbol{p})$, Θ_s, $\boldsymbol{u}_s(\theta)$, and $G_s(\theta)$ are similarly defined.

Finally, we have:

- Array gain factor of the radar transmitter:

$$\Gamma_r(\theta) = \left|\boldsymbol{b}_r^{\mathsf{H}} \boldsymbol{u}_r(\theta)\right|^2, \tag{2.1}$$

  which can be controlled via the spatial beamformer $\boldsymbol{b}_r$.

- Array gain factor of the RIS:

$$\Gamma_s(\theta) = \left|\boldsymbol{b}_s^{\mathsf{H}} \mathrm{diag}\left\{\boldsymbol{u}_s\left(\theta_s(\boldsymbol{p}_r)\right)\right\} \boldsymbol{u}_s(\theta)\right|^2, \tag{2.2}$$

  which can be controlled via the RIS response $\boldsymbol{b}_s$.

where, $\theta \in (-\pi/2, \pi/2)$.

We assume that the RIS does not obstruct the radar view, i.e., $\theta_r(\boldsymbol{p}_s) \notin \Theta_r$, and that the RIS is not illuminated by the radar transmitter, i.e., $\Gamma_r\left(\theta_r(\boldsymbol{p}_s)\right) \simeq 0$ (more on this in Sec. 2.3). Under $\bar{\mathcal{H}}$, the target scatters part of the incident signal back towards the radar receiver (direct echo) and part

towards the RIS that in turn amplifies and redirects it towards the radar receiver (indirect echo); accordingly, the received signal is

$$\boldsymbol{y}(t) = \begin{cases} \alpha_1(\boldsymbol{x})\boldsymbol{h}_1(t;\boldsymbol{x}) + \alpha_2(\boldsymbol{x})\boldsymbol{h}_2(t;\boldsymbol{x}) + \boldsymbol{n}(t), & \text{under } \bar{\mathcal{H}}, \\ \boldsymbol{n}(t), & \text{under } \mathcal{H}, \end{cases} \tag{2.3}$$

where $\boldsymbol{h}_1(t;\boldsymbol{x}) \in \mathbb{C}^{N_r}$ and $\boldsymbol{h}_2(t;\boldsymbol{x}) \in \mathbb{C}^{N_r}$ are the space-time signatures of the direct and indirect echoes under $\bar{\mathcal{H}}$, respectively, $\alpha_1(\boldsymbol{x}) \in \mathbb{C}$ and $\alpha_2(\boldsymbol{x}) \in \mathbb{C}$ are the corresponding amplitudes, and $\boldsymbol{n}(t) \in \mathbb{C}^{N_r}$ is the Gaussian noise. Assuming a narrowband signal [56], we have:

$$\boldsymbol{h}_1(t;\boldsymbol{x}) = \boldsymbol{u}_r\big(\theta_r(\boldsymbol{x})\big)\phi_r\big(t - \tau_1(\boldsymbol{x})\big), \tag{2.4a}$$

$$\boldsymbol{h}_2(t;\boldsymbol{x}) = \boldsymbol{u}_r\big(\theta_r(\boldsymbol{p}_s)\big)\phi_r\big(t - \tau_2(\boldsymbol{x})\big). \tag{2.4b}$$

where:

$$\tau_1(\boldsymbol{x}) = 2d_r(\boldsymbol{x})/c,$$
$$\tau_2(\boldsymbol{x}) = \big(d_r(\boldsymbol{x}) + d_s(\boldsymbol{x}) + d_r(\boldsymbol{p}_s)\big)/c,$$

and c is the speed of light. Also, assuming a free-space propagation [57], we have $\alpha_1(\boldsymbol{x}) = \gamma_1(\boldsymbol{x})\tilde{\alpha}_1$, where $\tilde{\alpha}_1 \in \mathbb{C}$ is the unknown (monostatic) target response, while

$$\gamma_1^2(\boldsymbol{x}) = \underbrace{\mathcal{P}_r T_r}_{\substack{\text{radiated} \\ \text{energy}}} \underbrace{\Gamma_r\big(\theta_r(\boldsymbol{x})\big)}_{\substack{\text{transmit} \\ \text{array gain}}} \underbrace{\frac{G_r\big(\theta_r(\boldsymbol{x})\big)}{4\pi d_r^2(\boldsymbol{x})}}_{\substack{\text{link budget in the} \\ \text{radar-target hop}}} \underbrace{\frac{G_r\big(\theta_r(\boldsymbol{x})\big)\lambda^2}{(4\pi)^2 d_r^2(\boldsymbol{x})}}_{\substack{\text{link budget in the} \\ \text{target-radar hop}}}. \tag{2.5}$$

Similarly, $\alpha_2(\boldsymbol{x}) = \gamma_2(\boldsymbol{x})\tilde{\alpha}_2$, where $\tilde{\alpha}_2 \in \mathbb{C}$ is the unknown (bistatic) target response and

$$\gamma_2^2(\boldsymbol{x}) = \underbrace{\mathcal{P}_r T_r}_{\substack{\text{radiated}\\ \text{energy}}} \underbrace{\Gamma_r\big(\theta_r(\boldsymbol{x})\big)}_{\substack{\text{transmit}\\ \text{array gain}}} \underbrace{\frac{G_r\big(\theta_r(\boldsymbol{x})\big)}{4\pi d_r^2(\boldsymbol{x})}}_{\substack{\text{link budget in the}\\ \text{radar-target hop}}} \underbrace{\frac{G_s\big(\theta_s(\boldsymbol{x})\big)\lambda^2}{(4\pi)^2 d_s^2(\boldsymbol{x})}}_{\substack{\text{link budget in the}\\ \text{target-RIS hop}}}$$
$$\times \underbrace{\Gamma_s\big(\theta_s(\boldsymbol{x})\big)}_{\substack{\text{RIS}\\ \text{array gain}}} \underbrace{\frac{B_s G_s\big(\theta_s(\boldsymbol{p}_r)\big) G_r\big(\theta_r(\boldsymbol{p}_s)\big)\lambda^2}{(4\pi)^2 d_r^2(\boldsymbol{p}_s)}}_{\text{link budget in the RIS-radar hop}}. \tag{2.6}$$

Remark 1. The expressions for $\alpha_1(\boldsymbol{x})$ and $\alpha_2(\boldsymbol{x})$ are based on a free-space path loss model and are used solely for signal generation in the numerical evaluations. These models assume line-of-sight propagation and explicitly capture how the waveform power is affected by the geometry, antenna gains, and propagation distances. However, the GLRT itself does not rely on any specific propagation model. It treats the complex amplitudes α_1 and α_2 as unknown deterministic parameters and estimates them directly from the data. This makes the GLRT robust to amplitude model mismatches. In practice, using different propagation environments or more complex channel models would affect the statistics of the received signal and thus the resulting PD and RMSE performance, but not the structure of the detector.

Following [12], [34], [35], [47], the noise is the sum of two independent contributions, namely, $\boldsymbol{n}(t) = \boldsymbol{n}_r(t) + n_s(t)\boldsymbol{u}_r\big(\theta_r(\boldsymbol{p}_s)\big)$. Here, $\boldsymbol{n}_r(t)$ is the noise of the radar receiver, and its entries are modeled as independent white Gaussian processes with Power Spectral Density (PSD) $\sigma_{r,n}^2$. Instead, $n_s(t)$ is the noise coming from the RIS that is amplified together with the signal of interest and redirected towards the radar receiver; in particular, we have

$n_s(t) = g_s \boldsymbol{b}_s^{\mathsf{H}} \mathrm{diag}\{\boldsymbol{u}_s(\theta_s(\boldsymbol{p}_r))\}\tilde{\boldsymbol{n}}_s(t)$, where

$$g_s = \left(\frac{B_s G_s(\theta_s(\boldsymbol{p}_r)) G_r(\theta_r(\boldsymbol{p}_s))\lambda^2}{(4\pi)^2 d_r^2(\boldsymbol{p}_s)}\right)^{1/2}, \tag{2.7}$$

while the n-th entry of $\tilde{\boldsymbol{n}}_s(t) \in \mathbb{C}^{N_s}$ is the dynamic noise of the n-th RIS element, accounting for both the input and the internal noise, assumed independent of the reflected signal. The entries of $\tilde{\boldsymbol{n}}_s(t)$ are modeled as independent white Gaussian processes with PSD $\sigma^2_{s,\tilde{n}}$, so that $n_s(t)$ is itself a white Gaussian process with PSD $\sigma^2_{s,n} = g_s^2 \|\boldsymbol{b}_s\|^2 \sigma^2_{s,\tilde{n}}$. We assume that both $\sigma^2_{r,n}$ and $\sigma^2_{s,n}$ are known; for example, they can be estimated by resorting to secondary data.

Finally, the power consumed by the radar transmitter can be modeled as $\mathcal{P}_r^{\mathrm{tot}} = \rho_r + \eta_{r,\mathrm{all}}^{-1}\mathcal{P}_r$, where ρ_r is the static power [58] and $\eta_{r,\mathrm{all}}$ is the overall efficiency of the RF amplifier [59, Eq. (10)]. Instead, the power consumed by the active RIS can be modeled as $\mathcal{P}_s^{\mathrm{tot}} = \big(\rho_s + \eta_{s,\mathrm{PAE}}^{-1}\mathcal{P}_{s,in}(B_s - 1)\big)N_s$, where $\rho_s = \rho_{s,c} + \rho_{s,dc}$ is the static power per each element [34], [50], with $\rho_{s,c}$ being the switch and control circuit power and $\rho_{s,dc}$ the DC biasing power, $\eta_{s,\mathrm{PAE}}$ is the Power-Added Efficiency (PAE) of the amplifier [59, Eq. (12)],

$$\mathcal{P}_{s,in} = \sigma^2_{s,\tilde{n}} W_r + \mathcal{P}_r \Gamma_r\big(\theta_r(\boldsymbol{x})\big) \frac{G_r\big(\theta_r(\boldsymbol{x})\big)}{4\pi d_r^2(\boldsymbol{x})} \frac{G_s\big(\theta_s(\boldsymbol{x})\big)\lambda^2}{(4\pi)^2 d_s^2(\boldsymbol{x})} |\tilde{\alpha}_2|^2 \tag{2.8}$$

is the input power (i.e., the sum of the dynamic noise power and incident power), and $\mathcal{P}_{s,in}(B_s - 1)$ is the difference between the output and input power; the term $\eta_{s,\mathrm{PAE}}^{-1}\mathcal{P}_{s,in}(B_s - 1)$ is often much smaller than $\rho_{s,dc}$. This claim is supported by practical power modeling analysis presented in [60], which shows that the dominant power consumption in active RIS elements arises from DC biasing and control circuitry, while the RF power-added contribution is typically in the sub-milliwatt range due to low power-added efficiency and weak input signals. As a result, the term $\eta_{s,\mathrm{PAE}}^{-1}\mathcal{P}_{s,\mathrm{in}}(B_s - 1)$

remains significantly smaller than $\rho_{s,\mathrm{dc}}$, as assumed in our system model. Notice that $\mathcal{P}_s^{\mathrm{tot}} = N_s \rho_{s,c}$ for a passive RIS and $\mathcal{P}_s^{\mathrm{tot}} = 0$ if no RIS is present. Hence, for the same power budget[1] $\mathcal{P}^{\mathrm{tot}} = \mathcal{P}_r^{\mathrm{tot}} + \mathcal{P}_s^{\mathrm{tot}}$, the radar radiates more power when a passive RIS or no RIS is employed.

2.3 System design

In this section, we first illustrate the design of the radar transmitter and RIS; then, we consider the radar receiver.

Given the prior uncertainty on the target location, we propose to choose $\boldsymbol{b}_r$ and $\boldsymbol{b}_s$ so that $\Gamma_r(\theta)$ and $\Gamma_s(\theta)$ approximate an ideal rectangular function that is non-zero only if $\theta \in \Theta_r$ and $\theta \in \Theta_s$, respectively, so as to ensure a uniform converge of the inspected region. Many matching criteria are available in the literature: see [56] and references therein. For example, in Sec. 2.4 we resort to a least-square solution with a Taylor tapering to reduce the level of the sidelobes.

The received signal $\boldsymbol{y}(t)$ is sent to a low-pass filter with impulse response $\psi_r(t) = \sqrt{\Psi_r}\,\mathrm{Rect}(t/\Psi_r)$, where $\mathrm{Rect}(t)$ is a unit-amplitude rectangular pulse with support $[0,1]$ and $1/\Psi_r \geq W_r$; the filter output is then sampled at rate $1/\Psi_r$ in the time interval $[\tau_{\min}, \tau_{\max} + \Phi_r + \Psi_r]$, where $\tau_{\min} = \min_{i\in\{1,2\},\,\boldsymbol{x}\in\mathcal{X}} \tau_i(\boldsymbol{x})$ and $\tau_{\max} = \max_{i\in\{1,2\},\,\boldsymbol{x}\in\mathcal{X}} \tau_i(\boldsymbol{x})$. The samples taken at the time epochs $\{\tau_{\min} + \ell\Psi_r\}_{\ell=0}^{F_r-1}$ are organized into a vector $\boldsymbol{y} \in \mathbb{C}^{M_r}$, where $F_r = \lfloor(\tau_{\max} - \tau_{\min} + \Phi_r + \Psi_r)/\Psi_r\rfloor + 1$ and $M_r = N_r F_r$.

[1] We omit in this power budget the consumption of the radar receiver, which can be assumed to be the same whether or not a help RIS is considered.

Let $\boldsymbol{\phi}_{r,i}(\boldsymbol{x}) \in \mathbb{C}^{F_r}$ be the vector containing the samples of the filtered waveform $\phi_r\big(t - \tau_i(\boldsymbol{x})\big) * \psi_r(t)$, for $i = 1, 2$; then, we have

$$\boldsymbol{y} = \begin{cases} \boldsymbol{H}(\boldsymbol{x})\boldsymbol{\alpha}(\boldsymbol{x}) + \boldsymbol{n}, & \text{under } \bar{\mathcal{H}}, \\ \boldsymbol{n}, & \text{under } \mathcal{H}, \end{cases} \tag{2.9}$$

where

$$\boldsymbol{\alpha}(\boldsymbol{x}) = [\alpha_1(\boldsymbol{x})\ \alpha_2(\boldsymbol{x})]^{\mathsf{T}}, \tag{2.10a}$$

$$\boldsymbol{H}(\boldsymbol{x}) = [\boldsymbol{h}_1(\boldsymbol{x})\ \boldsymbol{h}_2(\boldsymbol{x})], \tag{2.10b}$$

$$\boldsymbol{h}_1(\boldsymbol{x}) = \boldsymbol{u}_r\big(\theta_r(\boldsymbol{x})\big) \otimes \boldsymbol{\phi}_{r,1}(\boldsymbol{x}), \tag{2.10c}$$

$$\boldsymbol{h}_2(\boldsymbol{x}) = \boldsymbol{u}_r\big(\theta_r(\boldsymbol{p}_s)\big) \otimes \boldsymbol{\phi}_{r,2}(\boldsymbol{x}), \tag{2.10d}$$

while $\boldsymbol{n}$ contains the samples of the filtered noise. Under the considered assumptions, $\boldsymbol{H}(\boldsymbol{x})$ is full column-rank for any $\boldsymbol{x} \in \mathcal{X}$, and $\boldsymbol{n}$ is a circularly-symmetric complex Gaussian vector with covariance matrix $\boldsymbol{C} = \Big(\sigma_{r,n}^2 \boldsymbol{I}_{N_r} + \sigma_{s,n}^2 \boldsymbol{u}_r\big(\theta_r(\boldsymbol{p}_s)\big)\boldsymbol{u}_r^{\mathsf{H}}\big(\theta_r(\boldsymbol{p}_s)\big)\Big) \otimes \boldsymbol{I}_{F_r}$.

We solve the binary test in (2.9) by resorting to a GLRT, wherein we treat the target location $\boldsymbol{x}$ and the corresponding signal amplitudes $\alpha_1(\boldsymbol{x})$ and $\alpha_2(\boldsymbol{x})$ under $\bar{\mathcal{H}}$ as unknown deterministic parameters [61]. Given $\boldsymbol{x}$ and $\boldsymbol{\alpha}(\boldsymbol{x})$, the log-likelihood ratio between $\bar{\mathcal{H}}$ and $\mathcal{H}$ is

$$\Lambda\big(\boldsymbol{x}, \boldsymbol{\alpha}(\boldsymbol{x})\big) = 2\Re\Big\{\boldsymbol{\alpha}^{\mathsf{H}}(\boldsymbol{x})\boldsymbol{H}^{\mathsf{H}}(\boldsymbol{x})\boldsymbol{C}^{-1}\boldsymbol{y}\Big\} - \boldsymbol{\alpha}^{\mathsf{H}}(\boldsymbol{x})\boldsymbol{H}^{\mathsf{H}}(\boldsymbol{x})\boldsymbol{C}^{-1}\boldsymbol{H}(\boldsymbol{x})\boldsymbol{\alpha}(\boldsymbol{x}), \tag{2.11}$$

which is maximized when $\boldsymbol{\alpha}(\boldsymbol{x})$ is chosen as

$$\Big(\boldsymbol{H}^{\mathsf{H}}(\boldsymbol{x})\boldsymbol{C}^{-1}\boldsymbol{H}(\boldsymbol{x})\Big)^{-1}\boldsymbol{H}^{\mathsf{H}}(\boldsymbol{x})\boldsymbol{C}^{-1}\boldsymbol{y}. \tag{2.12}$$

Accordingly, the GLRT becomes

$$\max_{\boldsymbol{x}\in\mathcal{X}} \left\|\boldsymbol{\Pi}^{\mathsf{H}}(\boldsymbol{x})\boldsymbol{y}\right\|^2 \underset{H_0}{\overset{H_1}{\gtrless}} \eta, \tag{2.13}$$

where

$$\boldsymbol{\Pi}(\boldsymbol{x}) = \boldsymbol{C}^{-1}\boldsymbol{H}(\boldsymbol{x})(\boldsymbol{H}^{\mathsf{H}}(\boldsymbol{x})\boldsymbol{C}^{-1}\boldsymbol{H}(\boldsymbol{x}))^{-1/2} \tag{2.14}$$

and η is a threshold set to have a specified Probability of False Alarm (PFA). Notice that $\left\|\boldsymbol{\Pi}^{\mathsf{H}}(\boldsymbol{x})\boldsymbol{y}\right\|^2$ is the energy of the whitened observation $\boldsymbol{C}^{-1/2}\boldsymbol{y}$ falling in the two-dimensional column space of $\boldsymbol{C}^{-1/2}\boldsymbol{H}(\boldsymbol{x})$. As customary, the maximization over $\mathcal{X}$ is undertaken by a grid search. If $\bar{\mathcal{H}}$ is declared, the argument of the maximum provides an estimate of the target location.

Remark 2. The GLRT in Equation (2.13) is derived under the assumption that the complex amplitudes $\alpha_1(\boldsymbol{x})$ and $\alpha_2(\boldsymbol{x})$ are unknown and estimated without any constraints. This approach is suitable when no prior information is available, but in some specific settings, there may exist useful relationships between the two paths. For instance, if the radar system has knowledge of the relative power levels, phase shifts, or statistical dependence between the direct and RIS-assisted echoes, such information could be used to constrain the amplitude model. Incorporating these constraints into the detector design might help improving sensing performance.

Another assumption in the current formulation is that the target is equally likely to be located anywhere within the region of interest $\mathcal{X}$. While this simplifies the design, it may not reflect actual operational conditions, where prior knowledge about the spatial distribution of targets is often available. This could come from previous sensor measurements, contextual maps, or mission-related information. Integrating such a-priori knowledge

into the detection process, for example by weighting the likelihood function with a non-uniform spatial distribution, can improve detection and localization performance. It may also inform the design of the radar and RIS beam patterns by focusing energy on areas with higher probability. Exploring both of these directions could lead to more informed and adaptive sensing strategies in future systems.

To better understand the decision statistic, note that the radar receiver employs a digital array architecture wherein the signal from each antenna element is independently sampled and processed to form the observation vector $\boldsymbol{y}$. Under hypothesis $\bar{\mathcal{H}}$, the received signal lies in the two-dimensional subspace spanned by $\boldsymbol{C}^{-1}\boldsymbol{H}(\boldsymbol{x})$. As such, the GLRT in (2.13) tests whether the received vector $\boldsymbol{y}$ resides significantly in such a subspace, with each candidate point $\boldsymbol{x}$ producing a different projection. In this framework, traditional concepts such as beampatterns depending only on angles do not apply directly, since the statistic also depends on delay and bistatic geometry.

To illustrate these properties, Fig. 2.3 shows the heat map of the test statistic $\left\|\boldsymbol{\Pi}^{\mathsf{H}}(\boldsymbol{x})\,\boldsymbol{C}^{-1/2}\boldsymbol{y}\right\|^2$ over the inspected region for two independent snapshots (using the simulation setup described later in Sec. 2.4). The plots are in decibel scale, and the red star marks the true target position. The test statistic peaks near the target, and its structure reflects the intersection of regions with constant monostatic and bistatic ranges, forming curved patterns that highlight how both paths contribute to the localization performance.

The following remarks are now in order.

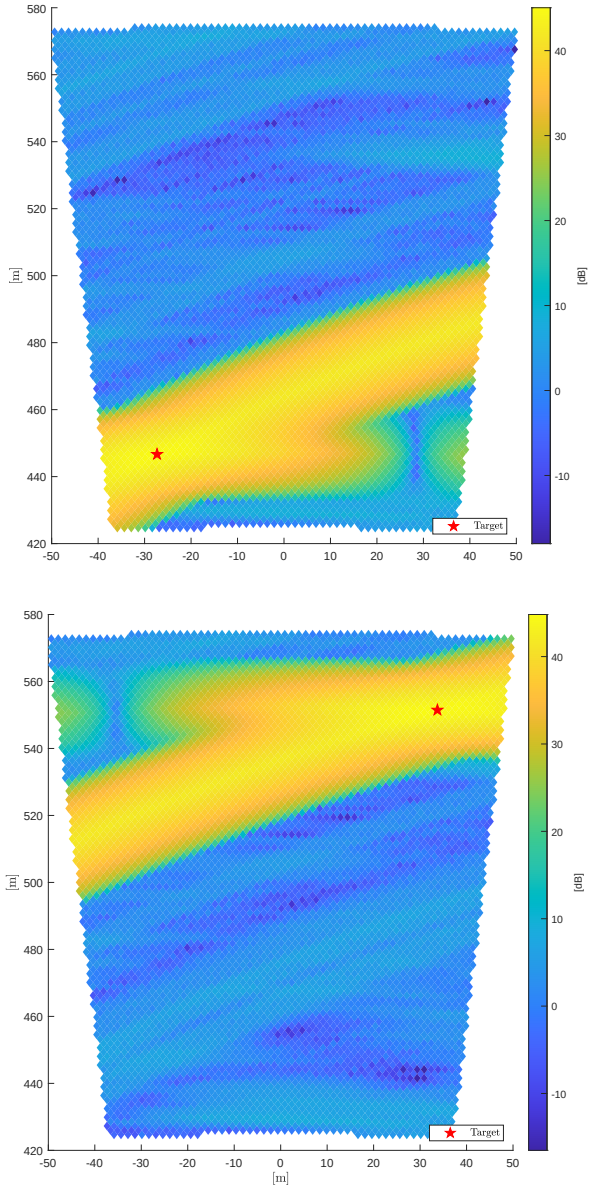

FIGURE 2.3: Test statistic $\left\|\boldsymbol{\Pi}^{\mathsf{H}}(\boldsymbol{x})\boldsymbol{C}^{-1/2}\boldsymbol{y}\right\|^2$ over the inspected region in two different snapshots. The reported values are in decibel. The true target location is marked with a red star-marker and $\mathrm{SNR}_1 = 30\,\mathrm{dB}$

Remark 3. If $\boldsymbol{h}_1^{\mathsf{H}}(\boldsymbol{x})\boldsymbol{C}^{-1}\boldsymbol{h}_2(\boldsymbol{x}) = 0$, then the k-th column of $\boldsymbol{\Pi}(\boldsymbol{x})$ is simply

$$\boldsymbol{C}^{-1}\boldsymbol{h}_k(\boldsymbol{x})/(\boldsymbol{h}_k^{\mathsf{H}}(\boldsymbol{x})\boldsymbol{C}^{-1}\boldsymbol{h}_k(\boldsymbol{x}))^{1/2}. \tag{2.15}$$

Since

$$\boldsymbol{h}_1^{\mathsf{H}}(\boldsymbol{x})\boldsymbol{C}^{-1}\boldsymbol{h}_2(\boldsymbol{x}) = \frac{\boldsymbol{u}_r^{\mathsf{H}}\big(\theta_r(\boldsymbol{x})\big)\boldsymbol{u}_r\big(\theta_r(\boldsymbol{p}_s)\big)\boldsymbol{\phi}_{r,1}^{\mathsf{H}}(\boldsymbol{x})\boldsymbol{\phi}_{r,2}(\boldsymbol{x})}{\sigma_{r,n}^2 + N_r\sigma_{s,n}^2}, \tag{2.16}$$

this occurs when the steering vectors towards the prospective target and the RIS are orthogonal or if the delay offset between the direct and indirect echoes exceeds the duration of $\phi_r(t) * \psi_r(t)$, i.e., $|d_s(\boldsymbol{x}) + d_r(\boldsymbol{p}_s) - d_r(\boldsymbol{x})| > c(\Phi_r + \Psi_r)$.

Remark 4. When no RIS is employed, the GLRT has still the form in (2.13), but with

$$\boldsymbol{\Pi}(\boldsymbol{x}) = \boldsymbol{C}^{-1}\boldsymbol{h}_1(\boldsymbol{x})/(\boldsymbol{h}_1^{\mathsf{H}}(\boldsymbol{x})\boldsymbol{C}^{-1}\boldsymbol{h}_1(\boldsymbol{x}))^{1/2} \tag{2.17}$$

Since $\|\boldsymbol{\Pi}^{\mathsf{H}}(\boldsymbol{x})\boldsymbol{y}\|^2$ is now the energy of the whitened observation $\boldsymbol{C}^{-1/2}\boldsymbol{y}$ falling in the one-dimensional subspace spanned by $\boldsymbol{C}^{-1/2}\boldsymbol{h}_1(\boldsymbol{x})$, for a fixed PFA, the GLRT needs here a lower threshold as compared to the proposed case.

Remark 5. The matrices $\{\boldsymbol{\Pi}(\boldsymbol{x})\}_{\boldsymbol{x}\in\mathcal{X}}$ can be computed off-line which a computational complexity that scales quadratically with the length M_r of the observation vector and linearly with the number $|\mathcal{X}|$ of grid points. Instead, given the current measurement $\boldsymbol{y}$, the in-line implementation of the GLRT in (2.13) is dominated by the multiplication of $\boldsymbol{\Pi}^{\mathsf{H}}(\boldsymbol{x})$ by $\boldsymbol{y}$ for each grid point, so that the computational complexity scales linearly with both M_r and $|\mathcal{X}|$. Interestingly, when no help RIS is present, the above asymptotic costs remain the same. In other words the implementation of the GLRT in 2.16 requires computing $\|\boldsymbol{\Pi}^{\mathsf{H}}(\boldsymbol{x})\boldsymbol{C}_n^{-1/2}\boldsymbol{y}\|^2$ for each grid point in $\mathcal{X}$. Assume that the $M_r \times 2$ matrix $\boldsymbol{\Pi}(\boldsymbol{x}) = \boldsymbol{C}^{-1/2}\boldsymbol{H}(\boldsymbol{x})(\boldsymbol{H}^{\mathsf{H}}(\boldsymbol{x})\boldsymbol{C}^{-1}\boldsymbol{H}(\boldsymbol{x}))^{-1/2}$ is computed off-line for each grid point; then, given the whitened measurement $\boldsymbol{C}^{-1/2}\boldsymbol{y} \in \mathbb{C}^{M_r}$, the GLRT implementation entails a complexity that

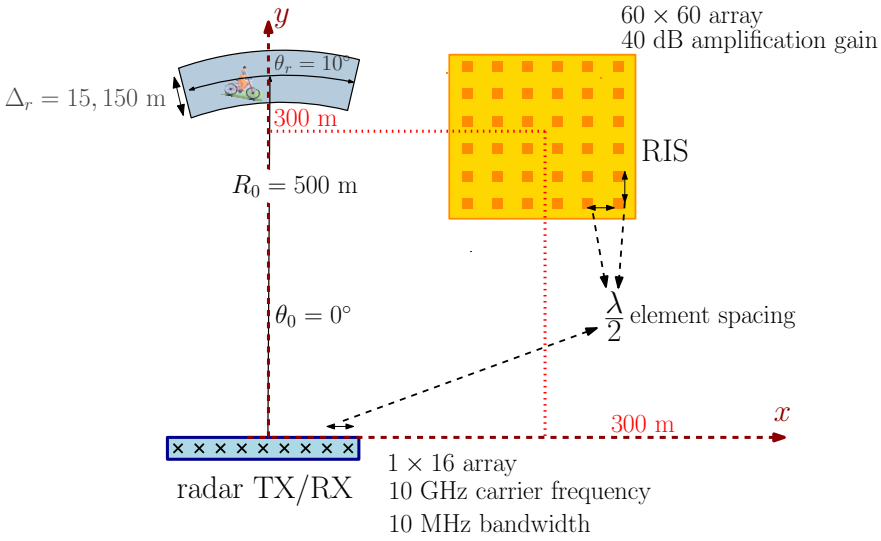

FIGURE 2.4: Schematic diagram of the simulated system.

scales linearly with the number of grid points and the length of the observation vector. Interestingly, the GLRT presents a similar computational complexity also when no RIS is present.

Remark 6. When multiple targets are present in $\mathcal{X}$, we may resort to standard approaches, such as for example subspace-based iterative procedures that extract one target at a time after eliminating the previously-detected signal components [62].

2.4 Performance analysis

We consider an X-band system with $\lambda = 3\,\text{cm}$, $G_r(\theta) = G_s(\theta) = 2\cos(\theta)\text{Rect}(\theta/\pi + 1/2)$, $T_r = 10$ µs, $\phi_r(t) = \sqrt{\Phi_r}\,\text{Rect}(t/\Phi_r)$, $\Phi_r = \Psi_r = 0.1$ µs, $W_r = 10\,\text{MHz}$, $N_r = 16$, $N_s = 3600$, $\delta_r = \delta_s = \lambda/2$, and $\sigma^2_{r,n} = \sigma^2_{s,\tilde{n}} = 1.6 \cdot 10^{-20}\,\text{W/Hz}$. As to the power consumption, we assume $\rho_r = 30\,\text{W}$, $\eta_{r,\text{all}} = 0.9$, and $\mathcal{P}_r = 8\,\text{W}$ for the radar transmitter, which gives a system efficiency $\mathcal{P}_r/\mathcal{P}_r^{\text{tot}}$ of about 20%, and $\rho_{s,c} = 0.1\,\text{mW}$,

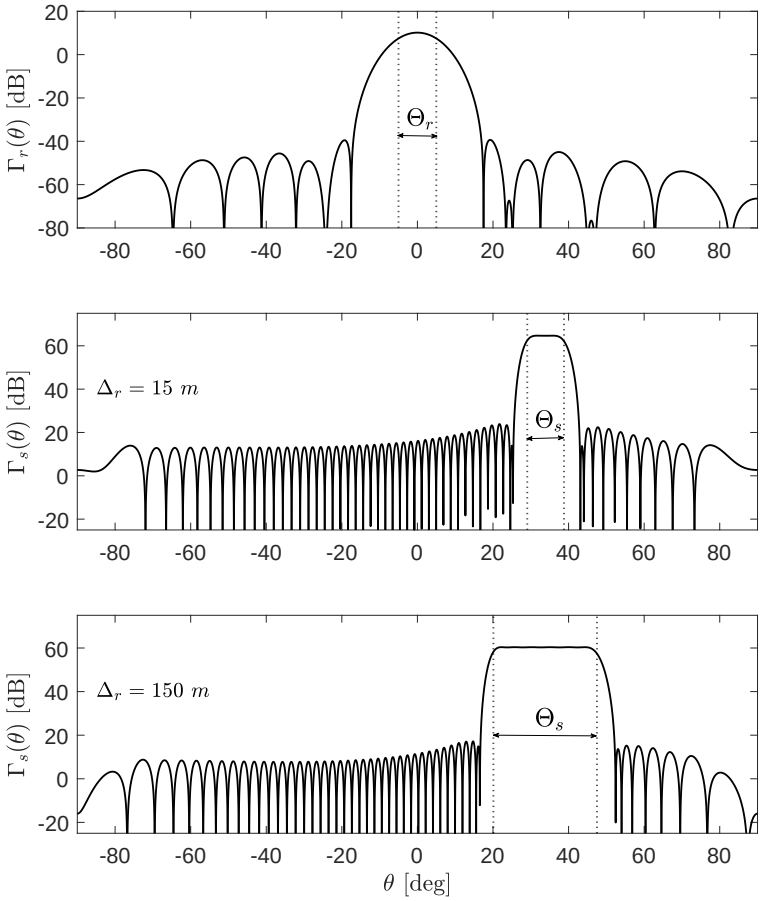

FIGURE 2.5: Top plot: array gain factor of the radar transmitter. Middle and bottom plots: array gain factor of the RIS for $\Delta_r = 15, 150$ m, respectively.

$\rho_{s,dc} = 0.32$ mW, and $\eta_{s,\text{PAE}} = 0.8$ for the active RIS. As to the target, $\tilde{\alpha}_1$ and $\tilde{\alpha}_2$ are generated as independent realizations of a circularly-symmetric Gaussian random variable with variance σ_t^2. With reference to Fig. 2.4, the radar is at the origin of the coordinate system and inspects the range interval $[500 - \Delta_r/2, 500 + \Delta_r/2]$ m in the angular sector $\Theta_r = [-5°, 5°]$, while the RIS is at $(300, 300)$ m. Two values of Δ_r are considered, namely, 15 and 150 m, with the former corresponding to the range resolution $c/(2W_r)$. The

TABLE 2.1: PD, RMSE, and SNR_2 when $\mathrm{SNR}_1 = 15\,\mathrm{dB}$

Δ_r [m]		No RIS	Passive RIS	Active RIS: B_s [dB]			
				25	30	35	40
15	PD	0.56	0.51	0.52	0.63	0.80	0.92
	RMSE [m]	14.3	14.9	12.6	10.1	7.9	7.0
	SNR_2[dB]	—	-19.8	4.7	9.7	17.7	19.7
150	PD	0.53	0.48	0.45	0.49	0.61	0.79
	RMSE [m]	29.8	31.4	31.1	28.1	23.3	19.9
	SNR_2[dB]	—	-24.1	0.4	5.4	10.4	15.4

top plot in Fig. 2.5 shows the array gain factor $\Gamma_r(\theta)$ of the radar transmitter; here, the mainbeam covers the angular sector Θ_r, and a null is placed at $\theta = \theta_r(\boldsymbol{p}_s) = \pi/4$. The middle and bottom plots in Fig. 2.5 show the array gain factor $\Gamma_s(\theta)$ of the RIS for $\Delta_r = 15, 150\,\mathrm{m}$, respectively; notice here that a wider mainbeam is required to cover the region of interest when Δ_r increases, at the price of a lower array gain.

We define the SNR of the direct echo as

$$\mathrm{SNR}_1 = \frac{N_r \gamma_1^2(\bar{\boldsymbol{x}})\sigma_t^2}{\sigma_{r,n}^2}, \tag{2.18}$$

where $\bar{\boldsymbol{x}}$ is a reference point with range $R_0 = 500\,\mathrm{m}$ and azimuth $\theta_0 = 0^\circ$. Fig. 2.6 shows the PD and the RMSE in the target localization of the proposed architecture versus SNR_1 when $B_s = 40\,\mathrm{dB}$. The reported values are computed over 10^5 independent snapshots, while SNR_1 is varied by increasing the radar target cross-section σ_t^2. In each snapshot, the target is randomly dropped in $\mathcal{X}$ under $\bar{\mathcal{H}}$. The performance of the proposed architecture is contrasted with that of a radar helped by a passive RIS or operating alone, when keeping the same consumed power $\mathcal{P}^{\mathrm{tot}}$; in all cases, the detection threshold is chosen to have $\mathrm{PFA} = 10^{-5}$.

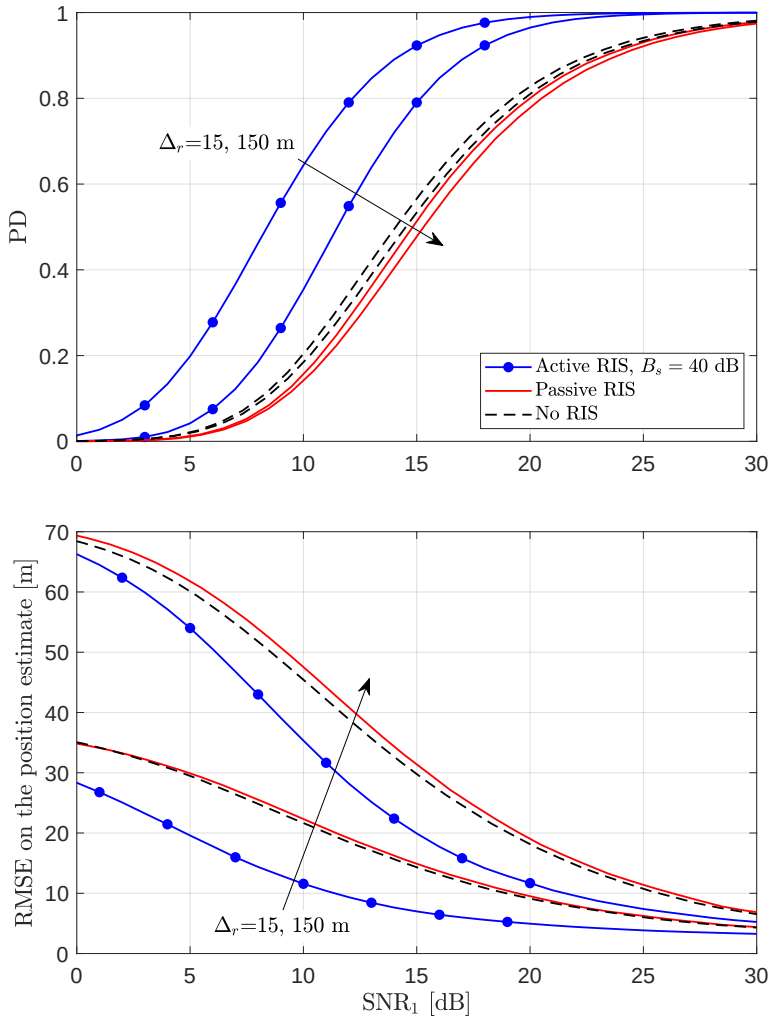

FIGURE 2.6: PD (top plot) and RMSE on the position estimate (bottom plot) versus SNR_1 when $\Delta_r = 15, 150$ m and no RIS, a passive RIS, and an active RIS with $B_s = 40$ dB are employed.

To comprehensively explore the capabilities of the proposed active RIS-assisted radar system, further simulations have been performed by varying several key system parameters. Specifically, the system performance, quantified in terms of PD and localization accuracy measured by RMSE,

is evaluated as a function of the SNR under different conditions of , range interval, RIS amplification gain, RIS positioning, and angular sector width. These additional results provide an in-depth understanding of how the system behaves under diverse spatial and operational settings. The following analysis illustrates the impact of each parameter, supported by corresponding simulation figures.

Effect of range interval on detection and localization performance:

Fig. 2.7 presents the variation of PD and localization accuracy (RMSE) with respect to SNR_1 for different range intervals of 15 m, 90 m, and 165 m. As expected, a larger range interval degrades both detection and localization performance. Specifically, PD decreases and RMSE increases with the widening of the range interval, since coarser spatial discretization reduces the radar's ability to resolve and accurately localize targets in adjacent range bins. Moreover, for larger intervals, the PD curve rises more slowly with SNR_1, indicating that higher SNR levels are required to achieve reliable detection.

The performance enhancement introduced by the active RIS is evident across all cases. Compared to the radar-only configuration, the active RIS consistently achieves higher PD and lower RMSE. Notably, this improvement becomes more pronounced as the range interval increases, demonstrating that the RIS helps to overcome the limitations in range resolution introduced by a wider search interval. This is primarily due to the amplification and controlled phase adjustment provided by the active RIS, which enhance the backscattered signal and improve overall target detectability and localization accuracy.

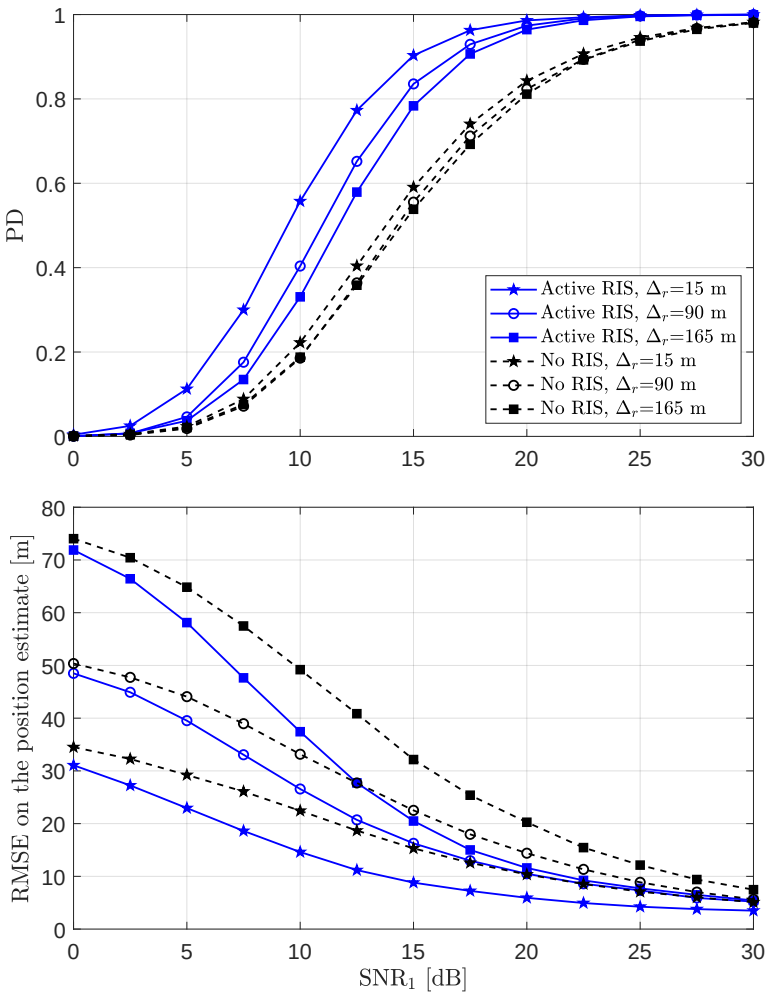

FIGURE 2.7: PD (top plot) and RMSE on the position estimate (bottom plot) versus SNR_1 when $\theta_0 = -45^\circ$ and no RIS, and an active RIS with $B_s = 40$ dB are employed.

Effect of amplification gain of active RIS on detection and localization performance:

Figure 2.8 shows how the PD and localization error (RMSE) vary with SNR_1 for different RIS amplification gains, including $B_s = 35$, 40, and 45 dB. The results also include comparisons with a passive RIS and a conventional

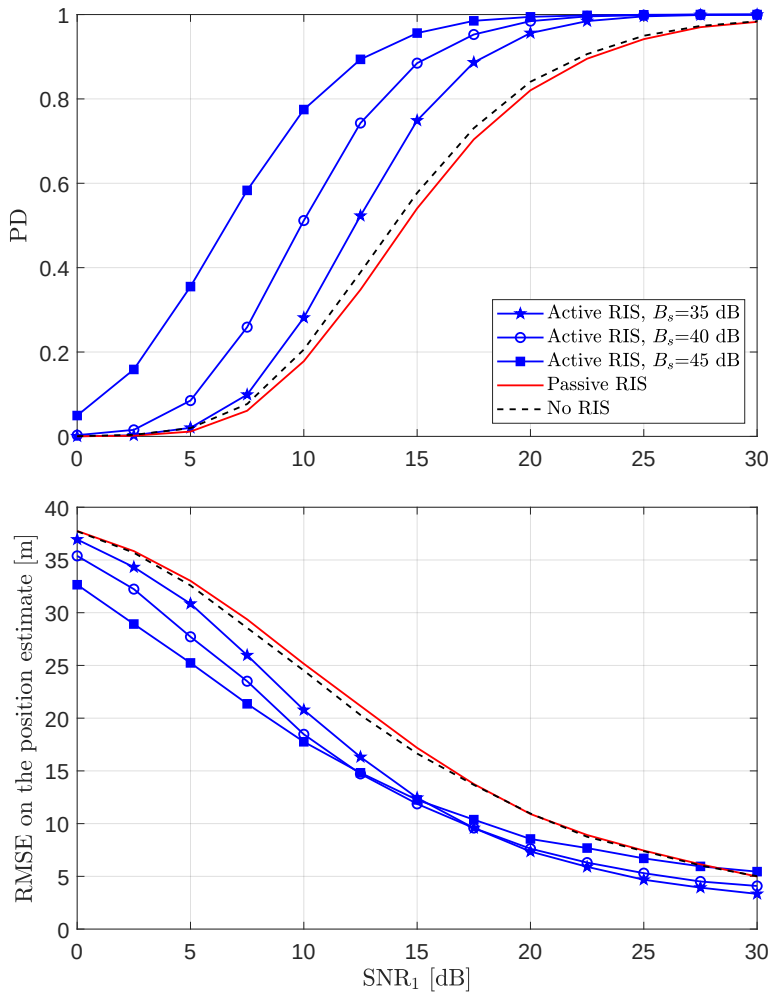

FIGURE 2.8: PD (top plot) and RMSE on the position estimate (bottom plot) versus SNR_1 when $\Delta_r = 30\,\text{m}$, $\theta_0 = -45^\circ$ and no RIS, a passive RIS, and an active RIS with $B_s = 40\,\text{dB}$ are employed.

radar system without any RIS. As expected, using an active RIS significantly improves the ability to detect a target. Higher amplification makes the reflected signal stronger, which increases PD across all SNR levels. In

contrast, the passive RIS performs worse than the system without RIS, because the indirect link suffers from path loss. Without amplifying the reflected signal, the echo that arrives at the receiver is very weak. As a result, the PD decreases, and the presence of a passive RIS can even be detrimental when compared to a system with no RIS at all.

However, localization accuracy behaves differently compared to detection performance. At moderate SNR levels, active RIS helps reduce RMSE due to the additional observation path it provides. But as both SNR and RIS gain become high, a noticeable increase in localization error is observed. The reason is that the indirect path becomes stronger than the direct one. While radar can estimate both the range and direction (azimuth) of the target, the RIS reflection mainly provides range information, without azimuth resolution. When the system relies more on the RIS path, it loses the directional accuracy that comes from the direct link, which results in worse position estimates, even though detection remains strong.

These results highlight a key trade-off in RIS-aided radar systems: stronger amplification improves detection but can come at the cost of localization precision. For best overall performance, especially in scenarios where accuracy is critical, the RIS gain must be carefully tuned to avoid overpowering the direct path with a less informative but stronger reflected signal.

It is also worth noting that the degraded performance of the passive RIS in the current setup is primarily due to the weak strength of the indirect echo, which undergoes significant two-hop path loss. This limitation becomes more pronounced when the RIS contains a moderate number of elements and is located far from both the radar and the target. However, if the size of the passive RIS were significantly increased, the resulting

aperture gain could enhance the strength of the reflected signal, potentially reversing the observed performance trend. In such cases, and under favorable geometries, a sufficiently large passive RIS might outperform the no-RIS scenario. It should be emphasized, however, that such configurations may enter the near-field propagation regime, where the usual far-field assumptions no longer hold. Moreover, as the RIS aperture grows, the narrowband array assumption underlying our signal model may no longer be valid, especially if the bandwidth is not small relative to the inverse of the array's spatial extension. Violating this assumption implies that frequency-dependent phase shifts and delay spreads across the surface must be taken into account. Accurately modeling these wideband and near-field effects would require a more advanced analytical framework that accounts for spherical wavefronts, spatial non-stationarity, and variation of the signal across elements. Exploring these aspects represents an important direction for future work in extending the applicability of passive RIS-aided radar systems.

The degradation in localization accuracy at high SNR and large RIS gain is due to the indirect path dominating the measurement, despite offering limited azimuth information. This issue could be addressed by modifying the decision statistic to reduce over-reliance on the indirect echo, or by optimizing the RIS gain to balance detection performance and localization precision. Such adaptations may improve robustness in high-gain scenarios and represent a promising extension of the current framework.

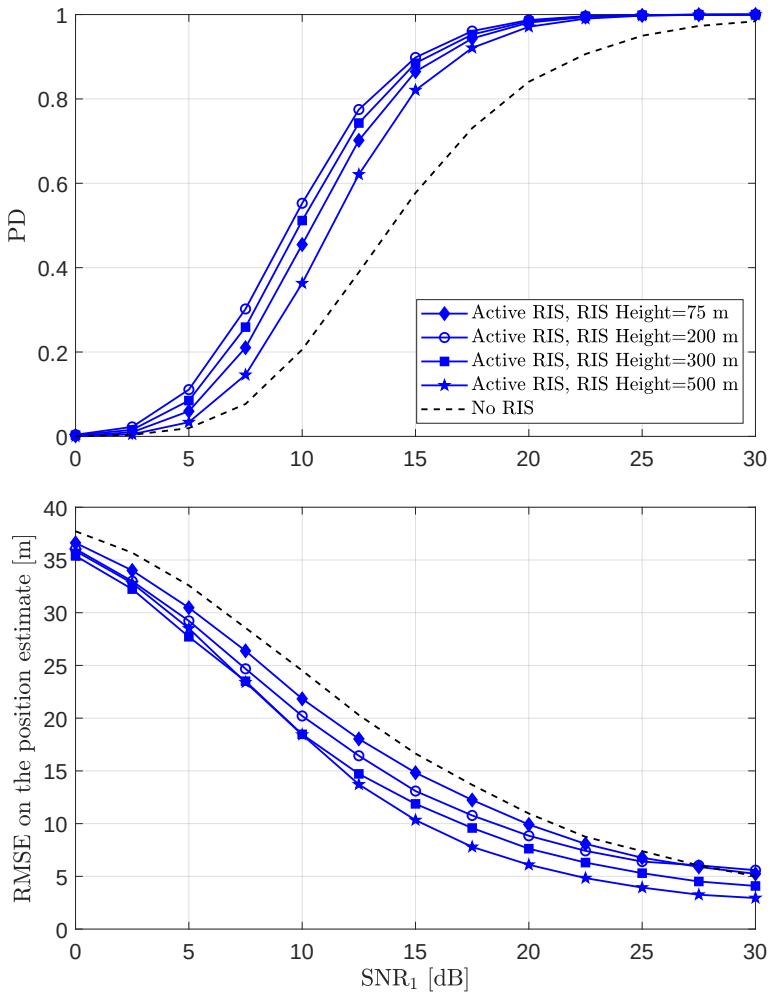

FIGURE 2.9: PD (top plot) and RMSE on the position estimate (bottom plot) versus SNR_1 when $\Delta_r = 30\,\text{m}$, $\theta_0 = -45^\circ$ and no RIS, a passive RIS, and an active RIS with $B_s = 40\,\text{dB}$ are employed.

Effect of RIS positioning on detection and localization performance:

In this part of the study, we examine how the vertical placement of the RIS affects the radar system's detection and localization performance. Specifically, the height of the RIS (y_s) is varied across four values: y_s=75 m, 200 m,

300 m, and 500 m and the results are compared to the reference case without any RIS.

As shown in Fig.2.9, the detection performance (PD) is highest when the RIS is placed at 200m. Lower placements, like 75m, provide limited improvement, while higher positions such as 300m and 500 m slightly reduce PD, but still outperform the case with no RIS. For localization accuracy, the results show a different trend. The RMSE consistently decreases as the RIS height increases, with the best accuracy achieved at 500 m. These results highlight that the RIS position has a significant impact on both detection and localization. Therefore, careful placement of the RIS is essential to achieve the best system performance.

Effect of angular sector width on detection and localization performance:

This part of the analysis explores how the angular sector width, denoted by Θ_r, impacts the target detection and localization performance of the radar system. Specifically, we consider three sector widths, $\Theta_r = 5^\circ$, 15°, and 30° and compare the results for systems with and without an active RIS.

As shown in Fig. 2.10, a wider angular sector generally leads to a lower PD, which is expected since the radar has to search over a larger area. This reduces its ability to focus energy in the target direction, making detection more challenging. The performance drop is most noticeable in the system without RIS, where increasing Θ_r causes a significant decline in PD. In contrast, when an active RIS is used, the system maintains a higher detection probability across all sector settings. Even at $\Theta_r = 30^\circ$, the PD with the RIS is still better than the radar-only system operating at a much narrower angle of $\Theta_r = 5^\circ$. This clearly shows how the RIS helps reinforce detection, especially when the coverage area becomes wider.

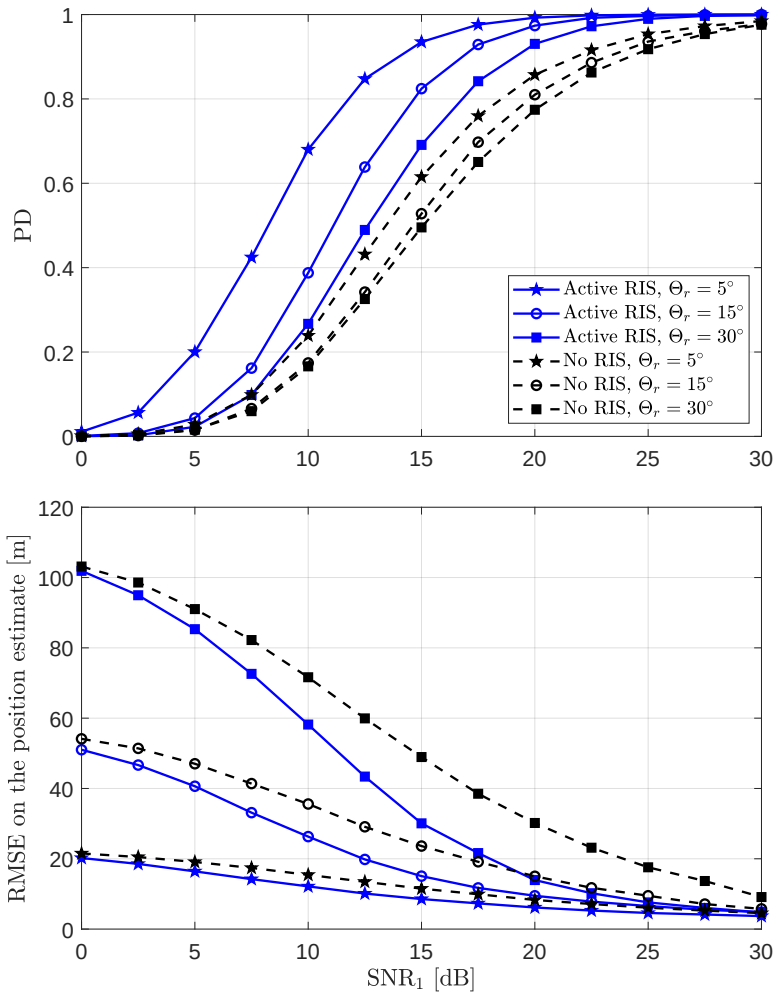

FIGURE 2.10: PD (top plot) and RMSE on the position estimate (bottom plot) versus SNR_1 when $\Delta_r = 30\,\text{m}$, $\theta_0 = -45°$ and no RIS, a passive RIS, and an active RIS with $B_s = 40\,\text{dB}$ are employed.

When it comes to localization accuracy, a similar trend appears. As the angular sector increases, the RMSE also increases because the system becomes less precise in estimating the target's direction. However, the presence of the active RIS consistently improves localization performance. Across all sector widths, the RMSE is lower with the RIS compared to the

radar without it. The improvement is especially noticeable at larger sectors, where conventional systems tend to struggle the most. Here, the additional reflected signal from the RIS provides spatial diversity that helps reduce uncertainty in the target's position.

Overall, these results demonstrate that while a wider angular sector typically makes detection and localization more difficult, an active RIS can significantly reduce those negative effects. Its ability to enhance both signal strength and spatial resolution makes it particularly valuable for applications that require broad coverage.

2.5 Conclusions

In this chapter, we have used an active RIS to get a second observation of the region inspected by a monostatic radar equipped with a digital array. We have designed the array gain factor of the radar transmitter and the RIS to uniformly cover the inspected region and solved the target detection and localization problem via a GLRT. The numerical analysis shows that, for the same power budget, the active RIS improves the radar performance if a sufficiently large amplification gain can be guaranteed. Future studies should account for the clutter presence and should investigate the radar and RIS scanning policy when multiple regions need to be inspected, each one possibly containing multiple targets.

Chapter 3

STAR-RIS-based Pulse-Doppler Radars

This chapter is based on article published in the Proceedings of the *2024 32nd European Signal Processing Conference (EUSIPCO)* [63].

3.1 Introduction

RISs are receiving increasing attention in both wireless communication and sensing applications. An RIS is a planar structure consisting of a large number of sub-wavelength size elements (atoms) that are low-cost and reconfigurable in terms of their electromagnetic responses. RISs can improve the spectral efficiency, energy efficiency, security, and reliability of wireless communication networks to some extend the radio propagation environment [37], [64], [65]; they have also been considered in radio localization and mapping [23], path planning [66], and radar target detection [28], [45], [67]. While transmitting-only or reflecting-only RISs provide half-space coverage, STAR-RISs allow full-space coverage. The hardware description of a STAR-RIS has been presented in [68], and, based on the field equivalence principle, a model for the signals transmitted and reflected by each atom has been provided. In [69], three operating protocols have been

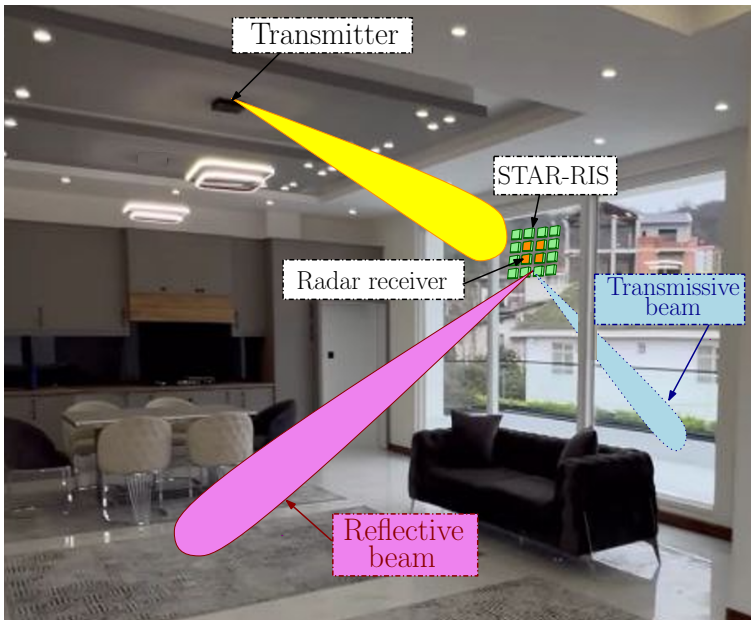

FIGURE 3.1: Graphical description of a STAR-RIS-based pulse-Doppler radar

proposed for a STAR-RIS, namely, Energy Splitting (ES), Mode Switching (MS), and Time Switching (TS). While past studies have mainly focused on using STAR-RISs in communication applications, to the best of the authors' knowledge, no previous work have investigated their specific usage in pulse-Doppler radars.

In this work, we propose the STAR-RIS-based pulse-Doppler radar architecture in Fig. 3.1, aiming to detect moving targets on both sides of the STAR-RIS in the presence of clutter. The transmitter illuminates the STAR-RIS that in turn redirects the signal in the transmissive and reflective half-spaces, while the radar receiver elaborates the reverberation from the environment. The receive antennas are collocated with the STAR-RIS and cover both half-spaces, so that a single processing chain implementing passband-to-baseband and analog-to-digital conversion is sufficient. The transmitter may be a dedicated feeder for a stand-alone system or an existing access

point which remotely enables the radar sensing at the STAR-RIS. To separate the echoes from the transmissive and reflective half-spaces, we propose to superimpose a slow-time (i.e., from pulse-to-pulse) amplitude/phase modulation on the signals redirected by the STAR-RIS during a Coherent Processing Interval (CPI); in particular, two practical scanning policies are introduced, referred to as simultaneous and sequential scanning, employing binary phase and on-off amplitude codes, respectively. At the radar receiver, a rule based on a GIC [62], [70] is employed to detect prospective targets on both sides of the STAR-RIS and estimate their radial velocity. Finally, a numerical example is provided to verify the effectiveness of the considered radar architecture and compare the performance-complexity tradeoffs of the proposed scanning policies.

The remainder of this chapter is organized as follows. Sec. 3.2 contains the system description. Sec. 3.3 illustrates the design of the STAR-RIS and radar receiver. Sec. 3.4 contains the numerical analysis. Finally, the conclusions are given in Sec. 3.5.

3.2 System description

In this work, we consider the STAR-RIS-based pulse-Doppler radar as illustrated in Fig. 3.2. The system operates at a carrier frequency f_o and comprises the following components:

- a transmitter equipped with a directional antenna;
- a STAR-RIS with N_{ris} tunable atoms;
- and a radar receiver equipped with N_{rx} antennas.

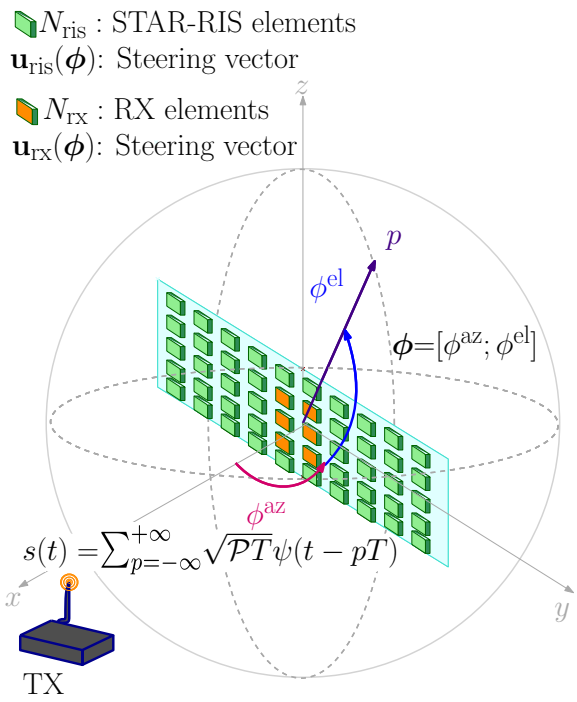

FIGURE 3.2: Coordinate reference system.

The whole space is divided by the STAR-RIS into two regions, namely, the transmissive and reflective half-spaces, with the former containing the transmitter. In this study, we make the following assumptions:

- The atoms of the STAR-RIS and the receive antennas are organized into two collocated uniform rectangular arrays; these arrays are on the (y,z)-plane of a Cartesian reference system centered at their center of gravity, with the positive x-axis pointing towards the reflective half-space; accordingly, the azimuth angle belongs to $(\pi/2, 3\pi/2)$ and $(-\pi/2, \pi/2)$ in the transmissive and reflective half-spaces, respectively.[2]

[2]Here, the azimuth angle of a point $\boldsymbol{p} \in \mathbb{R}^3$ is the angle between the x-axis and the orthogonal projection of the vector pointing towards $\boldsymbol{p}$ onto the (x,y)-plane, which is positive when going from the positive x-axis towards the positive y-axis, while the elevation angle is the angle between the vector pointing towards $\boldsymbol{p}$ and its orthogonal projection onto the (x,y)-plane, which is positive when going towards the positive z-axis from the (x,y)-plane.

- The baseband signal emitted by the transmitter is a periodic waveform with PRI T and average power $\mathcal{P}$, namely, $s(t) = \sum_{p=-\infty}^{+\infty} \sqrt{\mathcal{P}T}\psi(t-pT)$, where $\psi(t)$ is a unit-energy pulse with bandwidth B and support $[0, \Delta]$. The transmitter, STAR-RIS, and receiver are perfectly synchronized.

- The size of both the STAR-RIS and the receive array is much smaller than c/B, where c is the speed of light: this is the usual narrowband assumption [56]; also, any mutual coupling among their atoms/antennas is neglected.

- The radar receiver operates when the receive array (that is collocated with the STAR-RIS) is not illuminated by the transmitter to avoid direct interference. Interestingly, this implies the atoms of the STAR-RIS may be used also for sensing, if equipped with the necessary circuitry [71], [72]; in this latter case, the controller sets the atoms into the transmitting and/or reflecting mode when the pulses emitted by the transmitter hit the surface and into the sensing mode otherwise [71], [72]. This time-division operation introduces a constraint on the radar detectability range. Since the system avoids simultaneous transmission and reception, it must ensure that the echoes from the farthest target return to the receiver array while the system is still in receive mode. Specifically, the pulse duration Δ and T must satisfy the condition that the round-trip delay for the farthest target is less than the time remaining after transmission, i.e.,

$$2R_{\max}/c < T - \Delta,$$

where $R_{\max}$ is the maximum detectable range. This is a common constraint in pulse-Doppler radars and ensures that all target echoes arrive before the next transmission begins [57].

- The channel between the transmitter and STAR-RIS is known and denoted by $\boldsymbol{g} \in \mathbb{C}^{N_{\text{ris}}}$.

- The inspected region is in the far-field of the STAR-RIS and receive array. We denote by $\boldsymbol{u}_{\text{ris}}(\boldsymbol{\phi}) \in \mathbb{C}^{N_{\text{ris}}}$ and $\boldsymbol{u}_{\text{rx}}(\boldsymbol{\phi}) \in \mathbb{C}^{N_{\text{rx}}}$ the corresponding steering vectors towards the direction $\boldsymbol{\phi} = [\phi^{\text{az}}; \phi^{\text{el}}]$, respectively, where ϕ^{az} and ϕ^{el} are the azimuth and elevation angles; in particular, we have [56]

$$\boldsymbol{u}_{\text{ris}}(\boldsymbol{\phi}) = \boldsymbol{u}_{\text{ris},z} \otimes \boldsymbol{u}_{\text{ris},y}, \tag{3.1}$$

where:

$$\boldsymbol{u}_{\text{ris},y} = \left[1; \mathrm{e}^{\mathrm{i}\gamma_{\text{ris},y}}; \cdots; \mathrm{e}^{\mathrm{i}(N_{\text{ris},y}-1)\gamma_{\text{ris},y}}\right], \tag{3.2a}$$

$$\boldsymbol{u}_{\text{ris},z} = \left[1; \mathrm{e}^{\mathrm{i}\gamma_{\text{ris},z}}; \cdots; \mathrm{e}^{\mathrm{i}(N_{\text{ris},z}-1)\gamma_{\text{ris},z}}\right], \tag{3.2b}$$

$$\gamma_{\text{ris},y} = \frac{2\pi}{\lambda} d_{\text{ris}} \cos\phi^{\text{el}} \sin\phi^{\text{az}}, \tag{3.2c}$$

$$\gamma_{\text{ris},z} = \frac{2\pi}{\lambda} d_{\text{ris}} \sin\phi^{\text{el}}, \tag{3.2d}$$

where λ is the carrier wavelength, $N_{\text{ris},y}$ and $N_{\text{ris},z}$ are the number of elements along the y and z axes, respectively, $N_{\text{ris}} = N_{\text{ris},y} N_{\text{ris},z}$, and d_{ris} is the element spacing; $\boldsymbol{u}_{\text{rx}}(\boldsymbol{\phi})$ is similarly defined.

3.2.1 RIS response and power beam-pattern

The response of the STAR-RIS can be reconfigured at every PRI and is under the control of the system engineer; in particular, we denote by

$$\boldsymbol{x}_t(p) = \left[\beta_{t,1}(p)\mathrm{e}^{\mathrm{i}\omega_{t,1}(p)}; \cdots ; \beta_{t,N_{\mathrm{ris}}}(p)\mathrm{e}^{\mathrm{i}\omega_{t,N_{\mathrm{ris}}}(p)}\right] \tag{3.3a}$$

$$\boldsymbol{x}_r(p) = \left[\beta_{r,1}(p)\mathrm{e}^{\mathrm{i}\omega_{r,1}(p)}; \cdots ; \beta_{r,N_{\mathrm{ris}}}(p)\mathrm{e}^{\mathrm{i}\omega_{r,N_{\mathrm{ris}}}(p)}\right] \tag{3.3b}$$

the vectors containing the reflection and transmission coefficients of its atoms during the p-th PRI, respectively, with $\beta_{t,n}, \beta_{r,n} \geq 0$ and

$$\beta_{t,n}^2(p) + \beta_{r,n}^2(p) = 1, \tag{3.4}$$

where $\omega_{t,n}(p)$ and $\omega_{r,n}(p)$ denote the phase shifts applied by the n-th STAR-RIS element ($n = 1, \ldots, N_{\mathrm{ris}}$) in transmission and reflection sides, respectively, during the p-th PRI. Equivalently, it can be expressd as:

$$\left|[\boldsymbol{x}_t(p)]_n\right|^2 + \left|[\boldsymbol{x}_r(p)]_n\right|^2 = 1, \tag{3.5}$$

Accordingly, the p-th pulse redirected by the STAR-RIS towards the direction $\boldsymbol{\phi} = [\phi^{\mathrm{az}}; \phi^{\mathrm{el}}]$ is

$$\sqrt{\mathcal{P}TG_{\mathrm{ris}}(\boldsymbol{\phi})}\left(\boldsymbol{u}_{\mathrm{ris}}^{\mathsf{T}}(\boldsymbol{\phi})\mathrm{diag}\{\boldsymbol{x}(\boldsymbol{\phi}, p)\}\boldsymbol{g}\right)\psi(t - \delta - pT), \tag{3.6}$$

where $G_{\mathrm{ris}}(\boldsymbol{\phi})$ is the element gain of the STAR-RIS, δ is the propagation delay between the transmitter and STAR-RIS, and

$$\boldsymbol{x}(\boldsymbol{\phi}, p) = \begin{cases} \boldsymbol{x}_t(p), & \phi^{\mathrm{az}} \in (\pi/2, 3\pi/2), \\ \boldsymbol{x}_r(p), & \phi^{\mathrm{az}} \in (-\pi/2, \pi/2). \end{cases} \tag{3.7}$$

It is seen from (3.6) that $\boldsymbol{x}_t(p)$ and $\boldsymbol{x}_r(p)$ determine the power beampattern of the STAR-RIS during the p-th PRI, namely,

$$\mathrm{BP}_{\mathrm{ris}}(\boldsymbol{\phi}, p) = G_{\mathrm{ris}}(\boldsymbol{\phi}) \underbrace{\left| \boldsymbol{u}_{\mathrm{ris}}^{\mathsf{T}}(\boldsymbol{\phi}) \mathrm{diag}\{\boldsymbol{x}(\boldsymbol{\phi}, p)\} \boldsymbol{g} \right|^2}_{\mathrm{GF}_{\mathrm{ris}}(\boldsymbol{\phi}, p)}, \tag{3.8}$$

where $\mathrm{GF}_{\mathrm{ris}}(\boldsymbol{\phi}, p)$ is the array gain factor; hence, these vectors can be chosen to focus the STAR-RIS towards some desired angular directions [28] and, possibly, to introduce an slow-time modulation in the redirected signals [73]. Let $\mathcal{F}_t$ and $\mathcal{F}_r$ be the sets of angular directions to be monitored in the transmissive and reflective half-spaces, respectively. Over a CPI of length PT, the radar aims to inspect two angular directions, say $\boldsymbol{\phi}_t = [\phi_t^{\mathrm{az}}; \phi_t^{\mathrm{el}}] \in \mathcal{F}_t$ and $\boldsymbol{\phi}_r = [\phi_r^{\mathrm{az}}; \phi_r^{\mathrm{el}}] \in \mathcal{F}_r$, one in the transmissive half-space and one in the reflective half-space. In this setup, each CPI focuses on a single angular direction from each half-space. If the system is required to scan all directions in $\mathcal{F}_t$ and $\mathcal{F}_r$, then multiple CPIs must be used.

3.2.2 Radar received signal

For illustration, consider the CPI spanning the time segment $[0, PT)$, and denote by $\boldsymbol{b}(t) \in \mathbb{C}^{N_{\mathrm{rx}}}$ the baseband continuous-time signal collected by the receiver; also, denote by $\mathcal{T}$ the set of delays to be inspected by the radar, each one corresponding to a different range cell. For a given $\tau \in \mathcal{T}$,matched-filter pulse compression provides the following data samples

$$\boldsymbol{y}(p) = \int_{\mathbb{R}} \boldsymbol{b}(t) \psi^*\big(t - \delta - \tau - (p-1)T\big) dt \ \in \mathbb{C}^{N_{\mathrm{rx}}}, \tag{3.9}$$

for $p = 1, \ldots, P$. The tuples $(\boldsymbol{\phi}_t, \tau)$ and $(\boldsymbol{\phi}_r, \tau)$ specify the pair of resolution cells under inspection: we refer to them as the transmissive and reflective cells, respectively. Upon assuming that at most one target is present in each

resolution cell, $\boldsymbol{y}(p)$ can be expanded as

$$\begin{aligned}\boldsymbol{y}(p) = {} & \alpha_t \mathrm{e}^{\mathrm{i}2\pi\nu_t T(p-1)} \Big(\boldsymbol{u}_{\mathrm{ris}}^{\mathsf{T}}(\boldsymbol{\phi}_t)\mathrm{diag}\{\boldsymbol{x}_t(p)\}\boldsymbol{g}\Big)\boldsymbol{u}_{\mathrm{rx}}(\boldsymbol{\phi}_t) \\ & + \alpha_r \mathrm{e}^{\mathrm{i}2\pi\nu_r T(p-1)} \Big(\boldsymbol{u}_{\mathrm{ris}}^{\mathsf{T}}(\boldsymbol{\phi}_r)\mathrm{diag}\{\boldsymbol{x}_r(p)\}\boldsymbol{g}\Big)\boldsymbol{u}_{\mathrm{rx}}(\boldsymbol{\phi}_r) \\ & + \boldsymbol{z}(p) \in \mathbb{C}^{N_{\mathrm{rx}}}, \end{aligned} \tag{3.10}$$

where α_t and ν_t are the complex amplitude and Doppler shift of a prospective target in the transmissive cell, α_r and ν_r are the complex amplitude and Doppler shift of a prospective target in the reflective cell, and $\boldsymbol{z}(p)$ is the additive disturbance, including both clutter and noise (more on this in Sec. 3.2.3). Here, α_t and α_r account for the transmitted power $\mathcal{P}$, the two-way path-loss from the STAR-RIS to the target, and the target Radar Cross-Section (RCS); clearly, $\alpha_t = 0$ and $\alpha_r = 0$ if no target is present in the transmissive and reflective cells, respectively.

The observations in (3.10) are collected into the vector $\boldsymbol{y} = \big[\boldsymbol{y}(1); \cdots ; \boldsymbol{y}(P)\big]$; in particular, with the following definitions:

$$\boldsymbol{x}_t = [\boldsymbol{x}_t(1); \cdots ; \boldsymbol{x}_t(P)] \in \mathbb{C}^{PN_{\mathrm{ris}}}, \tag{3.11}$$

$$\boldsymbol{x}_r = [\boldsymbol{x}_r(1); \cdots ; \boldsymbol{x}_r(P)] \in \mathbb{C}^{PN_{\mathrm{ris}}}, \tag{3.12}$$

$$\boldsymbol{d}(\nu) = [1; \mathrm{e}^{\mathrm{i}2\pi T\nu}; \cdots ; \mathrm{e}^{\mathrm{i}2\pi\nu T(P-1)}] \in \mathbb{C}^{P}, \tag{3.13}$$

$$\boldsymbol{G}(\boldsymbol{\phi}) = \boldsymbol{I}_P \otimes \Big(\boldsymbol{u}_{\mathrm{ris}}^{\mathsf{T}}(\boldsymbol{\phi})\mathrm{diag}\{\boldsymbol{g}\}\Big) \in \mathbb{C}^{P\times PN_{\mathrm{ris}}}. \tag{3.14}$$

we have

$$\boldsymbol{y} = \alpha_t \boldsymbol{h}(\boldsymbol{x}_t, \boldsymbol{\phi}_t, \nu_t) + \alpha_r \boldsymbol{h}(\boldsymbol{x}_r, \boldsymbol{\phi}_r, \nu_r) + \boldsymbol{z} \in \mathbb{C}^{PN_{\mathrm{rx}}}, \tag{3.15}$$

where $\boldsymbol{z} = \big[\boldsymbol{z}(1); \cdots ; \boldsymbol{z}(P)\big]$ and

$$\boldsymbol{h}(\boldsymbol{x}, \boldsymbol{\phi}, \nu) = \big(\boldsymbol{d}(\nu) \odot \boldsymbol{G}(\boldsymbol{\phi})\boldsymbol{x}\big) \otimes \boldsymbol{u}_{\mathrm{rx}}(\boldsymbol{\phi}) \in \mathbb{C}^{PN_{\mathrm{rx}}} \tag{3.16}$$

is the *space-time* steering vector of a target with angular direction ϕ and Doppler shift ν when the STAR-RIS response vector in its half-space is $\boldsymbol{x}$. Notice that $\boldsymbol{u}_{\text{rx}}(\phi)$ and $\boldsymbol{d}(\nu) \odot \boldsymbol{G}(\phi)\boldsymbol{x}$ are the *spatial* and *temporal* steering vectors, respectively, and that a pulse-to-pulse variation of the STAR-RIS response induces a slow-time modulation in the temporal steering vector: this latter property will be exploited in Sec. 3.3.1 to devise suitable scanning policies.

3.2.3 Disturbance model

Assuming K_t and K_r clutter components in the reflective and transmissive half-spaces, respectively, we have

$$\boldsymbol{z} = \boldsymbol{z}_n + \sum_{k=1}^{K_t} \alpha_{t,k} \boldsymbol{h}(\boldsymbol{x}_t, \boldsymbol{\phi}_{t,k}, \nu_{t,k}) + \sum_{k=1}^{K_r} \alpha_{r,k} \boldsymbol{h}(\boldsymbol{x}_r, \boldsymbol{\phi}_{r,k}, \nu_{r,k}), \tag{3.17}$$

where $\boldsymbol{z}_n$ is the additive noise, $\alpha_{t,k}$, $\nu_{t,k}$, and $\boldsymbol{\phi}_{t,k} = [\phi^{\text{az}}_{t,k}; \phi^{\text{el}}_{t,k}]$ are the complex amplitude, Doppler shift, and direction of the k-th clutter component in the transmissive half-space, respectively, and $\alpha_{r,k}$, $\nu_{r,k}$, and $\boldsymbol{\phi}_{r,k} = [\phi^{\text{az}}_{r,k}; \phi^{\text{el}}_{r,k}]$ are the complex amplitude, Doppler shift, and direction of the k-th clutter component in the reflective half-space, respectively.

Hereafter, we model $\boldsymbol{z}_n$ as a circularly-symmetric Gaussian random vector with covariance matrix $\sigma_n^2 \boldsymbol{I}_{PN_{\text{rx}}}$ and $\alpha_{t,k}$ and $\alpha_{r,k}$ as independent circularly-symmetric Gaussian random variables with variance $\sigma^2_{t,k}$ and $\sigma^2_{r,k}$, respectively. Accordingly, the disturbance covariance matrix is

$$\begin{aligned} \boldsymbol{C} = \sigma_n^2 \boldsymbol{I}_{PN_{\text{rx}}} &+ \sum_{k=1}^{K_t} \sigma^2_{t,k} \boldsymbol{h}(\boldsymbol{x}_t, \boldsymbol{\phi}_{t,k}, \nu_{t,k}) \boldsymbol{h}^{\mathsf{H}}(\boldsymbol{x}_t, \boldsymbol{\phi}_{t,k}, \nu_{t,k}) \\ &+ \sum_{k=1}^{K_r} \sigma^2_{r,k} \boldsymbol{h}(\boldsymbol{x}_r, \boldsymbol{\phi}_{r,k}, \nu_{r,k}) \boldsymbol{h}^{\mathsf{H}}(\boldsymbol{x}_r, \boldsymbol{\phi}_{r,k}, \nu_{r,k}). \end{aligned} \tag{3.18}$$

In the following, $\boldsymbol{C}$ is assumed known: in practice, an estimate can be obtained by resorting to parametric or nonparametric algorithms, possibly aided by secondary data and/or some prior knowledge of the surrounding environment [74], [75], [76], [77]. Actually, since the clutter statistics may vary over time due to changes in the environment or the scanned angular direction, such estimation procedures may need to be repeated intermittently. This so-called re-training process ensures that the covariance model $\boldsymbol{C}$ remains accurate, especially in non-stationary scenarios.

3.3 System design

3.3.1 Proposed scanning policies

The echoes from the two half-spaces must be separable by the radar detector. Upon looking at (3.16), it is seen that the spatial steering vector alone cannot ensure such separability, since $\boldsymbol{u}_{\mathrm{rx}}([\phi^{\mathrm{az}};\phi^{\mathrm{el}}]) \propto \boldsymbol{u}_{\mathrm{rx}}([\pi-\phi^{\mathrm{az}};\phi^{\mathrm{el}}])$ for $\phi^{\mathrm{az}} \in (-\pi/2,\pi/2)$: this is a consequence of the fact that a single receive array simultaneously covers both half-spaces. This limitation can be overcome by exploiting the temporal steering vector $\boldsymbol{d}(\nu)\odot\boldsymbol{G}(\boldsymbol{\phi})\boldsymbol{x}$, which can be controlled by the STAR-RIS: the basic idea is that the STAR-RIS can superimpose a different slow-time modulation on the pulses redirected in each half-space, while focusing towards the desired angular directions.

To illustrate this idea, assume that $\boldsymbol{x}_t = \boldsymbol{c}_t \otimes \bar{\boldsymbol{x}}_t$ and $\boldsymbol{x}_r = \boldsymbol{c}_r \otimes \bar{\boldsymbol{x}}_r$, where $\bar{\boldsymbol{x}}_t$ and $\bar{\boldsymbol{x}}_r$ are N_{ris}–dimensional vectors with unit-modulus entries, while $\boldsymbol{c}_t$ and $\boldsymbol{c}_r$ are P–dimensional vectors with $\left|[\boldsymbol{c}_t]_p\right|^2 + \left|[\boldsymbol{c}_r]_p\right|^2 = 1$ for $p = 1,\dots,P$, so that the constraint in (3.5) is satisfied; accordingly, we have

$$\boldsymbol{h}(\boldsymbol{x}_t,\boldsymbol{\phi},\nu) = \boldsymbol{u}_{\mathrm{ris}}^{\mathsf{T}}(\boldsymbol{\phi})\mathrm{diag}\{\bar{\boldsymbol{x}}_t\}\boldsymbol{g}\Big[\big(\boldsymbol{d}(\nu)\odot\boldsymbol{c}_t\big)\otimes\boldsymbol{u}_{\mathrm{rx}}(\boldsymbol{\phi})\Big], \tag{3.19a}$$

$$\boldsymbol{h}(\boldsymbol{x}_r,\boldsymbol{\phi},\nu) = \boldsymbol{u}_{\mathrm{ris}}^{\mathsf{T}}(\boldsymbol{\phi})\mathrm{diag}\{\bar{\boldsymbol{x}}_r\}\boldsymbol{g}\Big[\big(\boldsymbol{d}(\nu)\odot\boldsymbol{c}_r\big)\otimes\boldsymbol{u}_{\mathrm{rx}}(\boldsymbol{\phi})\Big]. \tag{3.19b}$$

The vectors $\bar{\boldsymbol{x}}_t$ and $\bar{\boldsymbol{x}}_r$ control (up to a scaling factor) the array gain factor of the STAR-RIS in the transmissive and reflective half-spaces, respectively. Different criteria can be adopted to synthesize a desired power beampattern [45], [67], [78]; for illustration, $\bar{\boldsymbol{x}}_t$ and $\bar{\boldsymbol{x}}_r$ are chosen here to maximize the array gain factor towards ϕ_t and ϕ_r, respectively, whereby

$$[\bar{\boldsymbol{x}}_t]_n = \mathrm{e}^{-\mathrm{i}\left(\angle[\boldsymbol{g}]_n + \angle[\boldsymbol{u}_{\mathrm{rx}}(\phi_t)]_n\right)}, \tag{3.20a}$$

$$[\bar{\boldsymbol{x}}_r]_n = \mathrm{e}^{-\mathrm{i}\left(\angle[\boldsymbol{g}]_n + \angle[\boldsymbol{u}_{\mathrm{rx}}(\phi_r)]_n\right)}. \tag{3.20b}$$

Instead, the vectors $\boldsymbol{c}_t$ and $\boldsymbol{c}_r$ control the slow-time modulation superimposed on the signals redirected in the transmissive and reflective half-spaces, respectively. In order to separate the echoes from these half-spaces, we propose to use orthogonal code sequences, i.e., $\boldsymbol{c}_t^{\mathsf{H}}\boldsymbol{c}_r = 0$. In particular, upon assuming P even, we consider two practical scanning rules.

Simultaneous scanning

In this case, $[\boldsymbol{c}_t]_p = (-1)^n/\sqrt{2}$ and $[\boldsymbol{c}_r]_p = 1/\sqrt{2}$, for $p = 1, \ldots, P$, whereby the STAR-RIS simultaneously illuminates both half-spaces during the entire CPI by equally splitting the incoming energy [69]; the superimposed binary phase codes implement here a form of code-division multiple-access.

Sequential scanning

In this case, $[\boldsymbol{c}_t]_p = 1$ and $[\boldsymbol{c}_r]_p = 0$ for $p = 1, \ldots, P/2$ and $[\boldsymbol{c}_t]_p = 0$ and $[\boldsymbol{c}_r]_p = 1$ for $p = P/2 + 1, \ldots, P$, whereby the CPI is partitioned into two sub-intervals of duration $P/2$, and the STAR-RIS illuminates only one half-space in each sub-interval [69]; the adopted on-off codes implement here a form of time-division multiple-access.

3.3.2 Proposed GIC-based detector

The radar detector is faced with a composite hypothesis testing problem with four hypotheses: under the hypothesis $\mathcal{H}_0$, no target is present in both resolution cells; under $\mathcal{H}_{1,t}$ ($\mathcal{H}_{1,r}$), a target is present only in the transmissive (reflective) cell; under $\mathcal{H}_2$, a target is present in both resolution cells. The amplitude and Doppler shift of the prospective targets are unknown. To tackle this problem, we resort to a GIC [62], [70], whereby the selected hypothesis is

$$\hat{\mathcal{H}} = \underset{\mathcal{L}\in\{\mathcal{H}_0,\mathcal{H}_{1,t},\mathcal{H}_{1,r},\mathcal{H}_2\}}{\arg\max} \mu(\mathcal{L}), \tag{3.21}$$

where the objective function is defined as

$$\mu(\mathcal{L}) = \begin{cases} \ln f_{\mathcal{H}_0}(\boldsymbol{y}), & \text{if } \mathcal{L} = \mathcal{H}_0, \\ \max\limits_{\alpha_t\in\mathbb{C},\nu_t\in\mathcal{V}} \ln f_{\mathcal{H}_{1,t}}(\boldsymbol{y};\alpha_t,\nu_t) - \eta, & \text{if } \mathcal{L} = \mathcal{H}_{1,t}, \\ \max\limits_{\alpha_r\in\mathbb{C},\nu_r\in\mathcal{V}} \ln f_{\mathcal{H}_{1,r}}(\boldsymbol{y};\alpha_r,\nu_r) - \eta, & \text{if } \mathcal{L} = \mathcal{H}_{1,r}, \\ \max\limits_{\boldsymbol{\alpha}\in\mathbb{C}^2,\boldsymbol{\nu}\in\mathcal{V}^2} \ln f_{\mathcal{H}_2}(\boldsymbol{y};\boldsymbol{\alpha},\boldsymbol{\nu}) - 2\eta, & \text{if } \mathcal{L} = \mathcal{H}_2, \end{cases} \tag{3.22}$$

$f_{\mathcal{L}}(\boldsymbol{y};\cdot)$ is the likelihood function under $\mathcal{L}$, $\boldsymbol{\alpha} = [\alpha_t;\alpha_r]$, $\boldsymbol{\nu} = [\nu_t;\nu_r]$, $\mathcal{V}$ is Doppler search interval, and η is a penalty factor that can be set to control the false alarm rate under $\mathcal{H}_0$.

We define the following terms:

$$\boldsymbol{x} = [\boldsymbol{x}_t;\boldsymbol{x}_r], \tag{3.23a}$$

$$\boldsymbol{\phi} = [\boldsymbol{\phi}_t;\boldsymbol{\phi}_r], \tag{3.23b}$$

$$\boldsymbol{H}(\boldsymbol{x},\boldsymbol{\phi},\boldsymbol{\nu}) = [\boldsymbol{h}(\boldsymbol{x}_t,\boldsymbol{\phi}_t,\nu_t),\boldsymbol{h}(\boldsymbol{x}_r,\boldsymbol{\phi}_r,\nu_r)]. \tag{3.23c}$$

Therefore, we have:

$$\boldsymbol{\pi}_t(\nu_t) = \boldsymbol{C}^{-1}\boldsymbol{h}(\boldsymbol{x}_t, \boldsymbol{\phi}_t, \nu_t)/\|\boldsymbol{C}^{-\frac{1}{2}}\boldsymbol{h}(\boldsymbol{x}_t, \boldsymbol{\phi}_r, \nu_t)\|, \tag{3.24a}$$

$$\boldsymbol{\pi}_r(\nu_r) = \boldsymbol{C}^{-1}\boldsymbol{h}(\boldsymbol{x}_r, \boldsymbol{\phi}_r, \nu_r)/\|\boldsymbol{C}^{-\frac{1}{2}}\boldsymbol{h}(\boldsymbol{x}_r, \boldsymbol{\phi}_r, \nu_r)\|, \tag{3.24b}$$

$$\boldsymbol{\Pi}(\boldsymbol{\nu}) = \boldsymbol{C}^{-1}\boldsymbol{H}(\boldsymbol{x}, \boldsymbol{\phi}, \boldsymbol{\nu})\big(\boldsymbol{H}^{\mathsf{H}}(\boldsymbol{x}, \boldsymbol{\phi}, \boldsymbol{\nu})\boldsymbol{C}^{-1}\boldsymbol{H}(\boldsymbol{x}, \boldsymbol{\phi}, \boldsymbol{\nu})\big)^{-1/2}. \tag{3.24c}$$

Upon exploiting the fact that the disturbance is Gaussian and after some elaborations, the rule in (3.21) can be recast as [62]

$$\hat{\mathcal{H}} = \underset{\mathcal{L}\in\{\mathcal{H}_0,\mathcal{H}_{1,t},\mathcal{H}_{1,r},\mathcal{H}_2\}}{\arg\max}\ \tilde{\mu}(\mathcal{L}), \tag{3.25}$$

where the objective function is defined as

$$\tilde{\mu}(\mathcal{L}) = \begin{cases} 0, & \text{if } \mathcal{L} = \mathcal{H}_0, \\ \max\limits_{\nu_t\in\mathcal{V}} \left\|\boldsymbol{\pi}_t^{\mathsf{H}}(\nu_t)\boldsymbol{y}\right\|^2 - \eta, & \text{if } \mathcal{L} = \mathcal{H}_{1,t}, \\ \max\limits_{\nu_r\in\mathcal{V}} \left\|\boldsymbol{\pi}_r^{\mathsf{H}}(\nu_r)\boldsymbol{y}\right\|^2 - \eta, & \text{if } \mathcal{L} = \mathcal{H}_{1,r}, \\ \max\limits_{\boldsymbol{\nu}\in\mathcal{V}^2} \left\|\boldsymbol{\Pi}^{\mathsf{H}}(\boldsymbol{\nu})\boldsymbol{y}\right\|^2 - 2\eta, & \text{if } \mathcal{L} = \mathcal{H}_2. \end{cases} \tag{3.26}$$

When a target is declared in a given resolution cell, an estimate of its Doppler shift (and therefore of its radial velocity) is recovered from the corresponding argument maximizing the objective function in (3.26) under $\hat{\mathcal{H}}$.

Sequential scanning

Let $\boldsymbol{y}_t \in \mathbb{C}^{PN_{\text{ris}}/2}$ and $\boldsymbol{y}_r \in \mathbb{C}^{PN_{\text{ris}}/2}$ be the vectors containing the first and the last half entries of $\boldsymbol{y}$, i.e., $\boldsymbol{y} = [\boldsymbol{y}_t; \boldsymbol{y}_r]$. When using a sequential scanning, $\boldsymbol{y}_t$ and $\boldsymbol{y}_r$ only contain echoes originated from the transmissive and reflective half-spaces, respectively. Upon exploiting this property, the implementation of (3.25) can be simplified; it particular, two independent binary tests

can be run in each half-space, namely,

$$\max_{\nu_t \in \mathcal{V}} \left\| \overline{\boldsymbol{\pi}}_t^{\mathsf{H}}(\nu_t) \boldsymbol{y}_t \right\|^2 \underset{\mathcal{H}_{0,t}^{\text{seq}}}{\overset{\mathcal{H}_{1,t}^{\text{seq}}}{\gtrless}} \eta, \tag{3.27a}$$

$$\max_{\nu_r \in \mathcal{V}} \left\| \underline{\boldsymbol{\pi}}_r^{\mathsf{H}}(\nu_r) \boldsymbol{y}_r \right\|^2 \underset{\mathcal{H}_{0,r}^{\text{seq}}}{\overset{\mathcal{H}_{1,r}^{\text{seq}}}{\gtrless}} \eta, \tag{3.27b}$$

where $\overline{\boldsymbol{\pi}}_t \in \mathbb{C}^{PN_{\text{ris}}/2}$ contains the first half entries of $\boldsymbol{\pi}_t$, while $\underline{\boldsymbol{\pi}}_r \in \mathbb{C}^{PN_{\text{ris}}/2}$ the second half entries of $\boldsymbol{\pi}_r$; then, a decision is taken as follows: $\mathcal{H}_0$ is declared if $\mathcal{H}_{0,t}^{\text{seq}}$ and $\mathcal{H}_{0,r}^{\text{seq}}$ are true; $\mathcal{H}_{1,t}$ is declared if $\mathcal{H}_{1,t}^{\text{seq}}$ and $\mathcal{H}_{0,r}^{\text{seq}}$ are true; $\mathcal{H}_{1,r}$ is declared if $\mathcal{H}_{0,t}^{\text{seq}}$ and $\mathcal{H}_{1,r}^{\text{seq}}$ are true; $\mathcal{H}_2$ is declared if $\mathcal{H}_{1,t}^{\text{seq}}$ and $\mathcal{H}_{1,r}^{\text{seq}}$ are true. As compared to (3.25), not only the joint Doppler search under $\mathcal{H}_2$ is avoided, but also the involved vectors and matrices have smaller size: for example, it can be shown

$$\overline{\boldsymbol{\pi}}_t(\nu_t) = \overline{\boldsymbol{C}}^{(-1)} \overline{\boldsymbol{h}}(\boldsymbol{x}_t, \boldsymbol{\phi}_t, \nu_t) / \| \overline{\boldsymbol{C}}^{(-1/2)} \overline{\boldsymbol{h}}(\boldsymbol{x}_t, \boldsymbol{\phi}_t, \nu_t) \|, \tag{3.28}$$

where $\overline{\boldsymbol{h}}(\boldsymbol{x}_t, \boldsymbol{\phi}_t, \nu_t)$ contains the first half entries of $\boldsymbol{h}(\boldsymbol{x}_t, \boldsymbol{\phi}_t, \nu_t)$ and $\overline{\boldsymbol{C}}$ is the submatrix of $\boldsymbol{C}$ with the first half rows and columns.

3.4 Numerical results

We consider a system employing a carrier frequency $f_o = 28$ GHz, a bandwidth $B = 50$ MHz, a STAR-RIS and a receive array with 16 elements along the y-axis and 8 along the z-axis (whereby $N_{\text{ris}} = N_{\text{rx}} = 128$), rectangular probing pulses, $T = 0.5$ ms, and $P = 8, 16, 32$. Notice that the unambiguous Doppler interval is here $(-\nu_{\max}, \nu_{\max})$, with $\nu_{\max} = 1/(2T) = 1$ kHz; this latter value corresponds to a radial velocity of $c\nu_{\max}/(2f_o) \simeq 5.3$ m/s [57], which may be sufficient for low-mobility applications. Also, for the same CPI, simultaneous and sequential scanning presents a different Doppler

resolution of $1/(PT)$ and $2/(PT)$, since they elaborate P and $P/2$ consecutive pulses from each resolution cell under inspection, receptively [57]; if $P = 16$, the Doppler resolution for simultaneous scanning is 125 Hz, corresponding to a radial velocity of about 0.7 m/s.

The entries of channel from the transmitter to STAR-RIS are drawn from a complex Gaussian distribution. As to the targets, their directions and Doppler shifts are randomly generated, with $\boldsymbol{\phi}_t \in (155^\circ, 160^\circ) \times (20^\circ, 25^\circ)$, $\boldsymbol{\phi}_r \in (20^\circ, 25^\circ) \times (20^\circ, 25^\circ)$, and $\nu_t, \nu_r \in (500, 1000)$ Hz; also, α_t and α_r are drawn from a circularly-symmetric Gaussian distribution with variance σ_t^2 and σ_r^2, respectively, corresponding to a Swerling I fluctuation model [57]. Both targets have the same signal-to-noise ratio per pulse, defined as

$$\mathrm{SNR_p} = \frac{\sigma_t^2 \|\boldsymbol{h}(\boldsymbol{x}_t, \boldsymbol{\phi}_t, \nu_t)\|^2}{P\sigma_n^2} = \frac{\sigma_r^2 \|\boldsymbol{h}(\boldsymbol{x}_r, \boldsymbol{\phi}_r, \nu_r)\|^2}{P\sigma_n^2}. \tag{3.29}$$

As to clutter components, $K_t = K_r = 10$, and their directions and Doppler shifts are randomly generated, with $\boldsymbol{\phi}_{t,k} \in (200^\circ, 220^\circ) \times (-40^\circ, -20^\circ)$, $\boldsymbol{\phi}_{r,q} \in (-40^\circ, -20^\circ) \times (-40^\circ, -20^\circ)$, and $\nu_{r,k}, \nu_{t,q} \in (-125, 125)$ Hz, for $k = 1, \ldots, K_t$ and $q = 1, \ldots, K_r$; also, they all have a clutter-to-noise ratio per pulse of 20 dB, defined as

$$\mathrm{CNR_p} = \frac{\sigma_{t,k}^2 \|\boldsymbol{h}(\boldsymbol{x}_t, \boldsymbol{\phi}_{t,k}, \nu_{t,k})\|^2}{P\sigma_n^2} = \frac{\sigma_{r,q}^2 \|\boldsymbol{h}(\boldsymbol{x}_r, \boldsymbol{\phi}_{r,q}, \nu_{r,q})\|^2}{P\sigma_n^2}. \tag{3.30}$$

The STAR-RIS response is set according to (3.20); for example, Fig. 3.4 and Fig. 3.5 report the resulting normalized array gain factor in the reflective half-space with $\boldsymbol{\phi}_r = [22^\circ; 22^\circ]$ and in the transmissive half-space with $\boldsymbol{\phi}_t = [158^\circ; 22^\circ]$, respectively. Fig. 3.3 shows the STAR-RIS array power patterns. Finally, η is chosen to have an average number of false alarms per CPI under $\mathcal{H}_0$ equal to 10^{-3}.

Fig. 3.6 reports the probability of declaring $\mathcal{H}_2$ when $\mathcal{H}_2$ is true (shortly,

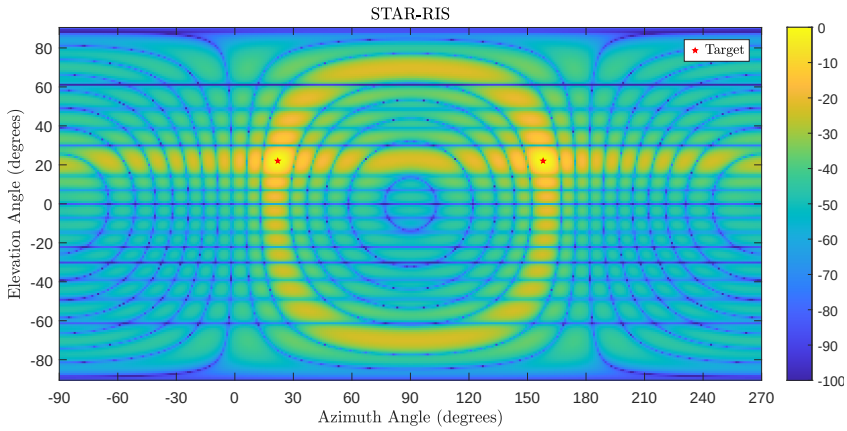

FIGURE 3.3: STAR-RIS array power patterns. Target locations are indicated by red star markers.

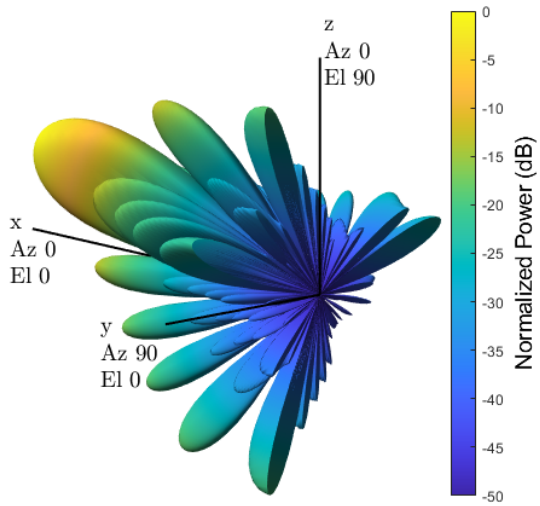

FIGURE 3.4: Normalized array gain factor of the STAR-RIS in the reflective half-space, when the design in (3.20) is employed and $\phi_r = [22°; 22°]$.

PD) and the corresponding RMSE in the estimation of the target radial velocity (averaged over both targets) versus the $\mathrm{SNR_p}$, for $P = 8, 16, 32$. Both scanning policies substantially present the same PD for the same value of P,

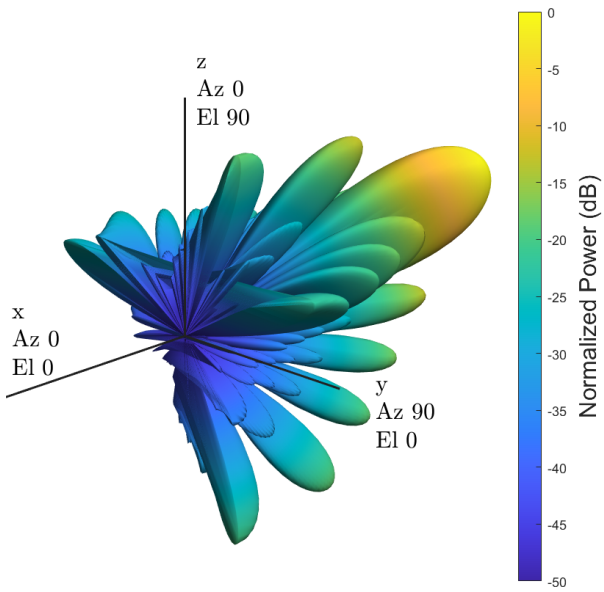

FIGURE 3.5: Normalized array gain factor of the STAR-RIS in the transmissive half-space, when the design in (3.20) is employed and $\phi_t = [158°; 22°]$.

as they redirect the same amount of energy in the two half-spaces in a given CPI. Instead, simultaneous scanning provides a lower RMSE than sequential scanning, since more pulses are elaborated from each resolution cell during the same CPI: this comes at price of a larger implementation complexity of the radar detector, as described in Sec. 3.3.2. Finally, doubling P results into an energy integration gain of 3 dB for both scanning policies, as evident from the shift of the PD curves, and into a smaller Doppler resolution; when looking at the RMSE curves, both these effects help improving the velocity estimation.

3.5 Conclusions

This chapter has introduced a STAR-RIS-based pulse-Doppler radar with sensing at the STAR-RIS location. After introducing a convenient signal

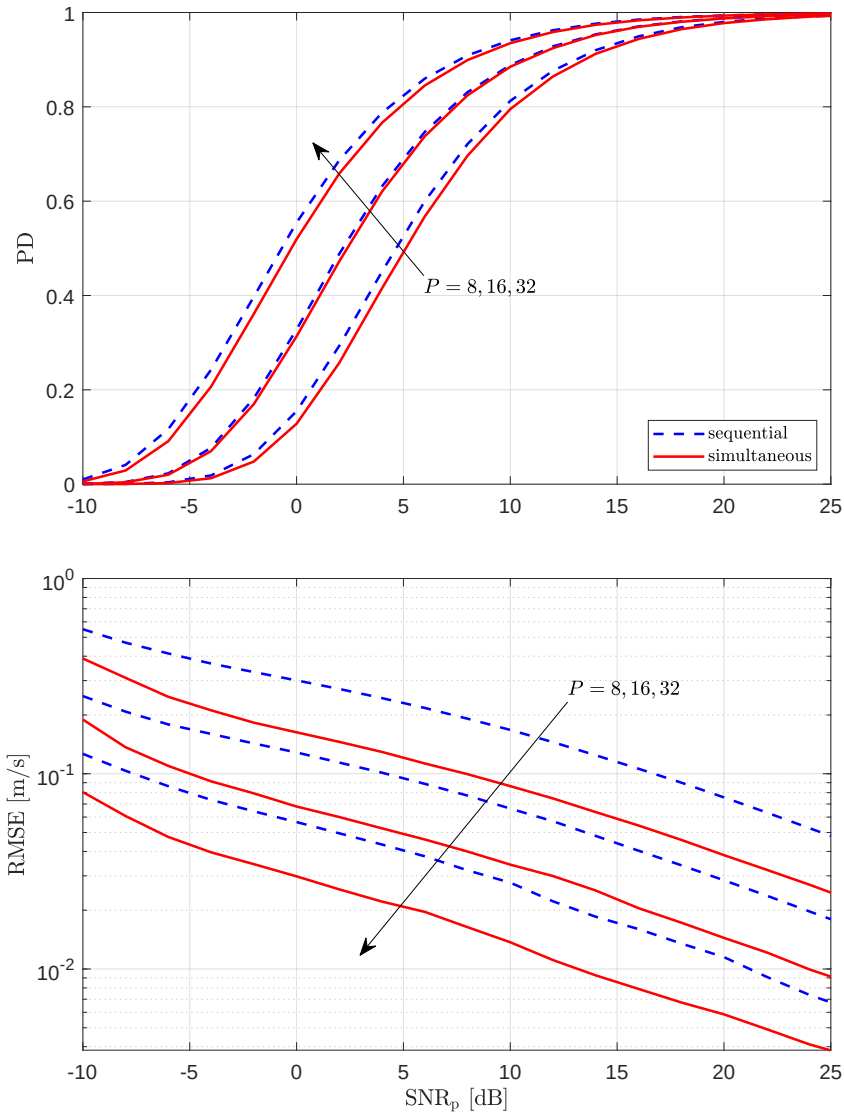

FIGURE 3.6: PD and RMSE in the radial velocity estimation versus $\mathrm{SNR_p}$.

model, we have proposed two scanning policies to ensure separability of the echoes received from the transmissive and reflective half-spaces, and we have devised a decision rule based on a GIC for joint target detection and radial velocity estimation. The analysis indicates that simultaneous

scanning provides a better radial velocity estimation than sequential scanning, at the price of a larger complexity of the radar detector.

Chapter 4

Radar-Centric ISAC System Using Passive STAR-RIS

This chapter is based on articles published in the Proceedings of the *2025 33rd European Signal Processing Conference (EUSIPCO)* [79], and in the *IEEE Open Journal of the Communications Society* , 2025 [80].

4.1 Introduction

The exponential growth in wireless data traffic, coupled with the increasing demand for ubiquitous connectivity and resource efficiency, has spurred the development of novel paradigms for future wireless networks. Among these, RISs have emerged as a compelling solution capable of redefining the wireless propagation environment in beyond-5G systems [33], [37], [81], [82], [83]. By intelligently altering the electromagnetic behavior of incident signals, RISs enable a fine-grained control of wireless channels. Their integration into wireless systems offers a host of advantages, including enhanced spectral and energy efficiency, extended coverage, and reduced infrastructure costs. Furthermore, RISs can embed information onto the

reflected signals by dynamically adjusting their spatial and temporal responses, thereby enabling the realization of low-cost RIS-based transmitters [20], [21], [22], [73], [84], [85]. RIS architectures can generally be classified into passive[3] and active types. Passive RISs consist of low-power elements without any RF circuitry and are particularly attractive due to their energy efficiency, scalability, and ease of deployment [6], [86]. In contrast, active RISs integrate amplifiers and/or RF components, which allow for power amplification of the redirected signals and enable advanced signal processing functionalities, albeit at the cost of increased complexity and energy consumption [28], [60], [87]. A related concept is Hybrid Reconfigurable Intelligent Surface (HRIS) [88], which combines active and passive elements to mitigate severe path loss and improve robustness against channel estimation errors, particularly in UAV-assisted ISAC systems. HRIS has shown potential in enhancing system performance under challenging propagation conditions, though it introduces additional hardware complexity and power consumption. Based on their capability to redirect incident signals, RISs are further categorized as reflective, transmissive, or simultaneously transmitting and reflecting, the latter being known as STAR-RISs [68], [69], [89], [90]. STAR-RISs have gained considerable interest due to their ability to extend coverage and increase deployment flexibility. Three practical operating protocols for STAR-RISs are introduced in [69]: the ES protocol, which allows each RIS element to reflect and transmit simultaneously by allocating a predefined energy ratio in each direction; the MS protocol, in which each element operates in either reflection or transmission

[3]While we adopt the standard term "passive" here, "nearly passive" is more precise. This is because control circuits are still needed to reconfigure the surfaces, although the power drawn is minimal compared to the power that would be required if RF chains and amplifiers were present.

mode at any given time; and the TS protocol, where the entire surface alternates between reflection and transmission over time. This study focuses on STAR-RISs operating in the ES and TS modes, with a fully passive hardware implementation. While our system-level design is the primary concern, it is important to acknowledge that STAR-RIS implementations are subject to practical hardware constraints such as phase quantization, nonlinearities, and limited switching speeds. Recent studies [91], [92], [93], [94], [95] have shown that such impairments can significantly impact the performance of metasurface-based architectures in real applications.

In parallel, ISAC has been identified as a fundamental enabler of next-generation wireless systems. ISAC seeks to unify communication and sensing functionalities within a shared platform, thereby achieving efficient utilization of spectral, hardware, and energy resources [17], [26], [27], [96]. Owing to the inherent synergies between STAR-RIS and ISAC, several recent studies have explored their integration to enhance overall system performance [97]. The literature has addressed diverse aspects of this integration, including joint waveform and beamforming design, user mobility management, security provisioning, fairness, and hardware considerations [71], [98], [99], [100], [101], [102], [103], [104]. Despite these advancements, most current approaches rely on communication-centric random waveforms, assume full-duplex operation, multi-channel digital transceivers, instantaneous CSI, and high computational complexity. These factors substantially increase the cost and complexity of practical deployment, and motivate the need for low-cost and scalable alternatives. Starting from the preliminary concepts introduced in [63], [79], this work proposes a radar-centric ISAC transceiver architecture (Fig. 4.1) consisting of a directional feeder, a passive STAR-RIS, and a co-located radar receiver.

The feeder illuminates the STAR-RIS with periodic pulsed waveforms. The STAR-RIS applies space-time modulation to the redirected signals, while the radar receiver, equipped with a PESA and a single digital channel, captures the echoes for joint sensing and communication purposes. The radar operates in time-duplex mode to avoid self-interference with the feeder. The two-way array power pattern of the monostatic radar is derived as the product of the STAR-RIS and PESA array responses. A joint optimization of the STAR-RIS spatial response and the radar analog beamformer is developed to maximize signal power in target directions while suppressing clutter and minimizing interference toward communication users. This nonconvex problem is tackled using the augmented Lagrangian method with partial constraint elimination. Two encoding schemes based on ES and TS operation are introduced to govern the STAR-RIS time-modulation across PRIs. The first enables simultaneous illumination of both half-spaces, while the second supports sequential operation. Both employ orthogonal binary codewords that provide unique signatures for radar detection and facilitate blind data decoding for communication users. Under this architecture, radar detection is cast as a composite hypothesis testing problem, whereas the communication receiver performs blind channel estimation and maximum-likelihood decoding. Model order selection for both sensing and communication tasks is addressed using the GIC [70]. Comprehensive numerical analysis is conducted to assess the system performance in terms of BER, transmission rate, PD , and RMSE for target velocity estimation. The proposed design enables flexible trade-offs between sensing and communication functionalities by reshaping the STAR-RIS and PESA beam patterns and tuning the time-modulation parameters, making it a promising

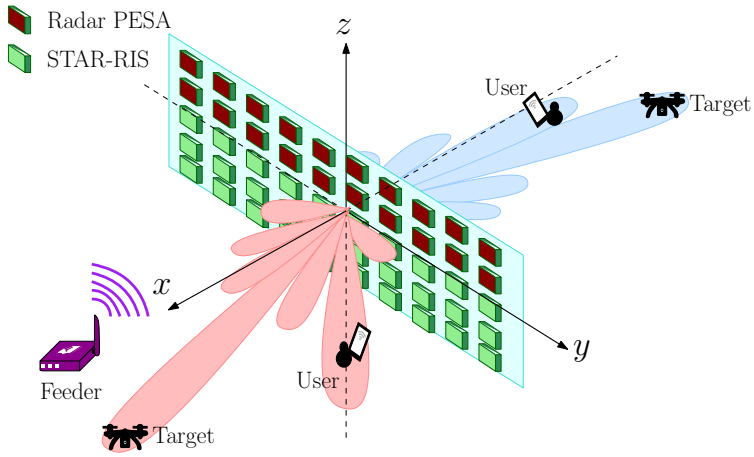

FIGURE 4.1: Considered system architecture.

and practical solution for future ISAC systems. The remainder of this chapter is organized as follows. Section 4.2 introduces the system model and key assumptions. Section 4.3 details the design of the STAR-RIS response and receiver architectures. Section 4.4 presents the performance evaluation. Finally, Section 4.5 concludes the chapter.

4.2 System description

In this section, we consider the system illustrated in Fig. 4.1, which operates at the carrier frequency f_o. The feeder is equipped with a directional antenna that illuminates the STAR-RIS and emits the baseband pulse train given by

$$\sum_{p=-\infty}^{+\infty} \sqrt{\mathcal{E}}\psi(t - pT + \delta), \tag{4.1}$$

where $\psi(t)$ is a unit-energy pulse with bandwidth B, which is zero for $t \notin [0, \Delta)$, with $\Delta \simeq 1/B$; $\mathcal{E} = \mathcal{P}\Delta$ denotes the pulse energy; $\mathcal{P}$ is the pulse power; T is PRI satisfying $T \gg \Delta$; and δ represents the time of flight between the feeder and the STAR-RIS. The feeder may be a dedicated device or a collaborative access point.

The STAR-RIS has N_{ris} atoms and divides the space into the transmissive and reflective half-spaces. The STAR-RIS aims to illuminate the angular region monitored by the radar receiver and to communicate with a single antenna user in each half-space. Users do not experience multiple access interference due to the spatial separation induced by the STAR-RIS. The radar receiver is equipped with a PESA containing N_{rad} antennas that simultaneously collects the echoes from both half-spaces. The STAR-RIS and PESA elements are organized into two collocated uniform rectangular arrays, which lay on the (y, z)-plane of a Cartesian reference system centered at their center of gravity, as shown in Fig. 4.1, with the positive x-axis pointing towards the reflective half-space; hence, the azimuth angle belongs to $(\pi/2, 3\pi/2)$ and $(-\pi/2, \pi/2)$ in the transmissive and reflective half-spaces, respectively. After analog beamforming, the radar elaborates the received signal via a single digital channel over a CPI spanning P PRIs. Without loss of generality, the CPI $[0, PT)$ is considered for illustration.

To proceed with the analysis, the following assumptions are made:

- The sizes of the STAR-RIS and of the radar receiving array are much smaller than c/B, where c is the speed of light (narrowband assumption [56]); also, any mutual coupling among their atoms/antennas is neglected.

- The STAR-RIS and radar receiver are synchronized and aware of the feeder's timing. The synchronization between STAR-RIS and radar receiver can be easily achieved since the two systems are collocated and (possibly) share the same clock. To avoid direct interference, the radar receiver operates when the feeder is not transmitting; consequently, the STAR-RIS atoms may also be used for reception if

equipped with necessary circuitry[72].

- The channel $\boldsymbol{g} \in \mathbb{C}^{N_{\text{ris}}}$ between the feeder and STAR-RIS is known to the STAR-RIS-based transceiver, and it remains constant over the CPI. This can easily be achieved, as the feeder and the STAR-RIS belong to the same network and are coordinated by a common control unit.

- Prospective targets are point-like and located in the far-field of the STAR-RIS and the radar PESA.

- The users do not have instantaneous CSI; specifically, angles of arrival, amplitudes, and delays of the multipath channel are unknown. They only have statistical information about the channel's delay spread and are aware of the encoder timing.

- The STAR-RIS does not have instantaneous CSI; specifically, angles of departure, amplitudes, and delays of the multipath channel are unknown. It may only have some prior information about the users' locations, encapsulated in the uncertainty set where the angles of departure belong.

For subsequent reference, let $\boldsymbol{\phi} = [\phi^{\text{az}}; \phi^{\text{el}}]$ denote an angular direction characterized by azimuth angle ϕ^{az} and elevation angle ϕ^{el}. Accordingly, the sets

$$\mathcal{F}_{\text{tr}} = \left(\frac{\pi}{2}, \frac{3\pi}{2}\right) \times \left(-\frac{\pi}{2}, \frac{\pi}{2}\right) \quad \text{and} \quad \mathcal{F}_{\text{re}} = \left(-\frac{\pi}{2}, \frac{\pi}{2}\right) \times \left(-\frac{\pi}{2}, \frac{\pi}{2}\right)$$

contain all angular directions in the transmissive and reflective half-spaces, respectively, while

$$\mathcal{F} = \mathcal{F}_{\text{tr}} \cup \mathcal{F}_{\text{re}}$$

specifies the entire field of view.

Moreover, let $G_{\text{ris}}(\phi)$ and $G_{\text{rad}}(\phi)$ denote the element gains of the STAR-RIS and the radar receiving array towards direction ϕ, respectively. Finally, the steering vectors of the STAR-RIS and radar receiving array toward ϕ are given by $\boldsymbol{u}_{\text{ris}}(\phi) \in \mathbb{C}^{N_{\text{ris}}}$ and $\boldsymbol{u}_{\text{rad}}(\phi) \in \mathbb{C}^{N_{\text{rad}}}$, respectively; in particular, the radar steering vector is expressed as [56]

$$\boldsymbol{u}_{\text{rad}}(\phi) = \left[1; \mathrm{e}^{\mathrm{i}\frac{2\pi d_{\text{rad}}}{\lambda}\sin\phi^{\text{el}}}; \cdots; \mathrm{e}^{\mathrm{i}(N_{\text{rad},z}-1)\frac{2\pi d_{\text{rad}}}{\lambda}\sin\phi^{\text{el}}}\right] \otimes \left[1; \mathrm{e}^{\mathrm{i}\frac{2\pi d_{\text{rad}}}{\lambda}\cos\phi^{\text{el}}\sin\phi^{\text{az}}}; \cdots; \mathrm{e}^{\mathrm{i}(N_{\text{rad},y}-1)\frac{2\pi d_{\text{rad}}}{\lambda}\cos\phi^{\text{el}}\sin\phi^{\text{az}}}\right], \quad (4.2)$$

where λ is the carrier wavelength, $N_{\text{rad},y}$ and $N_{\text{rad},z}$ are the number of antenna elements along the y and z axes, respectively, such that $N_{\text{rad}} = N_{\text{rad},y}N_{\text{rad},z}$, and d_{rad} is the element spacing. The STAR-RIS steering vector $\boldsymbol{u}_{\text{ris}}(\phi)$ is defined analogously. Finally, to aid in following the system's description and the mathematical derivations, a list of key variables and symbols defined and used throughout this section is provided in Tables 4.1 and 4.2.

4.2.1 Space-time response of the STAR-RIS

This subsection describes the response of the STAR-RIS in both transmissive and reflective half-spaces during the p-th PRI. The signals emitted in the two directions are modeled as follows:

$$c_{\text{tr}}(p)\boldsymbol{s}_{\text{tr}} \in \mathbb{C}^{N_{\text{ris}}}, \quad (4.3a)$$

$$c_{\text{re}}(p)\boldsymbol{s}_{\text{re}} \in \mathbb{C}^{N_{\text{ris}}}, \quad (4.3b)$$

where $\boldsymbol{s}_{\text{tr}}$ and $\boldsymbol{s}_{\text{re}}$ are unit-modulus spatial beamformers of dimension N_{ris}, and $c_{\text{tr}}(p)$ and $c_{\text{re}}(p)$ are complex scalars satisfying the normalization condition $|c_{\text{tr}}(p)|^2 + |c_{\text{re}}(p)|^2 = 1$, for $p = 0, \ldots, P-1$.

TABLE 4.1: List of key variables and symbols

λ = Carrier wavelength
T = Pulse repetition interval
$\mathcal{E}$ = Pulse energy
N_{ris} = Number of elements of the STAR-RIS
N_{rad} = Number of elements of the radar PESA
$G_{\text{ris}}(\phi)$ = Element gain of the STAR-RIS
$G_{\text{rad}}(\phi)$ = Element gain of the radar PESA
$\boldsymbol{g}$ = Radar transmitter to STAR-RIS channel
P = Number of pulses in the CPI at the radar receiver
$\mathcal{F}_{\text{tr}}$ = Angular directions in the tr. side
$\mathcal{F}_{\text{re}}$ = Angular directions in the re. side
$\mathcal{F} = \mathcal{F}_{\text{tr}} \cup \mathcal{F}_{\text{re}}$ = STAR-RIS field of view
$\boldsymbol{u}_{\text{ris}}(\phi)$ = Steering vector of the STAR-RIS
$\boldsymbol{u}_{\text{rad}}(\phi)$ = Steering vector of the radar PESA
$\boldsymbol{s}_{\text{rad}}$ = Radar receiver analog beamformer
$c_{\text{tr}}(p)\boldsymbol{s}_{\text{tr}}$ = STAR-RIS space-time response (tr. side)
$c_{\text{re}}(p)\boldsymbol{s}_{\text{re}}$ = STAR-RIS space-time response (re. side)
$\boldsymbol{c}_{\text{tr}} = [c_{\text{tr}}(0); \cdots ; c_{\text{tr}}(P-1)]$ = Code sequence (tr. side)
$\boldsymbol{c}_{\text{re}} = [c_{\text{re}}(0); \cdots ; c_{\text{re}}(P-1)]$ = Code sequence (re. side)

TABLE 4.2: List of key variables and symbols

$$\mathrm{A}_{\mathrm{tr}}(\boldsymbol{\phi};\boldsymbol{s}_{\mathrm{tr}}) = |\boldsymbol{u}_{\mathrm{ris}}^{\mathsf{T}}(\boldsymbol{\phi})\mathrm{diag}\{\boldsymbol{s}_{\mathrm{tr}}\}\boldsymbol{g}|^2\|\boldsymbol{g}\|_1^{-2}\mathbb{1}_{\{\boldsymbol{\phi}\in\mathcal{F}_{\mathrm{tr}}\}}$$
$$= \text{STAR-RIS array power pattern (tr. side)}$$

$$\mathrm{A}_{\mathrm{re}}(\boldsymbol{\phi};\boldsymbol{s}_{\mathrm{re}}) = |\boldsymbol{u}_{\mathrm{ris}}^{\mathsf{T}}(\boldsymbol{\phi})\mathrm{diag}\{\boldsymbol{s}_{\mathrm{re}}\}\boldsymbol{g}|^2\|\boldsymbol{g}\|_1^{-2}\mathbb{1}_{\{\boldsymbol{\phi}\in\mathcal{F}_{\mathrm{re}}\}}$$
$$= \text{STAR-RIS array power pattern (re. side)}$$

$$\mathrm{A}_{\mathrm{ris}}(\boldsymbol{\phi};\boldsymbol{s}_{\mathrm{tr}},\boldsymbol{s}_{\mathrm{re}}) = \mathrm{A}_{\mathrm{tr}}(\boldsymbol{\phi};\boldsymbol{s}_{\mathrm{tr}}) + \mathrm{A}_{\mathrm{re}}(\boldsymbol{\phi};\boldsymbol{s}_{\mathrm{re}})$$
$$= \text{Array power pattern of the STAR-RIS}$$

$$\mathrm{A}_{\mathrm{rad}}(\boldsymbol{\phi};\boldsymbol{s}_{\mathrm{rad}}) = |\boldsymbol{s}_{\mathrm{rad}}^{\mathsf{H}}\boldsymbol{u}_{\mathrm{rad}}(\boldsymbol{\phi})|^2 N_{\mathrm{rad}}^{-2}$$
$$= \text{Array power pattern of the radar PESA}$$

$$\mathrm{A}(\boldsymbol{\phi};\boldsymbol{s}_{\mathrm{tr}},\boldsymbol{s}_{\mathrm{re}},\boldsymbol{s}_{\mathrm{rad}}) = \mathrm{A}_{\mathrm{rad}}(\boldsymbol{\phi};\boldsymbol{s}_{\mathrm{rad}})\mathrm{A}_{\mathrm{ris}}(\boldsymbol{\phi};\boldsymbol{s}_{\mathrm{tr}},\boldsymbol{s}_{\mathrm{re}})$$
$$= \text{Two-way array power pattern}$$

$$\gamma_{\mathrm{tr}}(\boldsymbol{\phi};\boldsymbol{s}_{\mathrm{tr}},\boldsymbol{s}_{\mathrm{rad}}) = \sqrt{\tfrac{\mathcal{E}G_{\mathrm{rad}}(\boldsymbol{\phi})G_{\mathrm{ris}}(\boldsymbol{\phi})\lambda^2}{4\pi N_{\mathrm{rad}}}}\left(\boldsymbol{s}_{\mathrm{rad}}^{\mathsf{H}}\boldsymbol{u}_{\mathrm{rad}}(\boldsymbol{\phi})\right)$$
$$\times \left(\boldsymbol{u}_{\mathrm{ris}}^{\mathsf{T}}(\boldsymbol{\phi})\mathrm{diag}\{\boldsymbol{g}\}\boldsymbol{s}_{\mathrm{tr}}\right)\mathbb{1}_{\{\boldsymbol{\phi}\in\mathcal{F}_{\mathrm{tr}}\}}$$
$$= \text{Two-way field response (tr. side)}$$

$$\gamma_{\mathrm{re}}(\boldsymbol{\phi};\boldsymbol{s}_{\mathrm{re}},\boldsymbol{s}_{\mathrm{rad}}) = \sqrt{\tfrac{\mathcal{E}G_{\mathrm{rad}}(\boldsymbol{\phi})G_{\mathrm{ris}}(\boldsymbol{\phi})\lambda^2}{4\pi N_{\mathrm{rad}}}}\left(\boldsymbol{s}_{\mathrm{rad}}^{\mathsf{H}}\boldsymbol{u}_{\mathrm{rad}}(\boldsymbol{\phi})\right)$$
$$\times \left(\boldsymbol{u}_{\mathrm{ris}}^{\mathsf{T}}(\boldsymbol{\phi})\mathrm{diag}\{\boldsymbol{g}\}\boldsymbol{s}_{\mathrm{re}}\right)\mathbb{1}_{\{\boldsymbol{\phi}\in\mathcal{F}_{\mathrm{re}}\}}$$
$$= \text{Two-way field response (re. side)}$$

$$\gamma(\boldsymbol{\phi};\boldsymbol{s}_{\mathrm{tr}},\boldsymbol{s}_{\mathrm{re}},\boldsymbol{s}_{\mathrm{rad}}) = \gamma_{\mathrm{tr}}(\boldsymbol{\phi};\boldsymbol{s}_{\mathrm{tr}},\boldsymbol{s}_{\mathrm{rad}}) + \gamma_{\mathrm{re}}(\boldsymbol{\phi};\boldsymbol{s}_{\mathrm{re}},\boldsymbol{s}_{\mathrm{rad}})$$
$$= \text{Two way field response}$$

$$\boldsymbol{h}(\boldsymbol{c},\nu) = \left[c(0); c(1)\mathrm{e}^{\text{ß}2\pi T\nu}; \cdots; c(P-1)\mathrm{e}^{\text{ß}2\pi\nu T(P-1)}\right]$$
$$= \text{Doppler-shifted code sequence}$$

The resulting signal redirected by the STAR-RIS toward direction $\phi \in \mathcal{F}$ is given by:

$$\varrho_{\text{RIS}}(t,\phi) = \varrho_{\text{tr}}(t,\phi) + \varrho_{\text{re}}(t,\phi), \tag{4.4}$$

for $t \in [0, PT)$, where

$$\varrho_{\text{tr}}(t,\phi) = \mathbb{1}_{\{\phi\in\mathcal{F}_{\text{tr}}\}}\sqrt{\mathcal{E}G_{\text{ris}}(\phi)}\left(\boldsymbol{u}_{\text{ris}}^{\mathsf{T}}(\phi)\text{diag}\{\boldsymbol{s}_{\text{tr}}\}\boldsymbol{g}\right)\sum_{p=0}^{P-1} c_{\text{tr}}(p)\psi(t-pT), \tag{4.5a}$$

$$\varrho_{\text{re}}(t,\phi) = \mathbb{1}_{\{\phi\in\mathcal{F}_{\text{re}}\}}\sqrt{\mathcal{E}G_{\text{ris}}(\phi)}\left(\boldsymbol{u}_{\text{ris}}^{\mathsf{T}}(\phi)\text{diag}\{\boldsymbol{s}_{\text{re}}\}\boldsymbol{g}\right)\sum_{p=0}^{P-1} c_{\text{re}}(p)\psi(t-pT). \tag{4.5b}$$

Note that, by definition of the angular domains $\mathcal{F}_{\text{tr}}$ and $\mathcal{F}_{\text{re}}$, a given direction $\phi \in \mathcal{F}$ belongs to at most one of the two half-spaces. Hence, in practice, for any given direction ϕ, only one of the two terms on the right-hand side of (4.4) is nonzero. This is enforced by the indicator functions in the expressions for $\varrho_{\text{tr}}(t,\phi)$ and $\varrho_{\text{re}}(t,\phi)$.

The space-time STAR-RIS response is under the designer's control; in particular, by inspecting (4.4), the following remarks are in order.

Remark 7. The terms $G_{\text{ris}}(\phi)\left|\boldsymbol{u}_{\text{ris}}^{\mathsf{T}}(\phi)\text{diag}\{\boldsymbol{s}_{\text{tr}}\}\boldsymbol{g}\right|^2$ and $G_{\text{ris}}(\phi)\left|\boldsymbol{u}_{\text{ris}}^{\mathsf{T}}(\phi)\text{diag}\{\boldsymbol{s}_{\text{re}}\}\boldsymbol{g}\right|^2$ specify the intensity of the electromagnetic signals redirected by the STAR-RIS towards $\phi \in \mathcal{F}_{\text{tr}}$ and $\phi \in \mathcal{F}_{\text{re}}$, respectively. In particular, we define the STAR-RIS array power pattern as

$$\text{A}_{\text{ris}}(\phi;\boldsymbol{s}_{\text{tr}},\boldsymbol{s}_{\text{re}}) = \text{A}_{\text{tr}}(\phi;\boldsymbol{s}_{\text{tr}}) + \text{A}_{\text{re}}(\phi;\boldsymbol{s}_{\text{re}}), \tag{4.6}$$

for $\phi \in \mathcal{F}$, where

$$\mathrm{A}_{\mathrm{tr}}(\phi; \boldsymbol{s}_{\mathrm{tr}}) = \frac{\left|\boldsymbol{u}_{\mathrm{ris}}^{\mathsf{T}}(\phi)\mathrm{diag}\{\boldsymbol{s}_{\mathrm{tr}}\}\boldsymbol{g}\right|^2}{\|\boldsymbol{g}\|_1^2}\mathbb{1}_{\{\phi\in\mathcal{F}_{\mathrm{tr}}\}} \tag{4.7a}$$

$$\mathrm{A}_{\mathrm{re}}(\phi; \boldsymbol{s}_{\mathrm{re}}) = \frac{\left|\boldsymbol{u}_{\mathrm{ris}}^{\mathsf{T}}(\phi)\mathrm{diag}\{\boldsymbol{s}_{\mathrm{re}}\}\boldsymbol{g}\right|^2}{\|\boldsymbol{g}\|_1^2}\mathbb{1}_{\{\phi\in\mathcal{F}_{\mathrm{re}}\}} \tag{4.7b}$$

are the STAR-RIS array power patterns in the transmissive and reflective half-spaces, respectively. In (4.6), we have made explicit the dependence upon $\boldsymbol{s}_{\mathrm{tr}}$ and $\boldsymbol{s}_{\mathrm{re}}$; these beamformers will be designed in Sec. 4.3.1 to redirect the incident signal towards some desired directions. Also, the adopted normalization ensures that $\mathrm{A}_{\mathrm{ris}}(\phi; \boldsymbol{s}_{\mathrm{tr}}, \boldsymbol{s}_{\mathrm{re}}) \leq 1\ \forall \phi \in \mathcal{F}$.

Remark 8. The P-dimensional code sequences

$$\boldsymbol{c}_{\mathrm{tr}} = [c_{\mathrm{tr}}(0); \cdots; c_{\mathrm{tr}}(P-1)] \tag{4.8a}$$

$$\boldsymbol{c}_{\mathrm{re}} = [c_{\mathrm{re}}(0); \cdots; c_{\mathrm{re}}(P-1)] \tag{4.8b}$$

superimpose a time modulation on the pulses redirected in the transmissive and reflective half-spaces, respectively; these code sequences will be designed in Sec. 4.3.2 to enable the sensing and communication functions.

4.2.2 Radar received signal

Denote by $\boldsymbol{s}_{\mathrm{rad}}$ the N_{rad}–dimensional analog beamformer with unit modulus entries employed by the radar receiver. This beamformer is under the designer's control and determines the PESA array power pattern, defined as

$$\mathrm{A}_{\mathrm{rad}}(\phi; \boldsymbol{s}_{\mathrm{rad}}) = \frac{\left|\boldsymbol{s}_{\mathrm{rad}}^{\mathsf{H}}\boldsymbol{u}_{\mathrm{rad}}(\phi)\right|^2}{N_{\mathrm{rad}}^2}, \tag{4.9}$$

for $\phi \in \mathcal{F}$ (more on this in Sec. 4.3). The adopted normalization ensures that $\mathrm{A}_{\mathrm{rad}}(\phi; \boldsymbol{s}_{\mathrm{rad}}) \leq 1\ \forall \phi \in \mathcal{F}$. Throughout the analysis, we assume that the individual PESA elements exhibit isotropic (omnidirectional) radiation

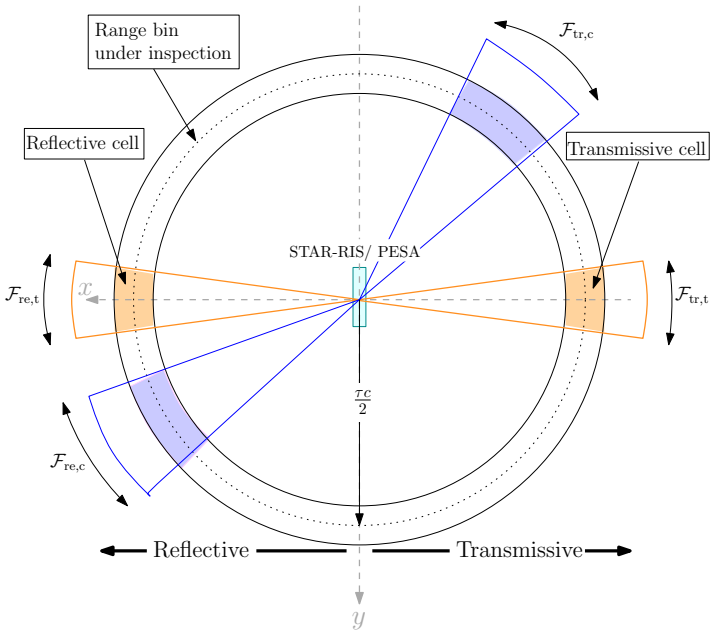

FIGURE 4.2: Illustration of the transmissive and reflective cells inspected by the radar receiver and of the clutter regions.

patterns. As such, angular selectivity arises exclusively from the beamforming action of the array.

From (4.2), it is seen that $\boldsymbol{u}_{\text{rad}}([\phi^{\text{az}};\phi^{\text{el}}]) = \boldsymbol{u}_{\text{rad}}([\pi-\phi^{\text{az}};\phi^{\text{el}}])$ for any $\phi^{\text{az}} \in (-\pi/2,\pi/2)$, which in turn implies $\text{A}_{\text{rad}}([\phi^{\text{az}};\phi^{\text{el}}];\boldsymbol{s}_{\text{rad}}) = \text{A}_{\text{rad}}([\pi-\phi^{\text{az}};\phi^{\text{el}}];\boldsymbol{s}_{\text{rad}})$. To reflect such symmetry, the angular regions monitored by the radar receiver in the transmissive and reflective half-spaces, say $\mathcal{F}_{\text{tr,t}} \subset \mathcal{F}_{\text{tr}}$ and $\mathcal{F}_{\text{re,t}} \subset \mathcal{F}_{\text{re}}$, respectively, are chosen mirror symmetric with respect to the plane containing both the STAR-RIS and the radar receiving array, as shown in Fig. 4.2; more specifically, we assume that

$$\mathcal{F}_{\text{tr,t}} = \left[\varphi^{\text{az}}_{\text{tr,t}}-\Delta^{\text{az}}_{\text{t}},\varphi^{\text{az}}_{\text{tr,t}}+\Delta^{\text{az}}_{\text{t}}\right]\times\left[\varphi^{\text{el}}_{\text{tr,t}}-\Delta^{\text{el}}_{\text{t}},\varphi^{\text{el}}_{\text{tr,t}}+\Delta^{\text{el}}_{\text{t}}\right], \tag{4.10a}$$

$$\mathcal{F}_{\text{re,t}} = \left[\varphi^{\text{az}}_{\text{re,t}}-\Delta^{\text{az}}_{\text{t}},\varphi^{\text{az}}_{\text{re,t}}+\Delta^{\text{az}}_{\text{t}}\right]\times\left[\varphi^{\text{el}}_{\text{re,t}}-\Delta^{\text{el}}_{\text{t}},\varphi^{\text{el}}_{\text{re,t}}+\Delta^{\text{el}}_{\text{t}}\right], \tag{4.10b}$$

respectively, with $\varphi^{\mathrm{az}}_{\mathrm{re,t}} = \pi - \varphi^{\mathrm{az}}_{\mathrm{tr,t}}$ and $\varphi^{\mathrm{el}}_{\mathrm{re,t}} = \varphi^{\mathrm{el}}_{\mathrm{tr,t}}$; here, $\boldsymbol{\varphi}_{\mathrm{tr,t}} = [\varphi^{\mathrm{az}}_{\mathrm{tr,t}}; \varphi^{\mathrm{el}}_{\mathrm{tr,t}}]$ and $\boldsymbol{\varphi}_{\mathrm{re,t}} = [\varphi^{\mathrm{az}}_{\mathrm{re,t}}; \varphi^{\mathrm{el}}_{\mathrm{re,t}}]$ are the central directions, while $\Delta^{\mathrm{az}}_{\mathrm{t}}$ and $\Delta^{\mathrm{el}}_{\mathrm{t}}$ specify the size of these regions. For future reference, we also define $\mathcal{F}_{\mathrm{t}} = \mathcal{F}_{\mathrm{tr,t}} \cup \mathcal{F}_{\mathrm{re,t}}$.

Next, denote by $\boldsymbol{b}_{\mathrm{rad}}(t) \in \mathbb{C}^{N_{\mathrm{rad}}}$ the baseband continuous-time signal collected by the antennas of the radar receiver in the considered CPI and by τ the delay of the inspected range bin. After analog beamforming, pulse compression, and range gating, the following samples are obtained

$$y_{\mathrm{rad}}(p) = \frac{1}{\sqrt{N_{\mathrm{rad}}}} \int_{\mathbb{R}} \boldsymbol{s}^{\mathsf{H}}_{\mathrm{rad}} \boldsymbol{b}_{\mathrm{rad}}(t) \psi^*\big(t - pT - \tau\big) dt, \tag{4.11}$$

for $p = 0, \ldots, P-1$. The pairs $(\boldsymbol{\varphi}_{\mathrm{tr,t}}, \tau)$ and $(\boldsymbol{\varphi}_{\mathrm{re,t}}, \tau)$ specify the resolution cells under inspection, as depicted in Fig. 4.2: we refer to them as the transmissive and reflective cells, respectively. For any $\boldsymbol{\phi} \in \mathcal{F}$, define the two-way field response in the transmissive and reflective side as

$$\begin{aligned} \gamma_{\mathrm{tr}}(\boldsymbol{\phi}; \boldsymbol{s}_{\mathrm{tr}}, \boldsymbol{s}_{\mathrm{rad}}) &= \sqrt{\frac{\mathcal{E} G_{\mathrm{rad}}(\boldsymbol{\phi}) G_{\mathrm{ris}}(\boldsymbol{\phi}) \lambda^2}{4\pi N_{\mathrm{rad}}}} \big(\boldsymbol{s}^{\mathsf{H}}_{\mathrm{rad}} \boldsymbol{u}_{\mathrm{rad}}(\boldsymbol{\phi})\big) \\ &\quad \times \big(\boldsymbol{u}^{\mathsf{T}}_{\mathrm{ris}}(\boldsymbol{\phi}) \mathrm{diag}\{\boldsymbol{g}\} \boldsymbol{s}_{\mathrm{tr}}\big) \mathbb{1}_{\{\boldsymbol{\phi} \in \mathcal{F}_{\mathrm{tr}}\}}, \end{aligned} \tag{4.12a}$$

$$\begin{aligned} \gamma_{\mathrm{re}}(\boldsymbol{\phi}; \boldsymbol{s}_{\mathrm{re}}, \boldsymbol{s}_{\mathrm{rad}}) &= \sqrt{\frac{\mathcal{E} G_{\mathrm{rad}}(\boldsymbol{\phi}) G_{\mathrm{ris}}(\boldsymbol{\phi}) \lambda^2}{4\pi N_{\mathrm{rad}}}} \big(\boldsymbol{s}^{\mathsf{H}}_{\mathrm{rad}} \boldsymbol{u}_{\mathrm{rad}}(\boldsymbol{\phi})\big) \\ &\quad \times \big(\boldsymbol{u}^{\mathsf{T}}_{\mathrm{ris}}(\boldsymbol{\phi}) \mathrm{diag}\{\boldsymbol{g}\} \boldsymbol{s}_{\mathrm{re}}\big) \mathbb{1}_{\{\boldsymbol{\phi} \in \mathcal{F}_{\mathrm{re}}\}}. \end{aligned} \tag{4.12b}$$

respectively, which account for overall propagation effects, except for the target response and the temporal modulation induced by the STAR-RIS. Upon assuming that at most one target is present in each resolution cell,

$y_{\text{rad}}(p)$ can be expanded as

$$\begin{aligned} y_{\text{rad}}(p) &= \alpha_{\text{tr,t}}\gamma_{\text{tr}}(\boldsymbol{\phi}_{\text{tr,t}}; \boldsymbol{s}_{\text{tr}}, \boldsymbol{s}_{\text{rad}})c_{\text{tr}}(p)\mathrm{e}^{\mathrm{i}2\pi\nu_{\text{tr,t}}T(p-1)} \\ &\quad + \alpha_{\text{re,t}}\gamma_{\text{re}}(\boldsymbol{\phi}_{\text{re,t}}; \boldsymbol{s}_{\text{re}}, \boldsymbol{s}_{\text{rad}})c_{\text{re}}(p)\mathrm{e}^{\mathrm{i}2\pi\nu_{\text{re,t}}T(p-1)} \\ &\quad + z_{\text{rad}}(p), \end{aligned} \tag{4.13}$$

where: $\alpha_{\text{tr,t}} \in \mathbb{C}$, $\nu_{\text{tr,t}} \in \mathbb{R}$, and $\boldsymbol{\phi}_{\text{tr,t}} \in \mathcal{F}_{\text{tr,t}}$ are the unknown amplitude, Doppler shift, and angular direction of a prospective target in the transmissive cell, respectively; $\alpha_{\text{re,t}} \in \mathbb{C}$, $\nu_{\text{re,t}} \in \mathbb{R}$, and $\boldsymbol{\phi}_{\text{re,t}} \in \mathcal{F}_{\text{re,t}}$ are the unknown amplitude, Doppler shift, and angular direction of a prospective target in the reflective cell, respectively; $z_{\text{rad}}(p)$ is the additive disturbance, including both clutter and noise. Here, $\alpha_{\text{tr,t}}$ and $\alpha_{\text{re,t}}$ account for the two-way path-loss from the STAR-RIS to the target and the target RCS , with $\alpha_{\text{tr,t}} = 0$ and $\alpha_{\text{re,t}} = 0$ if no target is present in the transmissive and reflective cells, respectively.

The observations in (4.13) are collected into the vector $\boldsymbol{y}_{\text{rad}} = \left[y_{\text{rad}}(0); \cdots; y_{\text{rad}}(P-1)\right] \in \mathbb{C}^P$. For any code sequence $\boldsymbol{c} = [c(0); \cdots; c(P-1)] \in \mathbb{C}^P$ and Doppler shift $\nu \in \mathbb{R}$, denote by

$$\boldsymbol{h}(\boldsymbol{c}, \nu) = \left[c(0); c(1)\mathrm{e}^{\mathrm{i}2\pi T\nu}; \cdots; c(P-1)\mathrm{e}^{\mathrm{i}2\pi\nu T(P-1)}\right]. \tag{4.14}$$

Then, we have

$$\begin{aligned} \boldsymbol{y}_{\text{rad}} &= \alpha_{\text{tr,t}}\gamma_{\text{tr}}(\boldsymbol{\phi}_{\text{tr,t}}; \boldsymbol{s}_{\text{tr}}, \boldsymbol{s}_{\text{rad}})\boldsymbol{h}(\boldsymbol{c}_{\text{tr}}, \nu_{\text{tr,t}}) \\ &\quad + \alpha_{\text{re,t}}\gamma_{\text{re}}(\boldsymbol{\phi}_{\text{re,t}}; \boldsymbol{s}_{\text{re}}, \boldsymbol{s}_{\text{rad}})\boldsymbol{h}(\boldsymbol{c}_{\text{re}}, \nu_{\text{re,t}}) + \boldsymbol{z}_{\text{rad}}, \end{aligned} \tag{4.15}$$

where $\boldsymbol{z}_{\text{rad}} = \left[z_{\text{rad}}(0); \cdots; z_{\text{rad}}(P-1)\right] \in \mathbb{C}^P$.

Two-way array power pattern

For $\phi \in \mathcal{F}$, the quantity

$$\gamma(\phi; \boldsymbol{s}_{\text{tr}}, \boldsymbol{s}_{\text{re}}, \boldsymbol{s}_{\text{rad}}) = \gamma_{\text{tr}}(\phi; \boldsymbol{s}_{\text{tr}}, \boldsymbol{s}_{\text{rad}}) + \gamma_{\text{re}}(\phi; \boldsymbol{s}_{\text{re}}, \boldsymbol{s}_{\text{rad}}) \tag{4.16}$$

depends on the two-way spatial response of the radar; in particular, we have

$$|\gamma(\phi; \boldsymbol{s}_{\text{tr}}, \boldsymbol{s}_{\text{re}}, \boldsymbol{s}_{\text{rad}})|^2 = \frac{\mathcal{E} G_{\text{rad}}(\phi) G_{\text{ris}}(\phi) \lambda^2}{4\pi} N_{\text{rad}} \|\boldsymbol{g}\|_1^2 \text{A}(\phi; \boldsymbol{s}_{\text{tr}}, \boldsymbol{s}_{\text{re}}, \boldsymbol{s}_{\text{rad}}), \tag{4.17}$$

where

$$\text{A}(\phi; \boldsymbol{s}_{\text{tr}}, \boldsymbol{s}_{\text{re}}, \boldsymbol{s}_{\text{rad}}) = \text{A}_{\text{rad}}(\phi; \boldsymbol{s}_{\text{rad}}) \text{A}_{\text{ris}}(\phi; \boldsymbol{s}_{\text{tr}}, \boldsymbol{s}_{\text{re}}) \tag{4.18}$$

is the two-way array power pattern towards $\phi \in \mathcal{F}$. Notice that $\text{A}(\phi; \boldsymbol{s}_{\text{tr}}, \boldsymbol{s}_{\text{re}}, \boldsymbol{s}_{\text{rad}}) \leq 1 \; \forall \phi \in \mathcal{F}$.

Disturbance model

Assume that $K_{\text{tr,c}}$ and $K_{\text{re,c}}$ clutter components are present in the transmissive and reflective half-spaces, respectively; then, $\boldsymbol{z}_{\text{rad}}$ can be expanded as

$$\begin{aligned} \boldsymbol{z}_{\text{rad}} = \boldsymbol{w}_{\text{rad}} &+ \sum_{k=1}^{K_{\text{tr,c}}} \alpha_{\text{tr,c},k} \gamma_{\text{tr}}(\phi_{\text{tr,c},k}, \boldsymbol{s}_{\text{tr}}, \boldsymbol{s}_{\text{rad}}) \boldsymbol{h}(\boldsymbol{c}_{\text{tr}}, \nu_{\text{tr,c},k}) \\ &+ \sum_{k=1}^{K_{\text{re,c}}} \alpha_{\text{re,c},k} \gamma_{\text{re}}(\phi_{\text{re,c},k}, \boldsymbol{s}_{\text{re}}, \boldsymbol{s}_{\text{rad}}) \boldsymbol{h}(\boldsymbol{c}_{\text{re}}, \nu_{\text{re,c},k}), \end{aligned} \tag{4.19}$$

where: $\boldsymbol{w}_{\text{rad}}$ is a circularly-symmetric Gaussian random vector with covariance matrix $\sigma_{\text{rad}}^2 \boldsymbol{I}_P$ accounting for the additive noise; $\alpha_{\text{tr,c},k} \in \mathbb{C}$, $\nu_{\text{tr,c},k} \in \mathbb{R}$, and $\phi_{\text{tr,c},k} \in \mathcal{F}_{\text{tr,c}}$ are the complex amplitude, Doppler shift, and angular direction of the k-th clutter component in the transmissive half-space, respectively; $\alpha_{\text{re,c},k} \in \mathbb{C}$, $\nu_{\text{re,c},k} \in \mathbb{R}$, and $\phi_{\text{re,c},k} \in \mathcal{F}_{\text{re,c}}$ are the complex

amplitude, Doppler shift, and angular direction of the k-th clutter component in the reflective half-space, respectively. Here, $\mathcal{F}_{\text{tr,c}} \subset \mathcal{F}_{\text{tr}} \setminus \mathcal{F}_{\text{tr,t}}$ and $\mathcal{F}_{\text{re,c}} \subset \mathcal{F}_{\text{re}} \setminus \mathcal{F}_{\text{re,t}}$ are the angular regions containing the clutter components in the transmissive and reflective half-spaces, respectively, as depicted in Fig. 4.2; for future reference, we also define $\mathcal{F}_{\text{c}} = \mathcal{F}_{\text{tr,c}} \cup \mathcal{F}_{\text{re,c}}$. Finally, we model $\alpha_{\text{tr,c},k}$ and $\alpha_{\text{re,c},k}$ as independent circularly-symmetric Gaussian random variables with variance $\sigma^2_{\text{tr,c},k}$ and $\sigma^2_{\text{re,c},k}$, respectively; accordingly, the disturbance covariance matrix is

$$\begin{aligned}\boldsymbol{C}_{\text{rad}} = \sigma^2_{\text{rad}}\boldsymbol{I} &+ \sum_{k=1}^{K_{\text{tr,c}}} \sigma^2_{\text{tr,c},k} |\gamma_{\text{tr}}(\boldsymbol{\phi}_{\text{tr,c},k}, \boldsymbol{s}_{\text{tr}}, \boldsymbol{s}_{\text{rad}})|^2 \boldsymbol{h}(\boldsymbol{c}_{\text{tr}}, \nu_{\text{tr,c},k}) \boldsymbol{h}^{\mathsf{H}}(\boldsymbol{c}_{\text{tr}}, \nu_{\text{tr,c},k}) \\ &+ \sum_{k=1}^{K_{\text{re,c}}} \sigma^2_{\text{re,c},k} |\gamma_{\text{re}}(\boldsymbol{\phi}_{\text{re,c},k}, \boldsymbol{s}_{\text{re}}, \boldsymbol{s}_{\text{rad}})|^2 \boldsymbol{h}(\boldsymbol{c}_{\text{re}}, \nu_{\text{re,c},k}) \boldsymbol{h}^{\mathsf{H}}(\boldsymbol{c}_{\text{re}}, \nu_{\text{re,c},k}).\end{aligned} \tag{4.20}$$

4.2.3 User received signal

When the communication function is present, the STAR-RIS partitions the CPI into P/M time slots of equal duration, where M is chosen so that P/M is an integer and MT is smaller than the coherence time of the channel from the STAR-RIS to the user. In every time slot, the STAR-RIS sends two messages (one for each side) as discussed in Sec. 4.3.

For illustration, consider the time slot $[0, MT]$ and the transmissive half-space. The signal received by the user is

$$y_{\text{tr,u}}(t) = \sum_{k=1}^{K_{\text{tr,u}}} \alpha_{\text{tr,u},k} \varrho_{\text{tr}}(t - \tau_{\text{tr,u},k}, \boldsymbol{\phi}_{\text{tr,u},k}) + z_{\text{tr,u}}(t), \tag{4.21}$$

for $t \in [0, MT]$, where: $K_{\text{tr,u}} \geq 1$ is the number of channel paths from the STAR-RIS to the user; $\alpha_{\text{tr,u},k} \in \mathbb{C}$ is the amplitude of the k-th path; $\tau_{\text{tr,u},k} \in [\tau_{\text{tr,u,min}}, \tau_{\text{tr,u,max}}]$ is the delay of the k-th path, with $0 \leq \tau_{\text{tr,u,min}} \leq \tau_{\text{tr,u,max}} \leq T - 2\Delta$; $\boldsymbol{\phi}_{\text{tr,u},k} \in \mathcal{F}_{\text{tr,u}}$ is the angular direction of departure of the

k-th path, with $\mathcal{F}_{\text{tr,u}} \subset \mathcal{F}_{\text{tr}}$; finally, $z_{\text{tr,u}}(t)$ is the additive noise. The quantities $K_{\text{tr,u}}$ and $\{\alpha_{\text{tr,u},k},\, \tau_{\text{tr,u},k},\, \phi_{\text{tr,u},k}\}_{k=1}^{K_{\text{tr,u}}}$ are unknown, as no instantaneous CSI is available. We only make the mild assumptions that the STAR-RIS knows the set $\mathcal{F}_{\text{tr,u}}$ and that the user knows the interval $[\tau_{\text{tr,u,min}}, \tau_{\text{tr,u,max}}]$; indeed, these quantities are tied to some prior information on the user location and can be enlarged at the design stage to account for greater uncertainty.

The signal in (4.21) is passed through a unit-energy filter matched to $\psi(t)$ and sampled at the Nyquist rate $1/B$. Upon denoting by $r_\psi(t) = \psi(t) * \psi^*(-t)$ the autocorrelation function of $\psi(t)$, the output samples are

$$\begin{aligned} y_{\text{tr},u}(p,\ell) &= y_{\text{tr,u}}(t) * \psi^*(-t) \mid_{t=\tau_{\text{tr,u,min}}+pT+\ell/B} \\ &= c_{\text{tr}}(p)\beta_{\text{tr},u}(\ell) + z_{\text{tr},u}(\ell,p), \end{aligned} \tag{4.22}$$

for $p = 0,\dots,M-1$ and $\ell = 0,\dots,L_{\text{tr},u}-1$, where $L_{\text{tr},u} = \lceil (\tau_{\text{tr,u,max}} - \tau_{\text{tr,u,min}} + 2\Delta)B \rceil$ and

$$\begin{aligned} \beta_{\text{tr},u}(\ell) = \sum_{k=1}^{K_{\text{tr,u}}} \alpha_{\text{tr,u},k} \sqrt{\mathcal{E} G_{\text{ris}}(\boldsymbol{\phi}_{\text{tr,u},k})}\, r_\psi\big(\tau_{\text{tr,u,min}} + \ell/B - \tau_{\text{tr,u},k}\big) \\ \times \big(\boldsymbol{u}_{\text{ris}}^{\mathsf{T}}(\boldsymbol{\phi}_{\text{tr,u},k}) \text{diag}\{\boldsymbol{g}\} \boldsymbol{s}_{\text{tr}}\big), \end{aligned} \tag{4.23a}$$

$$z_{\text{tr},u}(p,\ell) = z_{\text{tr,u}}(t) * \psi^*(-t) \mid_{t=\tau_{\text{tr,u,min}}+pT+\ell/B}. \tag{4.23b}$$

The coefficients $\{\beta_{\text{tr},u}(\ell)\}_{\ell=0}^{L_{\text{tr},u}-1}$ are the tap amplitudes of the discrete-time channel from the feeder to the STAR-RIS to the user. Since $r_\psi(t) = 0$ if $|t| \geq \Delta$, the k-th channel path contributes to the ℓ-th channel tap in (4.23a) only if $|\tau_{\text{tr,u,min}} + \ell/B - \tau_{\text{tr,u},k}| < \Delta$, with a strength that depends on the spatial response of the STAR-RIS towards $\boldsymbol{\phi}_{\text{tr,u},k}$. Finally, we model the noise samples $\{z_{\text{tr},u}(\ell,p),\ \ell = 0,\dots,L_{\text{tr},u}-1,\ p = 0,\dots,M-1\}$ are i.i.d. circularly-symmetric Gaussian random variables with variance σ^2_{com}.

For the reflective side, the signal received by the user is similarly derived: it is sufficient to replace the subscript "tr" with "re" in the above derivations from (4.21) to (4.23). For example, $K_{\text{re,u}} \geq 1$ denotes the number of channel paths for the user in the reflective side, with the corresponding angles of departure belonging to the set $\mathcal{F}_{\text{re,u}} \subset \mathcal{F}_{\text{re}}$. For future reference, we also define $\mathcal{F}_{\text{u}} = \mathcal{F}_{\text{tr,u}} \cup \mathcal{F}_{\text{re,u}}$.

4.3 System design

The space-time response of the STAR-RIS, the analog beamformer of the radar receiver, and the implementation of the radar and communication receivers are under the control of the system engineer. In Sec. 4.3.1, leveraging the knowledge of the channel $\boldsymbol{g}$ between the feeder and the STAR-RIS, we design the space response of the STAR-RIS and the analog beamformer of the radar receiver (namely, $\boldsymbol{s}_{\text{tr}}$, $\boldsymbol{s}_{\text{re}}$, and $\boldsymbol{s}_{\text{rad}}$) to control the STAR-RIS array power pattern, the PESA array power pattern, and their product.

In Sec. 4.3.2, instead, we design the temporal response of the STAR-RIS (namely, $\boldsymbol{c}_{\text{tr}}$ and $\boldsymbol{c}_{\text{re}}$) to make the echoes received from the two half-spaces distinguishable by the radar receiver, while also conveying a message to the users in the absence of instantaneous CSI. Finally, in Secs. 4.3.3, we discuss the implementation of the radar, which faces the challenge of a composite multiple hypotheses testing problem, and, in Sec. 4.3.4, we design the communication receivers, which must to recover the encoded message in the absence of instantaneous CSI.

4.3.1 Design of s_{tr}, s_{re}, and s_{rad}

Let $\bar{\mathcal{F}}_t$, $\bar{\mathcal{F}}_c$, and $\bar{\mathcal{F}}_u$ be the discrete sets containing a grid of angular directions taken from $\mathcal{F}_t$, $\mathcal{F}_c$, and $\mathcal{F}_u$, respectively. The region $\mathcal{F}_t$ typically corresponds to areas of operational interest identified through environmental maps, prior knowledge of target trajectories, or site surveys, which implies the availability of preliminary information. This prior information allows radar designers to guide beamforming efforts toward the most likely target directions, optimizing energy allocation. In other scenarios, such as search-mode operation, the radar may sequentially scan multiple angular directions, and $\mathcal{F}_t$ may accordingly cover a broader range. We remark that, although the sets $\mathcal{F}_t$ and $\mathcal{F}_u$ are defined independently, some level of spatial overlap between them may be desirable in order to ease the design of STAR-RIS beampatterns that simultaneously support both radar target illumination and user communication. In practice, partial angular alignment between targets and users may arise naturally due to deployment geometry. However, the proposed design framework remains valid even when these angular regions are disjoint. We consider the following design criterion

$$\max_{\boldsymbol{s}_{\text{tr}},\boldsymbol{s}_{\text{re}},\boldsymbol{s}_{\text{rad}}} \sum_{\boldsymbol{\phi}\in\bar{\mathcal{F}}_{\text{t}}} \mathrm{A}(\boldsymbol{\phi};\boldsymbol{s}_{\text{tr}},\boldsymbol{s}_{\text{re}},\boldsymbol{s}_{\text{rad}}), \tag{4.24a}$$

$$\text{s.t. } \mathrm{A}(\boldsymbol{\phi};\boldsymbol{s}_{\text{tr}},\boldsymbol{s}_{\text{re}},\boldsymbol{s}_{\text{rad}}) \le \zeta_c, \quad \forall \boldsymbol{\phi}\in\bar{\mathcal{F}}_{\text{c}}, \tag{4.24b}$$

$$\mathrm{A}_{\text{ris}}(\boldsymbol{\phi};\boldsymbol{s}_{\text{tr}},\boldsymbol{s}_{\text{re}}) \ge \zeta_u, \quad \forall \boldsymbol{\phi}\in\bar{\mathcal{F}}_{\text{u}}, \tag{4.24c}$$

$$|s_{\text{tr},n}| = |s_{\text{re},n}| = 1, \quad n = 1,\dots,N_{\text{ris}}, \tag{4.24d}$$

$$|s_{\text{rad},n}| = 1, \quad n = 1,\dots,N_{\text{rad}}, \tag{4.24e}$$

where $\zeta_c \in [0,1]$ and $\zeta_u \in [0,1]$ are design parameters. The feasibility of Problem (4.24) inherently depends on the choice of the thresholds ζ_c and

ζ_u. In practice, these values may need to be carefully adjusted to avoid conflicting constraints and to ensure that the optimization problem admits at least one solution. If the thresholds are too strict (e.g., large ζ_u and small ζ_c), no feasible beamformer may exist, and a relaxation of the design criteria may be necessary. Problem (4.24) aims to obtain a large two-way array power pattern in the angular regions monitored by radar, while limiting the two-way array power pattern in the angular regions containing clutter (first constraint) and requiring a minimum value of the STAR-RIS array power pattern in the angular regions where the users are located (second constraint). The last two constraints ensure that the spatial beamformers of the STAR-RIS and the analog beamformer of the radar receiver have unit modulus entries (see Secs. 4.2.1 and 4.2.2, respectively). Only the knowledge of $\boldsymbol{g}$, $\mathcal{F}_{\mathrm{c}}$, and $\mathcal{F}_{\mathrm{u}}$ is required for this design criterion.

Since Problem (4.24) is non-convex, we derive a suboptimal solution by using to the augmented Lagrangian method with partial elimination of the constraints [105], [106]; the associated computations are provided in Appendix A.As with many non-convex optimization problems, the solution obtained using the augmented Lagrangian method is sensitive to the initialization of the beamforming vectors. A good initialization (e.g., based on maximum-gain heuristics or previously optimized patterns) can lead to better convergence behavior and higher-quality solutions. In contrast, poor initialization may result in local optima with degraded radar or communication performance. Therefore, warm-start strategies or multiple initializations can be considered in practice. Finally note that, for a given region of interest $\mathcal{F}_{\mathrm{t}}$, the space response of the STAR-RIS must be updated every time the radar transmitter to STAR-RIS channel $\boldsymbol{g}$, the set containing the angles of departure for the user channel path $\mathcal{F}_{\mathrm{u}}$, or the angular region containing

the clutter components $\mathcal{F}_c$ changes. This happens over a long time scale (at least P PRIs, the radar coherent processing interval) and does not significantly impact real-time operation. Additionally, the size of the sets $\mathcal{F}_u$ and $\mathcal{F}_c$ can be adjusted to meet the required complexity-performance tradeoff: smaller sets reduce the uncertainty and improve the system performance, but this requires more frequent updates of the STAR-RIS space response, which increases the computational burden.

4.3.2 Design of $\boldsymbol{c}_{\text{tr}}$ and $\boldsymbol{c}_{\text{re}}$

The temporal code sequences of the STAR-RIS must ensure that the echoes originated from different half-spaces can be distinguished [63]; therefore, $\boldsymbol{c}_{\text{tr}}$ and $\boldsymbol{c}_{\text{re}}$ should have a low cross-correlation and be Doppler tolerant. Also, any embedded message must be encoded by the STAR-RIS and decoded by the communication receiver in the absence of instantaneous CSI. Inspired by the frame-by-frame encoding rule in [107], we propose two encoding strategies, which result into a simultaneous or sequential illumination of the two half-spaces over a CPI. To proceed, assume that $P \geq 4$ is a power of 2 and that P/M is integer; accordingly, M is also a power of 2.

Simultaneous illumination

The STAR-RIS operates here in the ES mode [69] and simultaneously illuminates both half-spaces in each PRI, i.e., $c_{\text{tr}}(p), c_{\text{re}}(p) \neq 0$ for $p = 0, \ldots, P-1$.

When the communication function is active, $\boldsymbol{c}_{\text{tr}}$ and $\boldsymbol{c}_{\text{re}}$ are constructed as the concatenation of P/M codewords taken from distinct codebooks $\mathcal{C}_{\text{tr}}$ and $\mathcal{C}_{\text{re}}$, respectively, so that $[\boldsymbol{c}_{\text{tr}}]_{(m-1)M+1:mM} \in \mathcal{C}_{\text{tr}}$ and $[\boldsymbol{c}_{\text{re}}]_{(m-1)M+1:mM} \in \mathcal{C}_{\text{re}}$, for $m = 1, \ldots, P/M$. Let $b \geq 1$ be the number of bits sent per time slot in each half-space also, let M be a power of two with $2^{b+1} \leq M \leq P$; finally, let $\boldsymbol{H}_M \in \{-1, 1\}^{M \times M}$ be the Hadamard of order M. Then, we propose to

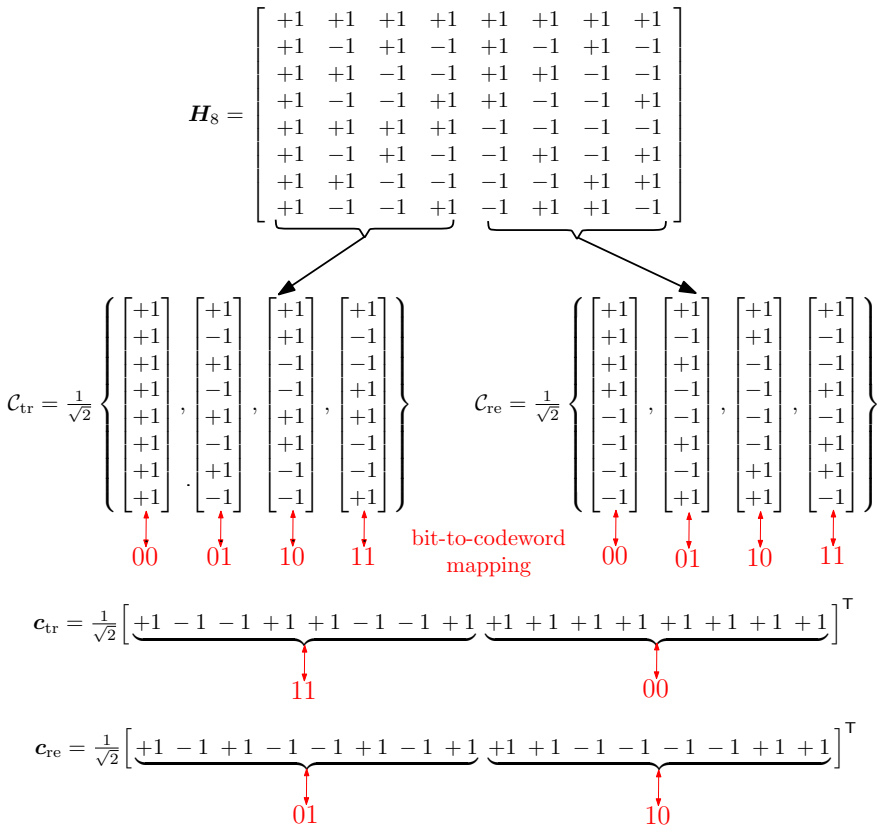

FIGURE 4.3: Encoding rule for simultaneous illumination when $P = 16$, $M = 8$, $b = 2$, and the bits 1100 and 0110 are sent in the transmissive and reflective half-spaces, respectively.

use the following codebooks

$$\mathcal{C}_{\text{tr}} = \left\{\text{first } 2^b \text{ columns of } 1/\sqrt{2}\boldsymbol{H}_M\right\}, \tag{4.25a}$$

$$\mathcal{C}_{\text{re}} = \left\{\text{last } 2^b \text{ columns of } 1/\sqrt{2}\boldsymbol{H}_M\right\}, \tag{4.25b}$$

where the factor $1/\sqrt{2}$ ensures that half of the energy is redirected in each half-space in every PRI. The transmission rate in each half-space is here $\mathcal{R} = \frac{b}{M}$ [bit per pulse]. Fig. 4.3 provides an illustration of this encoding rule, while Table 4.3 provides the possible values of M, b, and $\mathcal{R}$ when $P = 16$.

TABLE 4.3: Proposed encoding rules when $P = 16$

M			
Simultaneous	Sequential	b	$\mathcal{R}$ [bit per pulse]
16	8	1	1/16
8	4	1	2/16
16	8	2	2/16
16	8	3	3/16
4	2	1	4/16
8	4	2	4/16

When the communication function is not active, $\boldsymbol{c}_{\text{tr}}$ and $\boldsymbol{c}_{\text{re}}$ are chosen as the first and last columns of $\boldsymbol{H}_P$, respectively, which corresponds to set $M = P$ and $b = 0$ in (4.25).

Sequential illumination

The STAR-RIS operates here in the TS mode [69] and illuminates the transmissive half-space in the subinterval $[0, PT/2)$ and the reflective half-space in $[PT/2, PT)$, i.e., we have $[\boldsymbol{c}_{\text{tr}}]_{P/2+1:P} = [\boldsymbol{c}_{\text{re}}]_{1:P/2} = \boldsymbol{0}_{P/2}$.

When the communication function is active, $[\boldsymbol{c}_{\text{tr}}]_{1:P/2}$ and $[\boldsymbol{c}_{\text{re}}]_{P/2+1:P}$ are constructed as the concatenation of $P/(2M)$ codewords taken from a codebook $\mathcal{C}$, so that $[\boldsymbol{c}_{\text{tr}}]_{(m-1)M+1:mM} \in \mathcal{C}$ and $[\boldsymbol{c}_{\text{re}}]_{P/2+(m-1)M+1:P/2+mM} \in \mathcal{C}$, for $m = 1, \ldots, P/(2M)$. Let $b \geq 1$ be the number of bits to be sent per time slot (either on the transmissive or the reflecting half-space); also, let M be a power of two with $2^b \leq M \leq P/2$. Then we use the following codebook

$$\mathcal{C} = \left\{\text{first } 2^b \text{ columns of } \boldsymbol{H}_M\right\}. \tag{4.26}$$

There are several ways to construct a set of code sequences with good autocorrelation and cross-correlation properties. Zadoff–Chu sequences are one notable example, widely used in radar and communication systems

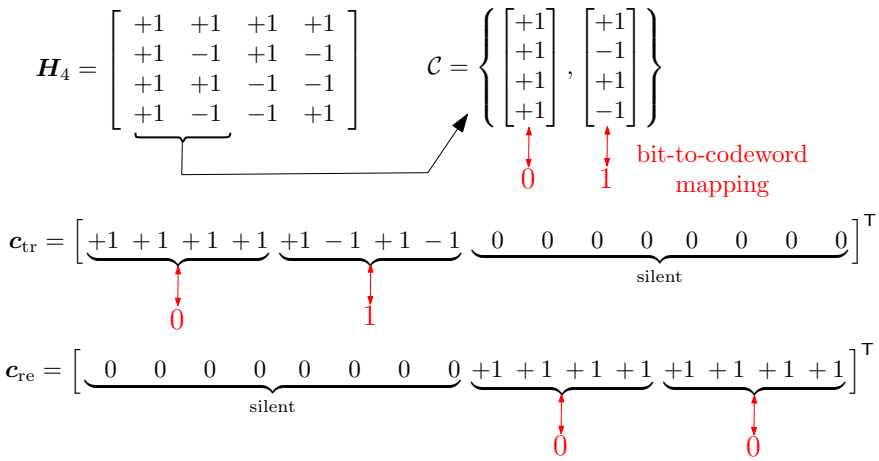

FIGURE 4.4: Encoding rule for sequential illumination when $P = 16$, $M = 4$, $b = 1$, and the bits 01 and 00 are sent in the transmissive and reflective half-spaces, respectively.

due to their constant modulus and ideal correlation profiles [108], [109]. Incorporating such sequences into the proposed framework is left for future investigation.

The transmission rate in each half-space is $\mathcal{R} = \frac{b}{2M}$ [bit per pulse], where the factor $1/2$ results from time splitting. Fig. 4.4 illustrates this encoding rule, while Table 4.3 reports the possible values of M, b, and $\mathcal{R}$ when $P = 16$.

When the communication function is not active, $[\boldsymbol{c}_{\text{tr}}]_{1:P/2}$ and $[\boldsymbol{c}_{\text{re}}]_{P/2+1:P}$ are both chosen as the first column of $\boldsymbol{H}_{P/2}$, which corresponds to set $M = P/2$ and $b = 0$ in (4.26).

Comments

Both encoding rules equally split the incident energy between the two half-spaces and, for a given P and b, can support the same transmission rate by arranging the value of M (see Table 4.3). In each time slot, the communication function relies on an orthogonal codebook to facilitate reliable

message recovery at the communication receiver, as discussed in more detail later. Moreover, the P-dimensional code sequences $\boldsymbol{c}_{\text{tr}}$ and $\boldsymbol{c}_{\text{re}}$ resulting from the concatenation of P/M codewords are orthogonal irrespectively of the encoded message, which aids in separating echoes originating from different half-spaces in (4.15). As to this latter point, a distinction arises between simultaneous and sequential illuminations, which has implications for the radar receiver design. In sequential illumination, echoes from different half-spaces are orthogonal regardless of their Doppler shifts. In contrast, under simultaneous illumination, such echoes lose orthogonality when they exhibit different Doppler shifts. Note that this encoding scheme can work even in rapidly changing environments; for example, MT, which must be smaller than the channel coherence time, can be set as low as two PRIs in simultaneous illumination. The coefficients $c_{\text{tr}}(p)$ and $c_{\text{re}}(p)$ are updated once per PRI T. Since T is much larger than the inverse of the signal bandwidth, these updates occur at a significantly lower rate compared to the baseband sampling rate, making this operation lightweight for the STAR-RIS controller. Finally, note that this encoding scheme is based on some idealistic assumptions. In particular, we are using here the phase-shift model, which, although widely adopted and convenient, is an oversimplified representation of the actual physical process [91]. Furthermore, we have adopted the common assumption that the phase shifts on the transmissive and reflective sides can be independently and continuously controlled. However, current hardware implementations can only support a finite set of reflection and transmission coefficients, and these coefficients are coupled [89], [91].

4.3.3 Design of the radar receiver

The radar detector relies on the knowledge of the code sequences $\boldsymbol{c}_{\text{tr}}$ and $\boldsymbol{c}_{\text{re}}$ to distinguish the echoes from different half-spaces. In particular, it is faced with a multiple composite hypotheses testing problem with four hypotheses:

$\mathcal{H}_0$**:** no target is present in the cells under inspection;

$\mathcal{H}_{1,\text{tr}}$**:** a target with unknown amplitude and Doppler shift is present only in the transmissive cell;

$\mathcal{H}_{1,\text{re}}$**:** a target with unknown amplitude and Doppler shift is present only in the reflective cell;

$\mathcal{H}_2$**:** a target with unknown amplitude and Doppler shift is present in each resolution cell under inspection.

Since this problem can be regarded as a model order selection, we propose to use a GIC-based decision rule [70]; hence, the selected hypothesis is

$$\hat{\mathcal{H}} = \underset{\mathcal{L}\in\{\mathcal{H}_0,\mathcal{H}_{1,\text{tr}},\mathcal{H}_{1,\text{re}},\mathcal{H}_2\}}{\arg\max}\ \mu(\mathcal{L}), \tag{4.27}$$

where

$$\mu(\mathcal{L}) = \begin{cases} f_{\mathcal{H}_0}(\boldsymbol{y}_{\text{rad}}), & \text{if } \mathcal{L}=\mathcal{H}_0, \\ \max\limits_{\substack{\alpha_{\text{tr,t}}\in\mathbb{C}\\ \nu_{\text{tr,t}}\in\mathcal{V}_{\text{tr,t}}}} f_{\mathcal{H}_{1,\text{tr}}}(\boldsymbol{y}_{\text{rad}};\alpha_{\text{tr,t}},\nu_{\text{tr,t}}) - \eta_{\text{rad}}, & \text{if } \mathcal{L}=\mathcal{H}_{1,\text{tr}}, \\ \max\limits_{\substack{\alpha_{\text{re,t}}\in\mathbb{C}\\ \nu_{\text{re,t}}\in\mathcal{V}_{\text{re,t}}}} f_{\mathcal{H}_{1,\text{re}}}(\boldsymbol{y}_{\text{rad}};\alpha_{\text{re,t}},\nu_{\text{re,t}}) - \eta_{\text{rad}}, & \text{if } \mathcal{L}=\mathcal{H}_{1,\text{re}}, \\ \max\limits_{\substack{\boldsymbol{\alpha}_{\text{t}}\in\mathbb{C}^2\\ \boldsymbol{\nu}_{\text{t}}\in\mathcal{V}_{\text{tr,t}}\times\mathcal{V}_{\text{re,t}}}} f_{\mathcal{H}_2}(\boldsymbol{y}_{\text{rad}};\boldsymbol{\alpha}_{\text{t}},\boldsymbol{\nu}_{\text{t}}) - 2\eta_{\text{rad}}, & \text{if } \mathcal{L}=\mathcal{H}_2, \end{cases} \tag{4.28}$$

$f_{\mathcal{L}}(\boldsymbol{y}_{\text{rad}};\cdot)$ is the log-likelihood function under $\mathcal{L}$, $\boldsymbol{\alpha}_{\text{t}} = [\alpha_{\text{tr,t}};\alpha_{\text{re,t}}]$, $\boldsymbol{\nu}_{\text{t}} = [\nu_{\text{tr,t}};\nu_{\text{re,t}}]$, $\mathcal{V}_{\text{tr,t}}$ and $\mathcal{V}_{\text{re,t}}$ are the Doppler search intervals in the transmissive and reflective half-space, respectively, and η_{rad} is a penalty factor that can be set to control the false alarm rate under $\mathcal{H}_0$.

To proceed, define the following quantities:

$$\boldsymbol{\xi}_{\text{tr}}(\nu_{\text{tr,t}}) = \boldsymbol{C}_{\text{rad}}^{-1}\boldsymbol{h}(\boldsymbol{c}_{\text{tr}},\nu_{\text{tr,t}})/\|\boldsymbol{C}_{\text{rad}}^{-\frac{1}{2}}\boldsymbol{h}(\boldsymbol{c}_{\text{tr}},\nu_{\text{tr,t}})\|, \tag{4.29a}$$

$$\boldsymbol{\xi}_{\text{re}}(\nu_{\text{re,t}}) = \boldsymbol{C}_{\text{rad}}^{-1}\boldsymbol{h}(\boldsymbol{c}_{\text{re}},\nu_{\text{re,t}})/\|\boldsymbol{C}_{\text{rad}}^{-\frac{1}{2}}\boldsymbol{h}(\boldsymbol{c}_{\text{re}},\nu_{\text{re,t}})\|, \tag{4.29b}$$

$$\begin{aligned}\boldsymbol{\Xi}(\boldsymbol{\nu}_{\text{t}}) = {} & \boldsymbol{C}_{\text{rad}}^{-1}\boldsymbol{H}_{\text{rad}}(\boldsymbol{\nu}_{\text{t}}) \\ & \times \left(\boldsymbol{H}_{\text{rad}}^{\mathsf{H}}(\boldsymbol{\nu}_{\text{t}})\boldsymbol{C}_{\text{rad}}^{-1}\boldsymbol{H}_{\text{rad}}(\boldsymbol{\nu}_{\text{t}})\right)^{-1/2},\end{aligned} \tag{4.29c}$$

where $\boldsymbol{H}_{\text{rad}}(\boldsymbol{\nu}_{\text{t}}) = \begin{bmatrix}\boldsymbol{h}(\boldsymbol{c}_{\text{re}},\nu_{\text{re,t}}) & \boldsymbol{h}(\boldsymbol{c}_{\text{tr}},\nu_{\text{tr,t}})\end{bmatrix}$. Then, upon exploiting the fact that the disturbance is Gaussian and after some elaborations, the rule in (4.27) can be recast as [62], [110]

$$\hat{\mathcal{H}} = \underset{\mathcal{L}\in\{\mathcal{H}_0,\mathcal{H}_{1,\text{tr}},\mathcal{H}_{1,\text{re}},\mathcal{H}_2\}}{\arg\max}\ \bar{\mu}(\mathcal{L}), \tag{4.30}$$

where

$$\bar{\mu}(\mathcal{L}) = \begin{cases} 0, & \text{if } \mathcal{L}=\mathcal{H}_0, \\ \max\limits_{\nu_{\text{tr,t}}\in\mathcal{V}_{\text{tr,t}}} \left|\boldsymbol{\xi}_{\text{tr}}^{\mathsf{H}}(\nu_{\text{tr,t}})\boldsymbol{y}_{\text{rad}}\right|^2 - \eta_{\text{rad}}, & \text{if } \mathcal{L}=\mathcal{H}_{1,\text{tr}}, \\ \max\limits_{\nu_{\text{re,t}}\in\mathcal{V}_{\text{re,t}}} \left|\boldsymbol{\xi}_{\text{re}}^{\mathsf{H}}(\nu_{\text{re,t}})\boldsymbol{y}_{\text{rad}}\right|^2 - \eta_{\text{rad}}, & \text{if } \mathcal{L}=\mathcal{H}_{1,\text{re}}, \\ \max\limits_{\boldsymbol{\nu}_{\text{t}}\in\mathcal{V}_{\text{tr,t}}\times\mathcal{V}_{\text{re,t}}} \left\|\boldsymbol{\Xi}^{\mathsf{H}}(\boldsymbol{\nu}_{\text{t}})\boldsymbol{y}_{\text{rad}}\right\|^2 - 2\eta_{\text{rad}}, & \text{if } \mathcal{L}=\mathcal{H}_2. \end{cases} \tag{4.31}$$

When a target is detected, an estimate of its Doppler shift (and hence radial velocity) is provided by the maximizer of the objective function in (4.31) under $\hat{\mathcal{H}}$.

Remark 9. The matrix $\boldsymbol{C}_{\text{rad}}$ in (4.20) is data-dependent, and its computation and inversion must be performed for each CPI; this entails a computational complexity of $\mathcal{O}\big((K_{\text{tr,c}} + K_{\text{re,c}})(P^2 + N_{\text{rad}} + N_{\text{ris}}) + P^3\big)$. The evaluation of the quantities in (4.29), for all $[\nu_{\text{tr,t}}; \nu_{\text{re,t}}] \in \mathcal{V}_{\text{tr,t}} \times \mathcal{V}_{\text{re,t}}$, has a cost of $\mathcal{O}\big(|\mathcal{V}_{\text{tr,t}}||\mathcal{V}_{\text{re,t}}|P^2\big)$. The computational complexity of the GIC-based rule in (4.30) is, therefore, $\mathcal{O}\big((K_{\text{tr,c}} + K_{\text{re,c}})(P^2 + N_{\text{rad}} + N_{\text{ris}}) + P^3 + |\mathcal{V}_{\text{tr,t}}||\mathcal{V}_{\text{re,t}}|P^2\big)$. If clutter can be mitigated by properly designing the two-way array power pattern, we can assume $\boldsymbol{C}_{\text{rad}} \simeq \sigma^2_{\text{rad}} \boldsymbol{I}_P$ at the design stage: this simplifies the implementation of the radar receiver and eliminates the need for prior knowledge of the clutter parameters. The computational cost of this reduced-complexity decision rule is $\mathcal{O}\big(|\mathcal{V}_{\text{tr,t}}||\mathcal{V}_{\text{re,t}}|P^2\big)$.

Remark 10. The implementation of the rule in (4.30) simplifies for sequential illumination. To verify this, let $\bar{\boldsymbol{y}}_{\text{rad}} \in \mathbb{C}^{P/2}$ and $\underline{\boldsymbol{y}}_{\text{rad}} \in \mathbb{C}^{P/2}$ be the vectors containing the first and the last half entries of $\boldsymbol{y}_{\text{rad}}$, respectively. Notice that, since the last half entries of $\boldsymbol{h}(\boldsymbol{c}_{\text{tr}}, \nu_{\text{tr,t}})$ and the first half entries of $\boldsymbol{h}(\boldsymbol{c}_{\text{re}}, \nu_{\text{re,t}})$ are zeros for sequential illumination, $\bar{\boldsymbol{y}}_{\text{rad}}$ and $\underline{\boldsymbol{y}}_{\text{rad}}$ only contain echoes originated from the transmissive and reflective half-spaces, respectively. Consequently, the solution in (4.30) can equivalently be obtained by running two independent binary tests, one for each half-space, namely,

$$\max_{\nu_{\text{tr,t}} \in \mathcal{V}_{\text{tr,t}}} \left| \bar{\boldsymbol{\xi}}^{\mathsf{H}}_{\text{tr}}(\nu_{\text{tr,t}}) \bar{\boldsymbol{y}}_{\text{rad}} \right|^2 \underset{\mathcal{H}^{\text{seq}}_{0,t}}{\overset{\mathcal{H}^{\text{seq}}_{1,t}}{\gtrless}} \eta_{\text{rad}}, \tag{4.32a}$$

$$\max_{\nu_{\text{re,t}} \in \mathcal{V}_{\text{re},t}} \left| \underline{\boldsymbol{\xi}}^{\mathsf{H}}_{\text{re}}(\nu_{\text{re,t}}) \underline{\boldsymbol{y}}_{\text{rad}} \right|^2 \underset{\mathcal{H}^{\text{seq}}_{0,r}}{\overset{\mathcal{H}^{\text{seq}}_{1,r}}{\gtrless}} \eta_{\text{rad}}, \tag{4.32b}$$

where $\bar{\boldsymbol{\xi}}_{\text{tr}}(\nu_{\text{tr,t}}) \in \mathbb{C}^{P/2}$ contains the first half entries of $\boldsymbol{\xi}_{\text{tr}}(\nu_{\text{tr,t}})$, while $\underline{\boldsymbol{\xi}}_{\text{re}}(\nu_{\text{re,t}}) \in \mathbb{C}^{P/2}$ the last half entries of $\boldsymbol{\xi}_{\text{re}}(\nu_{\text{re,t}})$; then, a decision $\hat{\mathcal{H}}$ is taken as follows:

- $\mathcal{H}_0$ is declared if $\mathcal{H}_{0,\text{tr}}^{\text{seq}}$ and $\mathcal{H}_{0,\text{re}}^{\text{seq}}$ are true;
- $\mathcal{H}_{1,\text{tr}}$ is declared if $\mathcal{H}_{1,\text{tr}}^{\text{seq}}$ and $\mathcal{H}_{0,\text{re}}^{\text{seq}}$ are true;
- $\mathcal{H}_{1,\text{re}}$ is declared if $\mathcal{H}_{0,\text{tr}}^{\text{seq}}$ and $\mathcal{H}_{1,\text{re}}^{\text{seq}}$ are true;
- $\mathcal{H}_2$ is declared if $\mathcal{H}_{1,\text{tr}}^{\text{seq}}$ and $\mathcal{H}_{1,\text{re}}^{\text{seq}}$ are true.

The joint Doppler search under hypothesis $\mathcal{H}_2$ is now bypassed. Additionally, the dimensions of the involved vectors and matrices are reduced; for instance, the vector

$$\bar{\boldsymbol{\xi}}_{\text{tr}}(\nu_{\text{tr,t}}) = \frac{\bar{\boldsymbol{C}}_{\text{rad}}^{-1}\bar{\boldsymbol{h}}(\boldsymbol{c}_{\text{tr}}, \nu_{\text{tr,t}})}{\|\bar{\boldsymbol{C}}_{\text{rad}}^{-1/2}\bar{\boldsymbol{h}}(\boldsymbol{c}_{\text{tr}}, \nu_{\text{tr,t}})\|}$$

is defined where $\bar{\boldsymbol{h}}(\boldsymbol{c}_{\text{tr}}, \nu_{\text{tr,t}})$ consists of the first half of the entries of $\boldsymbol{h}(\boldsymbol{c}_{\text{tr}}, \nu_{\text{tr,t}})$, and $\bar{\boldsymbol{C}}_{\text{rad}}$ denotes the principal submatrix of $\boldsymbol{C}_{\text{rad}}$ formed by removing the last $P/2$ rows and columns. The computational complexity in this case is $\mathcal{O}\big((K_{\text{tr,c}} + K_{\text{re,c}})(P^2 + N_{\text{rad}} + N_{\text{ris}}) + P^3 + (|\mathcal{V}_{\text{tr,t}}| + |\mathcal{V}_{\text{re,t}}|)P^2\big)$ and can be reduced to $\mathcal{O}\big((|\mathcal{V}_{\text{tr,t}}| + |\mathcal{V}_{\text{re,t}}|)P^2\big)$, if clutter is mitigated by properly designing the two-way array power pattern (see Remark 9).

4.3.4 Design of the communication receiver

Without loss of generality, assume simultaneous illumination and consider the user in the transmissive half-space: the same discussion applies for sequential illumination and/or for the user in the reflective half-space. To recover the codeword $[\boldsymbol{c}_{\text{tr}}]_{1:M} \in \mathcal{C}_{\text{tr}}$ from the measurements in (4.22), we resort to a ML decoder combined with a GIC-based rule to estimate the number of channel taps with non-zero amplitude [70].

For each $\boldsymbol{c} \in \mathcal{C}_{\text{tr}}$, define

$$T_{\text{tr}}(\boldsymbol{c}, \ell) = \frac{1}{\|\boldsymbol{c}\|^2}\left|\sum_{p=1}^{M} c^*(p) y_{\text{tr},u}(p, \ell)\right|^2, \tag{4.33}$$

for $\ell = 0, \ldots, L_{\mathrm{tr},u} - 1$, and

$$\hat{\ell}(\boldsymbol{c}) = \underset{\ell=0,\ldots,L_{\mathrm{tr},u}-1}{\arg\max} \; T_{\mathrm{tr}}(\boldsymbol{c}, \ell). \tag{4.34}$$

Then, as shown in Appendix B, an estimate of the transmitted codeword is

$$\hat{\boldsymbol{c}} = \underset{\boldsymbol{c}\in\mathcal{C}_{\mathrm{tr}}}{\arg\max} \left\{ T_{\mathrm{tr}}(\boldsymbol{c}, \hat{\ell}(\boldsymbol{c})) + \sum_{\ell=1,\, \ell\neq\hat{\ell}(\boldsymbol{c})}^{L_{\mathrm{tr},u}} \left(T_{\mathrm{tr}}(\boldsymbol{c}, \ell) - \eta_{\mathrm{com}} \right)^{+} \right\}, \tag{4.35}$$

where $\eta_{\mathrm{com}} \geq 0$ is a threshold that can be set so as to avoid using those measurements corresponding to channel taps that are weak (and therefore less reliable) or contain only noise. Here, we propose to select η_{com} to have a desired probability that the energy of a noise-only channel tap exceeds η_{com}, i.e., to have $\Pr(T_{\mathrm{tr}}(\boldsymbol{c}, \ell) > \eta_{\mathrm{com}} |\ \beta_{\mathrm{tr},u}(\ell) = 0) = \epsilon_{\mathrm{com}}$. Since $T_{\mathrm{tr}}(\boldsymbol{c}, \ell)$ is an exponential random variable with mean value σ^2_{com} when $\beta_{\mathrm{tr},u}(\ell) = 0$, we obtain $\eta_{\mathrm{com}} = \sigma^2_{\mathrm{com}} \ln(1/\epsilon_{\mathrm{com}})$. Observe that this receiver is quite simple. Indeed, the computational cost for evaluating the statistics in (4.33), for all $\boldsymbol{c} \in \mathcal{C}_{\mathrm{tr}}$ and $\ell \in \{0, \ldots, L_{\mathrm{tr},u}\}$, is $\mathcal{O}(L_{\mathrm{tr},u}|\mathcal{C}_{\mathrm{tr}}|M)$. Since $|\mathcal{C}_{\mathrm{tr}}| = 2^b \leq M$, the computational complexity of the GIC-based rule in (4.35) is $\mathcal{O}(L_{\mathrm{tr},u}M^2)$.

4.4 Performance analysis

This section provides the performance analysis of the proposed system, based on the parameters listed in Table 4.4. The feeder employs rectangular pulses. Both the STAR-RIS and the radar receiver array adopt a square planar structure with half-wavelength inter-element spacing. The element gain is modeled as:

$$G_{\mathrm{ris}}(\phi) = G_{\mathrm{rad}}(\phi) = \frac{\pi}{4} \cos^2 \phi^{\mathrm{az}} \cos^2 \phi^{\mathrm{el}}. \tag{4.36}$$

TABLE 4.4: System parameters

f_o	Carrier frequency	28 GHz
B	Bandwidth	50 MHz
$\mathcal{P}$	Pulse Power	30 dBm
T	PRI	0.25 ms
P	Number of PRIs	16
N_{ris}	Number of STAR-RIS elements	16×16
N_{rad}	Number of radar PESA elements	16×16
$\mathcal{V}_{\text{tr,t}}$	Target Doppler interval (tr. side)	$(1.75\,\text{kHz}, 2\,\text{kHz})$
$\mathcal{V}_{\text{re,t}}$	Target Doppler interval (re. side)	$(0.25\,\text{kHz}, 0.5\,\text{kHz})$
$\mathcal{V}_{\text{tr,c}}$	Clutter Doppler interval (tr. side)	$(-0.25\,\text{kHz}, 0.25\,\text{kHz})$
$\mathcal{V}_{\text{re,c}}$	Clutter Doppler interval (re. side)	$(-0.25\,\text{kHz}, 0.25\,\text{kHz})$
$\mathcal{F}_{\text{tr,t}}$	Target angular region (tr. side)	$(-2^\circ, 2^\circ) \times (-2^\circ, 2^\circ)$
$\mathcal{F}_{\text{re,t}}$	Target angular region (re. side)	$(178^\circ, 182^\circ) \times (-2^\circ, 2^\circ)$
$\mathcal{F}_{\text{tr,c}}$	Clutter angular region (tr. side)	$(202^\circ, 238^\circ) \times (-4^\circ, 4^\circ)$
$\mathcal{F}_{\text{re,c}}$	Clutter angular region (re. side)	$(-4^\circ, 4^\circ) \times (-58^\circ, -22^\circ)$
$\mathcal{F}_{\text{tr,u}}$	User angular region (tr. side)	$(138^\circ, 142^\circ) \times (-42^\circ, -38^\circ)$
$\mathcal{F}_{\text{re,u}}$	User angular region (re. side)	$(-42^\circ, -38^\circ) \times (-12^\circ, -8^\circ)$
σ^2_{rad}	Noise power spectral density	-164 dBm/Hz

The feeder and the STAR-RIS are placed in each other's far field, and the corresponding channel is modeled as:

$$\boldsymbol{g} = \left(\frac{G_{\mathrm{f}} G_{\mathrm{ris}}(\phi_{\mathrm{f}}) \lambda^2}{(4\pi)^2 d_{\mathrm{f}}^2} \right)^{\frac{1}{2}} \boldsymbol{u}_{\mathrm{ris}}(\phi_{\mathrm{f}}), \tag{4.37}$$

where $G_{\mathrm{f}} = 20$ dB denotes the antenna gain of the feeder, $d_{\mathrm{f}} = 3$ m is the distance between the feeder and the STAR-RIS, and $\phi_{\mathrm{f}} = [-45^\circ; 0^\circ]$ indicates the angular direction of the feeder.

Therefore, the unambiguous Doppler interval of the radar is given by $\big(-1/(2T), 1/(2T)\big)$, which corresponds to a maximum radial velocity of approximately 10.7 m/s when $1/(2T) = 2$ kHz. The Doppler resolution is $1/(PT) = 250$ Hz, corresponding to a radial velocity resolution of approximately 1.3 m/s for $P = 16$ [57].

The detection threshold η_{rad} for the GLRT is selected to yield an average false alarm probability of 10^{-4} under the null hypothesis $\mathcal{H}_0$, and the detection threshold for clutter is set to $\zeta_{\mathrm{c}} = -60$.

Target directions $\phi_{\mathrm{tr,t}}$ and $\phi_{\mathrm{re,t}}$ are uniformly sampled from the angular regions $\mathcal{F}_{\mathrm{tr,t}}$ and $\mathcal{F}_{\mathrm{re,t}}$, respectively. Their Doppler shifts $\nu_{\mathrm{tr,t}}$ and $\nu_{\mathrm{re,t}}$ are drawn uniformly from $\mathcal{V}_{\mathrm{tr,t}}$ and $\mathcal{V}_{\mathrm{re,t}}$, respectively. The target amplitudes $\alpha_{\mathrm{tr,t}}$ and $\alpha_{\mathrm{re,t}}$ are modeled according to a Swerling I fluctuation model and are generated as independent realizations of a circularly symmetric complex Gaussian variable with variance:

$$\sigma_{\mathrm{t}}^2 = \frac{\mathrm{RCS}_{\mathrm{t}}}{(4\pi)^2 d_{\mathrm{rad}}^4}, \tag{4.38}$$

where $\mathrm{RCS}_{\mathrm{t}}$ is the RCS of the target, and $d_{\mathrm{rad}} = 10$ m is the range under observation.

As to the clutter, we assume $K_{\mathrm{tr,c}} = K_{\mathrm{re,c}} = K_{\mathrm{c}}$, with $K_{\mathrm{c}} = 95$; $\{\phi_{\mathrm{tr,c},k}\}_{k=1}^{K_{\mathrm{c}}}$

and $\{\phi_{\text{re,c},k}\}_{k=1}^{K_\text{c}}$ are uniformly sampled from $\mathcal{F}_{\text{tr,c}}$ and $\mathcal{F}_{\text{re,c}}$, respectively; $\{\nu_{\text{tr,c},k}\}_{k=1}^{K_\text{c}}$ and $\{\nu_{\text{re,c},k}\}_{k=1}^{K_\text{c}}$ are uniformly sampled from $\mathcal{V}_{\text{tr,c}}$ and $\mathcal{V}_{\text{re,c}}$, respectively; finally,

$$\sigma_{\text{tr,c},k}^2 = \sigma_{\text{re,c},k}^2 = \frac{\text{RCS}_\text{c}}{(4\pi)^2 d_{\text{rad}}^4}, \tag{4.39}$$

where $\text{RCS}_\text{c} = 15$ dBsm is the clutter radar cross-section.

At the communication receiver, we set $\epsilon_{\text{com}} = 10^{-2}$. As to the users, we assume $L_{\text{tr,u}} = L_{\text{re,u}} = L_\text{u}$, $K_{\text{tr,u}} = K_{\text{re,u}} = K_\text{u}$, with $L_\text{u} = 15$ and $K_\text{u} = 3$; $\{\tau_{\text{tr,u},k}, \tau_{\text{re,u},k}\}_{k=1}^{K_\text{u}}$ are uniformly sampled from $\{\tau_{\text{tr,u,min}} + \ell/B\}_{\ell=0}^{L_\text{u}-1}$; $\{\phi_{\text{tr,u},k}\}_{k=1}^{K_\text{u}}$ and $\{\phi_{\text{re,u},k}\}_{k=1}^{K_\text{u}}$ are uniformly sampled from $\mathcal{F}_{\text{tr,u}}$ and $\mathcal{F}_{\text{re,u}}$, respectively; Rayleigh fading is considered, and $\{\alpha_{\text{tr,u},k}, \alpha_{\text{re,u},k}\}_{k=1}^{K_\text{u}}$ are generated as independent realizations of a circularly-symmetric complex Gaussian variable with variance σ_u^2; finally, for future reference, we define the communication SNR as

$$\text{SNR}_\text{com} = \frac{\mathcal{E} G_\text{ris}(\mathbf{0}_2) \|\boldsymbol{g}\|_1^2 \sigma_u^2 \zeta_\text{u} K_\text{u}}{L_\text{u} \sigma_\text{com}^2}. \tag{4.40}$$

4.4.1 Performance metrics

For the radar functionality, two metrics are considered: the PD and RMSE in estimating the target's radial velocity. The PD is defined as the probability of correctly deciding in favor of hypothesis $\mathcal{H}_2$ when it is indeed true.[4]

For the communication function, the BER, averaged over both users, is employed as the performance metric. The analysis of these metrics is carried out with respect to several following parameters, including the target's radar cross-section (RCS_t), the communication signal-to-noise ratio

[4]This work focuses on velocity estimation and detection performance. Although the radar processing is performed over discrete range bins (determined by the system bandwidth), range-estimation results are not reported here, since the considered radar-centric STAR-RIS setup and the chosen waveforms were optimized for Doppler sensing rather than for joint delay-Doppler estimation.

($\mathrm{SNR}_{\mathrm{com}}$), the peak value of the STAR-RIS array gain in the angular direction of the users (denoted as ζ_u), and the data encoding schemes outlined in Table 4.3.

Regarding radar performance, note that the test statistics in (4.32) is independent of the message transmitted to the users. More specifically, conditioned on the complex amplitude $\alpha_{\mathrm{tr,t}}$, the test statistic

$$2\left|\bar{\boldsymbol{\xi}}_{\mathrm{tr}}^{\mathrm{H}}(\nu_{\mathrm{tr,t}})\bar{\boldsymbol{y}}_{\mathrm{rad}}\right|^2$$

follows an exponential distribution with unit mean under the null hypothesis $\mathcal{H}_{0,\mathrm{tr}}^{\mathrm{seq}}$, and a noncentral chi-squared distribution with two degrees of freedom under the alternative hypothesis $\mathcal{H}_{1,\mathrm{tr}}^{\mathrm{seq}}$, having the following noncentrality parameter:

$$\begin{aligned}&2|\alpha_{\mathrm{tr,t}}|^2\left|\gamma_{\mathrm{tr}}(\boldsymbol{\phi}_{\mathrm{tr,t}};\boldsymbol{s}_{\mathrm{tr}},\boldsymbol{s}_{\mathrm{rad}})\right|^2\bar{\boldsymbol{d}}^{\mathrm{H}}(\nu_{\mathrm{tr,t}})\\&\left(\sigma_{\mathrm{rad}}^2\boldsymbol{I}_{P/2}+\sum_{k=1}^{K_{\mathrm{tr,c}}}\sigma_{\mathrm{tr,c},k}^2\left|\gamma_{\mathrm{tr}}(\boldsymbol{\phi}_{\mathrm{tr,c},k},\boldsymbol{s}_{\mathrm{tr}},\boldsymbol{s}_{\mathrm{rad}})\right|^2\bar{\boldsymbol{d}}(\nu_{\mathrm{tr,c},k})\bar{\boldsymbol{d}}^{\mathrm{H}}(\nu_{\mathrm{tr,c},k})\right)^{-1}\bar{\boldsymbol{d}}(\nu_{\mathrm{tr,t}}),\end{aligned}\tag{4.41}$$

where the vector $\bar{\boldsymbol{d}}(\nu)$ is defined as:

$$\bar{\boldsymbol{d}}(\nu)=\begin{bmatrix}1 & \mathrm{e}^{\mathrm{i}2\pi T\nu} & \cdots & \mathrm{e}^{\mathrm{i}2\pi T\nu(P/2-1)}\end{bmatrix}^{\mathrm{T}}.$$

An analogous argument applies to the test statistic

$$2\left|\underline{\boldsymbol{\xi}}_{\mathrm{re}}^{\mathrm{H}}(\nu_{\mathrm{re,t}})\underline{\boldsymbol{y}}_{\mathrm{rad}}\right|^2,$$

which exhibits the same statistical behavior. As a result, in the case of sequential illumination, radar performance is unaffected by the communication data (a desirable property). In contrast, for simultaneous illumination, radar performance generally depends on the data, although, as shown in

the next subsection, this dependency is relatively weak.

On the other hand, in the context of communication, the test statistics described in (4.33) are independent when conditioned on the coefficients $\{\beta_{\mathrm{tr},u}(\ell)\}_{\ell=0}^{L_{\mathrm{tr},u}-1}$. In particular, the quantity

$$\frac{2}{\sigma_{\mathrm{com}}^2} T_{\mathrm{tr}}(\boldsymbol{c}, \ell)$$

follows a noncentral chi-squared distribution with two degrees of freedom and noncentrality parameter

$$\frac{2\|\boldsymbol{c}_{\mathrm{tr}}\|^2 |\beta_{\mathrm{tr},u}(\ell)|^2}{\sigma_{\mathrm{com}}^2}$$

when $\boldsymbol{c} = \boldsymbol{c}_{\mathrm{tr}}$ and $\beta_{\mathrm{tr},u}(\ell) \neq 0$. In other cases, this quantity is exponentially distributed with unit mean. This analysis implies that the BER primarily depends on the number and energy of the codewords. As a result, for a given number of bits per symbol b, that is, for a given codebook size, the communication performance under simultaneous and sequential illumination becomes equivalent if the codeword length M in the simultaneous case is set to twice that used in the sequential case. This condition is satisfied in each row of Table 4.3, thereby ensuring equal transmission rates for both illumination modes.

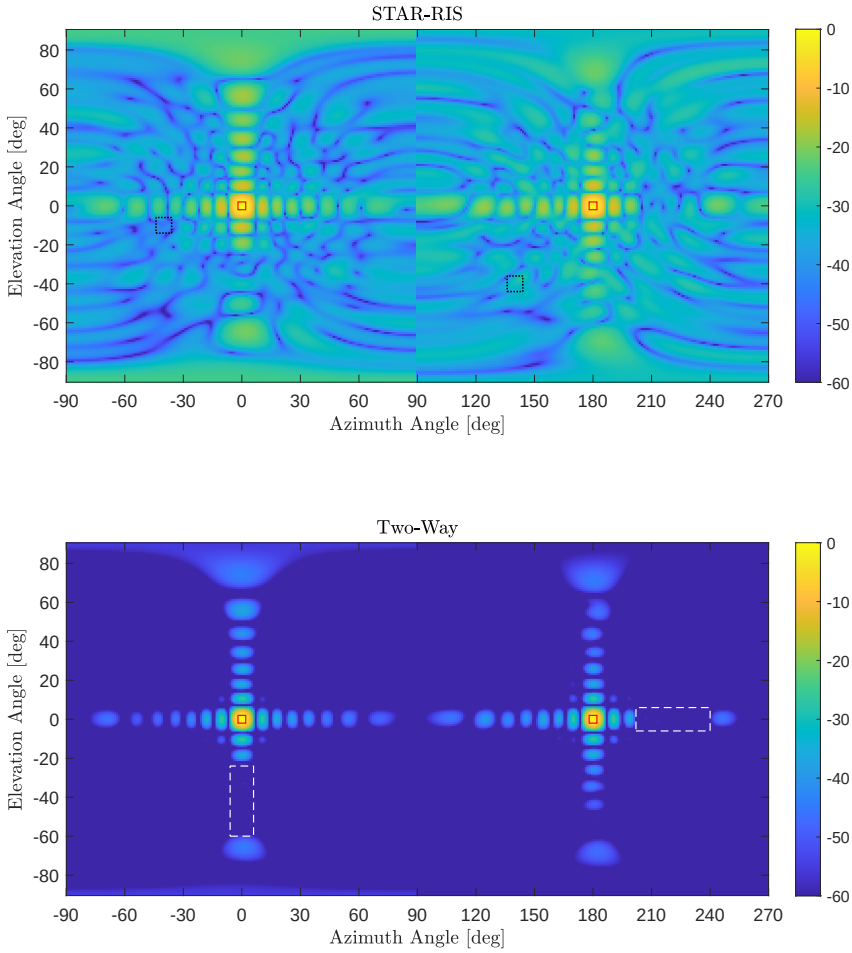

FIGURE 4.5: STAR-RIS (top) and two-way (bottom) array power patterns for $\zeta_{\mathrm{u}} = -\infty$. Red solid-line squares indicate the target regions; black dotted-line squares indicate the user regions; white dashed-line rectangles indicate the clutter regions.

4.4.2 Numerical results

We first analyze the ability to control the transmit and receive array response. Figure 4.5 shows the STAR-RIS and two-way array power patterns obtained by solving Problem (4.24) for $\zeta_{\mathrm{u}} = -\infty$ (the users' constraints are

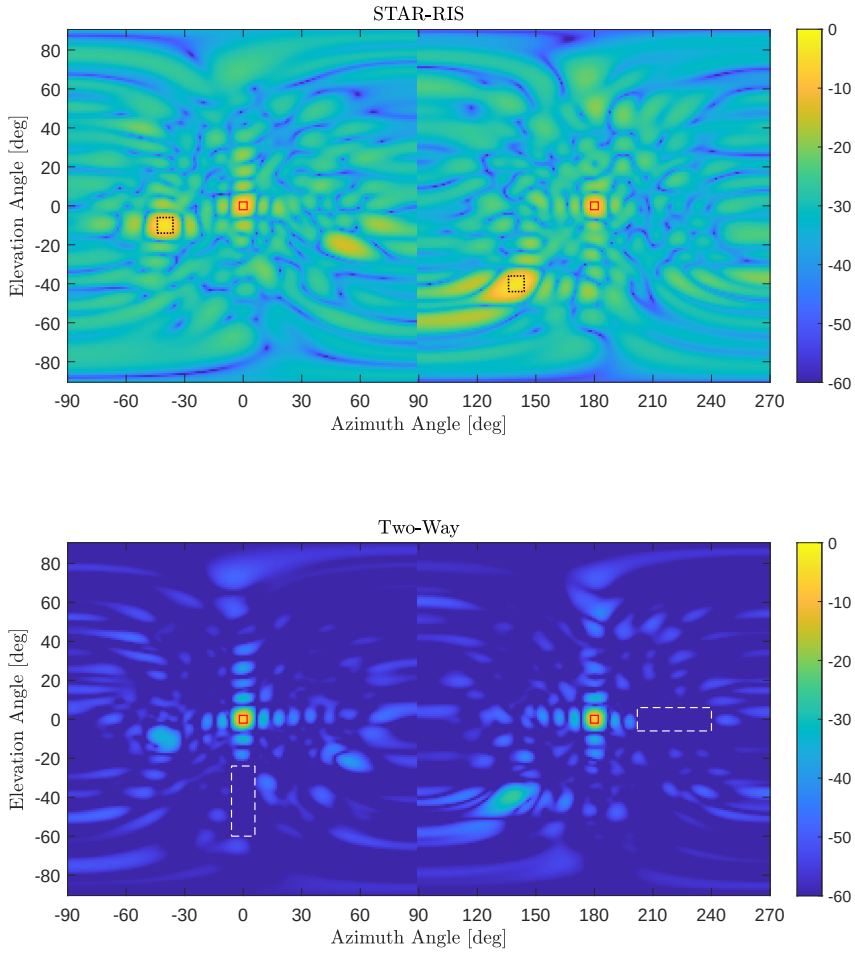

FIGURE 4.6: STAR-RIS (top) and two-way (bottom) array power patterns for $\zeta_{\mathrm{u}} = -5$ dB . Red solid-line squares indicate the target regions; black dotted-line squares indicate the user regions; white dashed-line rectangles indicate the clutter regions.

not active), while Figure 4.6 illustrates the results for $\zeta_{\mathrm{u}} = -5$ dB (the users' constraints are active). When $\zeta_{\mathrm{u}} = -\infty$, the STAR-RIS array power pattern only contains one sharp beam in each half-space that points towards the prospective target. Instead, for $\zeta_{\mathrm{u}} = -5$ dB, the STAR-RIS forms two beams in each half-space that point towards both the prospective target and

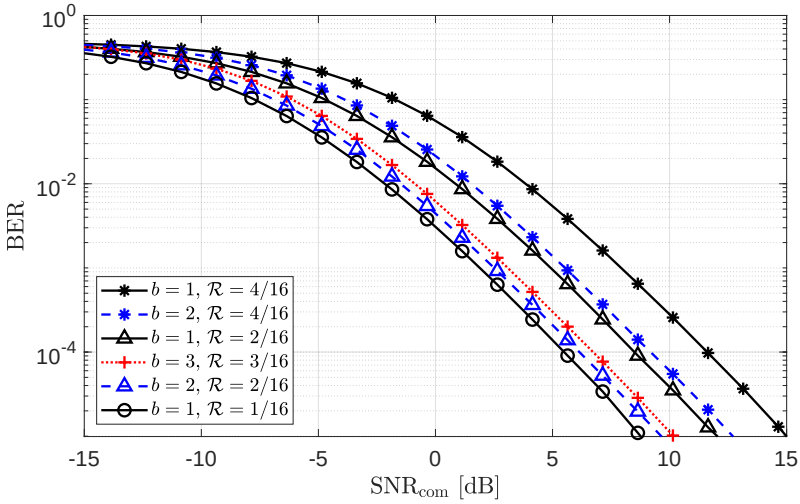

FIGURE 4.7: BER vs the communication SNR for simultaneous and sequential illumination and for different $(b, \mathcal{R})$ pairs when $\zeta_{\mathrm{u}} = -5$ dB and $\zeta_{\mathrm{c}} = -60$ dB.

the user, thus safeguarding the communication performance. In both cases, the two-way array power pattern only presents one sharp beam in each half-space, pointing towards the prospective target, and its sidelobes remain below -60 dB in the cluttered region $\mathcal{F}_{\mathrm{c}}$.

Next, we evaluate the impact of the proposed encoding rules on the system performance under the condition $\zeta_{\mathrm{u}} = -5$ dB. Fig. 4.7 presents BER versus $\mathrm{SNR}_{\mathrm{com}}$ for all cases listed in Table 4.3. Recall that, when $b = 1$, a transmission rate of $1/16$ is achieved by setting $M = 16$ for simultaneous illumination and $M = 8$ for sequential illumination. As discussed in Sec. 4.4.1, both configurations yield identical BER performance. A similar observation holds for the other $(b, \mathcal{R})$ pairs reported in Table 4.3. Fig. 4.8 presents PD and RMSE versus $\mathrm{RCS}_{\mathrm{t}}$ for both simultaneous and sequential illumination schemes. For sequential illumination, radar performance is independent of the specific $(b, \mathcal{R})$ pair, as discussed in Sec. 4.4.1. For simultaneous illumination, instead, we consider for illustration the two extreme

cases in Fig. 4.7, namely, $(b, \mathcal{R}) = (1, 4/16)$ and $(b, \mathcal{R}) = (1, 1/16)$. We also include the performance of a radar-only system, optimized for radar functionality by setting $\zeta_{\mathrm{u}} = -\infty$. Several key observations can be made.

- **Communication trade-offs:** Fig. 4.7 shows that different trade-offs between transmission rate and error performance can be achieved. For a fixed b (or equivalently, a fixed $\mathcal{R}$), the BER decreases as $\mathcal{R}$ decreases (or b increases). This is because the codeword length M increases, which in turn increases the received signal energy. For example, when comparing the extreme cases $(b, \mathcal{R}) = (1, 4/16)$ and $(b, \mathcal{R}) = (1, 1/16)$, the corresponding values of M differ by a factor 4, that results into a gap of about 6 dB.

- **Robustness of radar to encoding strategies:** Fig. 4.8 shows that, even under simultaneous illumination, the choice of $(b, \mathcal{R})$ has a negligible impact on radar performance. This further confirms the robustness of the radar function with respect to the specific encoding configuration.

- **Simultaneous vs. sequential illumination:**

  For a fixed $(b, \mathcal{R})$, sequential illumination offers several advantages over its simultaneous counterpart. First, it allows halving the time slot duration, which is beneficial when the coherence time of the user channel is limited. Second, it avoids temporal overlap of echoes from the two half-spaces, simplifying implementation of the radar detector as discussed in Sec. 4.3.3. Third, as illustrated in Fig. 4.8 (top), it offers slightly improved detection performance. However, this comes at the cost of halving the illumination time per half-space, which doubles the radar Doppler resolution compared to simultaneous illumination.

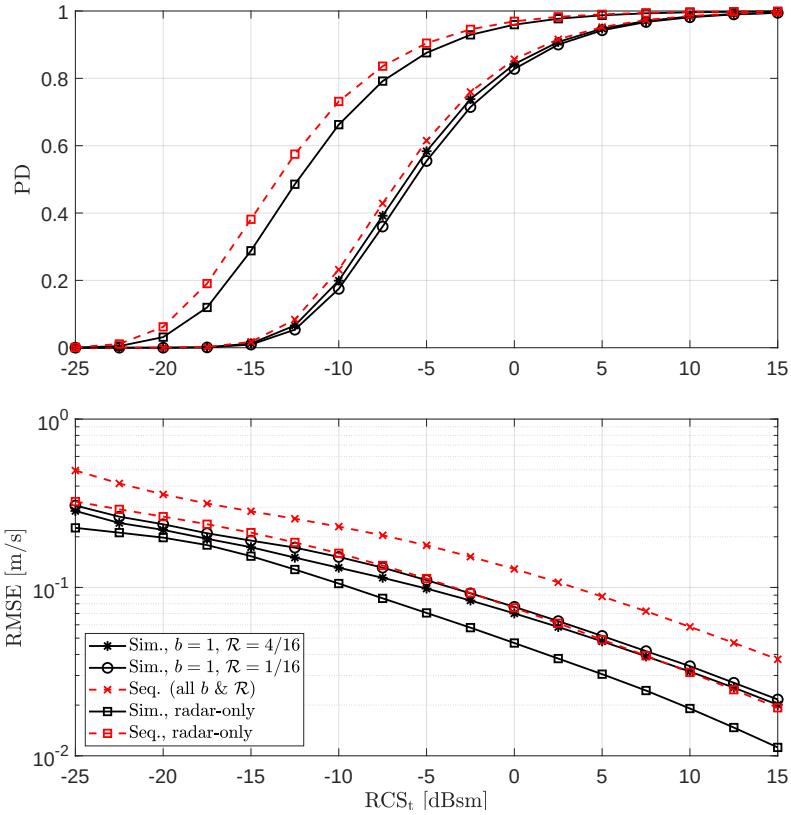

FIGURE 4.8: PD (top) and RMSE (bottom) versus RCS$_t$ for simultaneous and sequential illumination and for different $(b, \mathcal{R})$ pairs when $\zeta_u = -5$ dB and $\zeta_c = -60$ dB; for comparison, the radar-only scenario (where $\zeta_u = -\infty$ dB) is also included.

Consequently, sequential illumination results in a higher RMSE, as shown in Fig. 4.8 (bottom).

- **Effect of communication on radar performance:** The integration of the communication functionality leads to a degradation in radar performance. Compared to the radar-only scenario (i.e., when $\zeta_u = -\infty$), a performance loss of approximately 5 dBsm is observed. This reduction primarily results from the STAR-RIS redirecting only a fraction

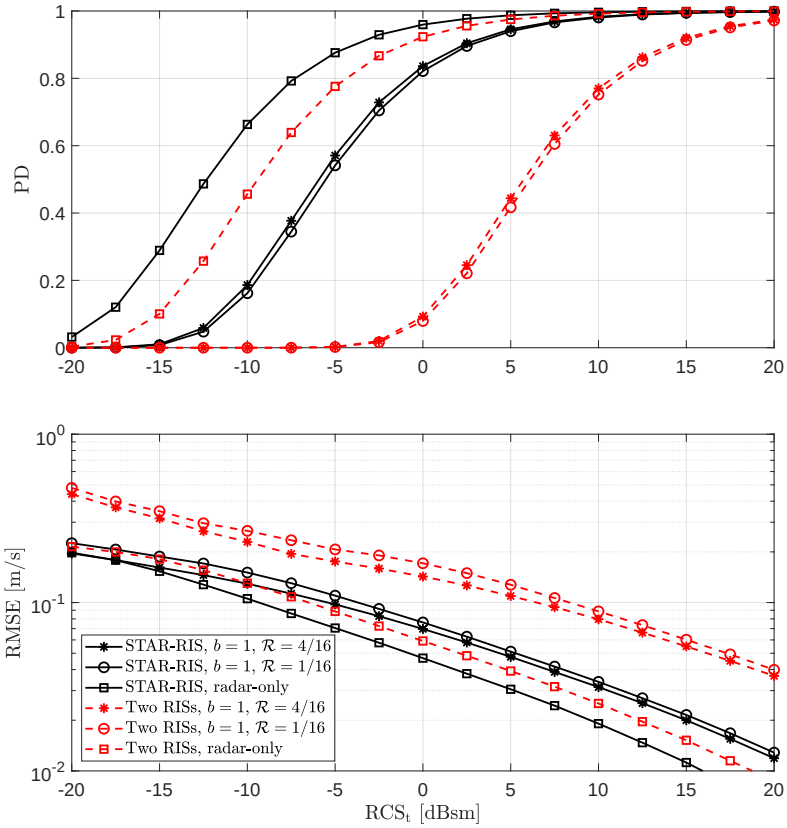

FIGURE 4.9: PD (top) and RMSE (bottom) versus RCS_t for simultaneous illumination and for two $(b, \mathcal{R})$ pairs when $\zeta_\text{u} = -5$ dB and $\zeta_\text{c} = -60$ dB; the radar-only case is also considered, and the Two RISs traditional system is included for comparison.

of the incident energy toward the target, whereas the embedded information signal has a negligible impact. This behavior is supported by the results in Fig. 4.5 and, Fig. 4.6 , where the gain directed toward the target in both the STAR-RIS and the two-way array power patterns drops by approximately 5 dB as ζ_u increases from $-\infty$ to -5 dB.

We also provide a quantitative comparison against a *traditional* RIS baseline that achieves full-space coverage using two panels: one transmissive and one reflective, each with $N_\text{ris}/2$ elements. This configuration, referred

to as the *Two RISs* scheme, ensures the total aperture equals that of the proposed STAR-RIS. We focus on the simultaneous illumination mode, where both RRIS panels are active in every PRI, enabling concurrent dual-side sensing and communication. For fairness, the beampattern constraints are set such that the Two RISs system sends the same power toward the users' directions and receives the same power from the clutter region as the STAR-RIS system.

Fig. 4.9 presents PD and RMSE versus $\mathrm{RCS_t}$ for the two compared systems; two pairs of $(b, \mathcal{R})$ are reported, along with the radar-only case. Thanks to the adopted setting for the beampattern design, the users in both the STAR-RIS and Two RISs cases experience the same BER. From Fig. 4.9, it is seen that the proposed STAR-RIS-based architecture gains about 3 dB over the Two-RISs one, in the radar-only case, and about 12 dB, in the ISAC scenario. The superior performance is due to the higher number of elements. Indeed, although each element of the STAR-RISs scheme splits the incident power between the two sides, the double number of elements grants a higher array gain and a higher number of degrees of freedom for beampattern design. In particular, the latter point becomes quite relevant in the presence of the communication function.

Finally, we examine the sensing-communication tradeoff in greater detail by decreasing ζ_u from -2 dB to -70 dB. Fig. 4.10 presents the resulting values of PD and RMSE versus BER for $\mathrm{RCS_t} = 0, 5, 10$ dBsm and two operating scenarios for the users. The radar performance is marginally affected by the communication function when the desired BER is not lower than 10^{-4} for $\mathrm{SNR_{com}} = 11.5$ dB or $5 \cdot 10^{-3}$ for $\mathrm{SNR_{com}} = 5.5$ dB. Further reducing the BER requires the STAR-RIS to redirect nearly all the incident energy toward the user, which significantly degrades radar performance.

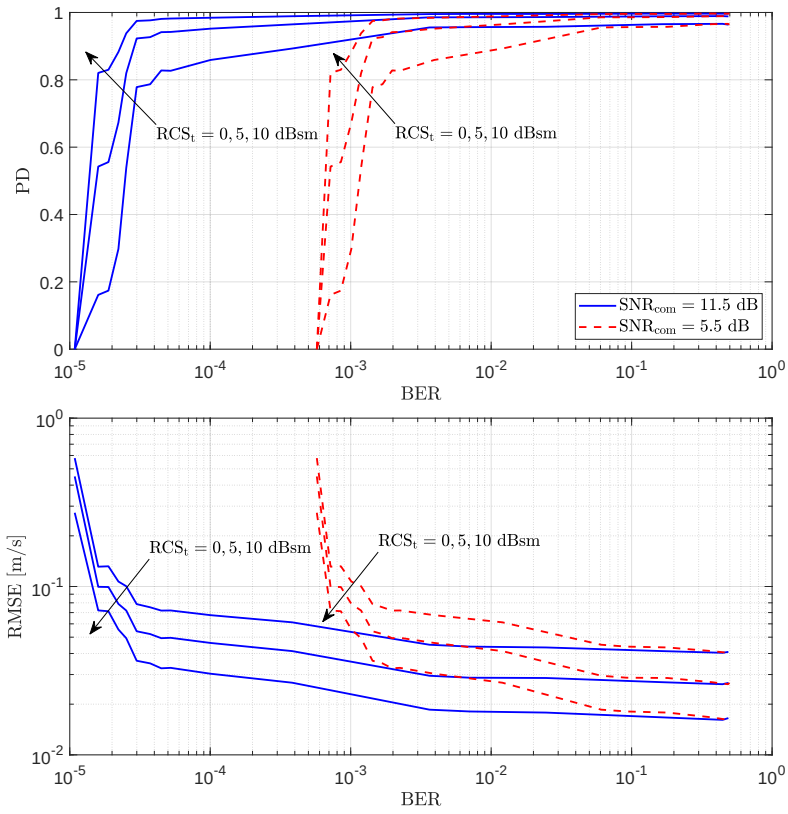

FIGURE 4.10: PD (top) and RMSE (bottom) versus BER for $\zeta_c = -60$ dB and varying ζ_u, when the simultaneous illumination is adopted, $b = 1$, and $\mathcal{R} = 4/16$. Two operating scenarios are considered for the communication users that correspond to have $\text{SNR}_{\text{com}} = 5.5$ dB and 11.5 dB when $\zeta_u = -5$ dB.

4.5 Conclusions

This paper presented a radar-centric ISAC architecture that exploits a feeder emitting a periodic pulse train, a passive STAR-RIS, and a radar receiver equipped with a PESA and a single digital channel. A joint design of the STAR-RIS spatial response and the radar analog beamformer was proposed to maximize the two-way array power pattern in the directions of interest to the radar, while mitigating clutter and safeguarding communication.

Two encoding schemes were introduced to govern the STAR-RIS modulation across pulse repetition intervals, enabling either simultaneous or sequential illumination of the two half-spaces; these schemes support both radar target separability and blind communication decoding through the use of orthogonal binary codewords. Finally, the design of the radar and communication receivers were developed under a GIC-based framework.

The analysis demonstrated that different trade-offs between radar and communication functionalities are achievable by balancing the amounts of power redirected towards prospective targets and users. The proposed encoding schemes also allow for flexible trade-offs between transmission rate and BER with a minimal impact on radar performance, which was evaluated in terms of PD and RMSE in estimating target radial velocity. Notably, simultaneous illumination provides improved velocity estimation due to the processing of a longer pulse train, whereas sequential illumination simplifies radar detection by ensuring non-overlapping echoes from the two half-spaces.

The analysis developed in this chapter can be extended in several relevant directions. A natural first step is the study of heterogeneous clutter scenarios, where clutter returns may originate from regions with diverse spatial and statistical characteristics. Incorporating these effects would enable a more realistic assessment of the proposed radar-centric STAR-RIS architecture and may motivate the use of models beyond the adopted GIC formulation.

In addition, the grid-based discretization employed in the optimization framework of Sec. 4.3.1 could be replaced by adaptive strategies capable of estimating dominant directions of users, targets, and clutter without relying on a fixed spatial grid. Techniques based on sparse Bayesian learning,

subspace tracking, or adaptive beamspace refinement represent promising options in this context.

Another avenue for future research is to extend the system model beyond point-like targets to include extended targets and near-field propagation effects. This would allow a more comprehensive evaluation of the ISAC performance of STAR-RIS-assisted systems in scenarios where wavefront curvature, spatial spread, and range-dependent phase variations become significant.

While this work focuses primarily on the estimation of target velocity (via Doppler), incorporating range estimation into the sensing process would enhance the system's ISAC capabilities. For instance, joint delay-Doppler estimation methods or the use of non-standard probing waveforms may be explored.

Moreover, future work may investigate adaptive or learning-based beamforming strategies that exploit users' CSI, enabling more flexible illumination patterns and helping to mitigate range or Doppler ambiguities. Finally, further efforts are needed to evaluate system performance under more complex and dynamic environments to quantify the impact of hardware impairments, and to conduct experimental validations that assess real-world feasibility.

Chapter 5

Conclusions

Summary and outlook

This thesis explored the potential of RIS to enhance radar sensing and support ISAC in future wireless networks. The research focused on designing architectures that make practical use of both active RIS and passive STAR-RIS technologies, particularly in radar-centric applications.

In Chapter 2, we examined an active RIS-aided monostatic radar system, tackling the fundamental issue of signal degradation in indirect echo paths. By placing an active RIS in the scene and modeling its interaction with the radar signal path, we proposed a framework where both direct and RIS-reflected echoes could be used jointly for improved target detection and localization. The problem was formalized using a GLRT, and the system's performance was analyzed under various configurations. The results demonstrated that with careful control of amplification gain and optimized placement, active RIS can significantly enhance radar sensing performance.

Chapter 3 introduced a novel Doppler radar architecture using a STAR-RIS, which enables wave control in both reflective and transmissive directions. The radar system implements a slow-time modulation scheme to distinguish between echoes from different sides of the surface. Two scanning protocols were proposed (sequential and simultaneous), each offering

trade-offs between hardware simplicity and estimation accuracy. These results demonstrate that programmable metasurfaces such as STAR-RIS can support dual-sided radar sensing, and that operating modes can be flexibly selected to meet varying accuracy and complexity requirements.

Chapter 4 presented a radar-centric ISAC transceiver that combines a passive STAR-RIS, a periodic pulse feeder, and a radar receiver equipped with a PESA and a single digital channel. Unlike the fully digital phased array architecture described in Chapter 3, the system presented here emphasizes hardware simplicity. By transferring complexity to the analog domain, it enables reliable dual-functionality while significantly reducing implementation cost and power consumption. This move toward a single-channel, low-complexity design represents a practical step toward realizing deployable ISAC systems. The architecture leverages space-time modulation at the STAR-RIS to enable directional control across both reflective and transmissive domains, supporting coexisting radar and communication functionalities within shared hardware constraints. To facilitate dual-function operation, two encoding schemes were developed to govern the STAR-RIS's behavior across pulse repetition intervals. These schemes allow either simultaneous or sequential illumination of both half-spaces, enabling target separability for radar sensing and blind message decoding for communication users through the use of orthogonal binary codewords. The system evaluation demonstrated that radar accuracy and communication reliability can be effectively balanced by adjusting the spatial beam patterns and coding strategies. Simultaneous illumination improves Doppler resolution through longer coherent integration, while sequential illumination avoids echo overlap, simplifying detection and estimation. Importantly, all functions are achieved without relying on high-speed switching or additional

communication waveforms, making the design compatible with practical passive metasurface hardware. Overall, this chapter has established the viability of using programmable surfaces to support low-complexity ISAC systems. By embedding communication features directly into radar operations and jointly optimizing analog beamforming and metasurface control, the proposed system enables spectrum-efficient, hardware-aware operation. These insights provide a solid foundation for future RIS-assisted designs aimed at supporting sensing and data delivery in 6G networks and beyond.

Future Work

While this thesis systems offer meaningful progress toward RIS-enabled sensing and ISAC, several directions remain open for further exploration. A key area of advancement is system adaptivity. The current designs rely on pre-defined beamforming and modulation strategies, which can perform well in static environments but may degrade in dynamic or time-varying scenarios. Incorporating adaptive or learning-based methods, such as reinforcement learning or feedback-driven optimization, could enable real-time adjustment to user movement or changing channel conditions. This would significantly improve robustness in mobile or decentralized use cases, especially when full channel state information is unavailable.

Another direction involves increasing realism in the modeling of propagation and channel conditions. This work has used simplified models; however, introducing more practical environments, including Rician fading, correlated multipath propagation, and interference from multiple users, would provide a more accurate picture of system performance in real-world deployments.

Furthermore, future work should consider practical hardware limitations. While idealized hardware assumptions simplify the analysis, real-world RISs and STAR-RISs suffer from quantized phase control, control latency, limited switching speed, and non-linearities in electromagnetic behavior. New algorithms that explicitly account for these imperfections and remain effective under such constraints will be essential for transitioning from theoretical models to deployable systems.

Recent developments in multi-layer or stacked RISs suggest another promising extension. By layering programmable surfaces, it is possible to enhance spatial resolution and control flexibility. However, this also introduces new challenges, such as managing inter-layer coupling and increased system complexity, which will require innovative design solutions.

HRISs, which integrate a small number of active components or embedded sensors into an otherwise passive surface, open up new opportunities for ISAC. These hybrid architectures can support local signal observation, partial channel estimation, and increased environmental awareness. Future research could investigate how HRISs contribute to sensing tasks such as motion tracking, self-localization, or autonomous surface calibration, particularly in use cases like UAV-mounted communication nodes or rapidly deployed smart infrastructure.

Finally, experimental validation remains a critical step. While simulation offers valuable insights, testing the proposed algorithms on physical RISs or STAR-RISs would help evaluate their practical effectiveness. This includes analyzing the impact of hardware latency, phase inaccuracies, and fluctuating environmental conditions. Even small-scale prototypes can provide significant feedback for refining theoretical models and guiding future development.

Together, these directions support a transition from theoretical models to real-world deployment. They are well aligned with the evolving requirements of intelligent and reconfigurable environments in applications such as vehicular communications, UAV-based platforms, and industrial IoT systems. Continued progress in these areas will be critical for realizing the full potential of RIS-enabled ISAC in the context of future 6G networks.

Appendix A

Suboptimum solution to Problem (4.24)

Let $M_{\mathrm{c}} = \mathrm{card}(\bar{\mathcal{F}}_{\mathrm{c}})$, $M_{\mathrm{u}} = \mathrm{card}(\bar{\mathcal{F}}_{\mathrm{u}})$, and $M = M_{\mathrm{c}} + M_{\mathrm{u}}$. Denote by $\{\boldsymbol{\phi}_i\}_{i=1}^{M_{\mathrm{c}}}$ and $\{\boldsymbol{\phi}_i\}_{i=M_{\mathrm{c}}+1}^{M}$ the angular directions contained in the sets $\bar{\mathcal{F}}_{\mathrm{c}}$ and $\bar{\mathcal{F}}_{\mathrm{u}}$, respectively. Let $N = 2N_{\mathrm{ris}} + N_{\mathrm{rad}}$ and define

$$\boldsymbol{s} = \left[\boldsymbol{s}_{\mathrm{tr}};\quad \boldsymbol{s}_{\mathrm{re}};\quad \boldsymbol{s}_{\mathrm{rad}}\right] \in \mathbb{C}^N, \tag{A.1}$$

$$f(\boldsymbol{s}) = -\sum_{\boldsymbol{\phi}\in\bar{\mathcal{F}}_{\mathrm{t}}} \mathrm{A}(\boldsymbol{\phi}; \boldsymbol{s}_{\mathrm{tr}}, \boldsymbol{s}_{\mathrm{re}}, \boldsymbol{s}_{\mathrm{rad}}), \tag{A.2}$$

$$q_i(\boldsymbol{s}) = \begin{cases} \frac{1}{\zeta_c}\mathrm{A}(\boldsymbol{\phi}_i; \boldsymbol{s}_{\mathrm{tr}}, \boldsymbol{s}_{\mathrm{re}}, \boldsymbol{s}_{\mathrm{rad}}) - 1, & \text{if } i \le M_{\mathrm{c}} \\ 1 - \frac{1}{\zeta_u}\mathrm{A}_{\mathrm{ris}}(\boldsymbol{\phi}_i; \boldsymbol{s}_{\mathrm{tr}}, \boldsymbol{s}_{\mathrm{re}}), & \text{if } i > M_{\mathrm{c}}. \end{cases} \tag{A.3}$$

Then, Problem (4.24) can be rewritten as

$$\begin{aligned} &\min_{\boldsymbol{s}\in\mathbb{C}^N} f(\boldsymbol{s}), \\ &\text{s.t. } q_i(\boldsymbol{s}) \le 1, \quad i = 1, \ldots, M, \\ &\qquad |s_n| = 1, \quad n = 1, \ldots, N. \end{aligned} \tag{A.4}$$

Next we derive a suboptimal solution to (A.4) by resorting to the augmented Lagrangian method with partial elimination of the constraints [105]. After introducing the slack variables $\boldsymbol{z} \in \mathbb{R}^M$, the inequality

constraints are converted into equality constrains, and Problem (A.4) is reformulated as

$$\begin{aligned} \min_{\boldsymbol{s}\in\mathbb{C}^N,\boldsymbol{z}\in\mathbb{R}^M} & f(\boldsymbol{s}), \\ \text{s.t. } & q_i(\boldsymbol{s}) + z_i = 0, \quad i = 1,\dots,M, \\ & z_i \geq 0, \quad i = 1,\dots,M, \\ & |s_n| = 1, \quad n = 1,\dots,N. \end{aligned} \tag{A.5}$$

The augmented Lagrangian for this problem is

$$\bar{\mathcal{L}}_\mu(\boldsymbol{s},\boldsymbol{z},\boldsymbol{\lambda}) = f(\boldsymbol{s}) + \sum_{i=1}^{M}\left[\lambda_i\big(q_i(\boldsymbol{s})+z_i\big) + \frac{\mu}{2}\big(q_i(\boldsymbol{s})+z_i\big)^2\right], \tag{A.6}$$

where the constraints $|s_i| = 1$ have not been eliminated by means of a penalty. Instead, they are handled directly in the minimization of the Lagrangian function, i.e.,

$$\begin{aligned} \min_{\boldsymbol{s}\in\mathbb{C}^N,\boldsymbol{z}\in\mathbb{R}^M} & \bar{\mathcal{L}}_\mu(\boldsymbol{s},\boldsymbol{z},\boldsymbol{\lambda}), \\ \text{s.t. } & z_i \geq 0, \quad i = 1,\dots,M, \\ & |s_n| = 1, \quad n = 1,\dots,N. \end{aligned} \tag{A.7}$$

For fixed $\boldsymbol{s}$, the minimization over $\boldsymbol{z}$ gives $z_i = \left(-\left(\lambda_i/\mu + q_i(\boldsymbol{s})\right)\right)^+$, where $z^+ = \max\{z, 0\}$. Therefore, the constraint $q_i(\boldsymbol{s}) + z_i = 0$ in (A.5) becomes $\max\left\{q_i(\boldsymbol{s}), -\lambda_i/\mu\right\} = 0$, and Problem (A.7) reduces to

$$\min_{\boldsymbol{s}\in\mathbb{C}^N} \ \mathcal{L}_\mu(\boldsymbol{s},\boldsymbol{\lambda}), \quad \text{s.t. } |s_n| = 1, \quad n = 1,\dots,N. \tag{A.8}$$

where

$$\mathcal{L}_\mu(\boldsymbol{s},\boldsymbol{\lambda}) = f(\boldsymbol{s}) + \frac{1}{2\mu}\sum_{i=1}^{M}\left[\Big(\big(\lambda_i + \mu q_i(\boldsymbol{s})\big)^+\Big)^2 - \lambda_i^2\right]. \tag{A.9}$$

Problem (A.8) can be solved using the gradient projection method; in this case, the n-th iteration takes the form

$$\boldsymbol{s}^{(n)} = \Pi\left(\boldsymbol{s}^{(n-1)} - \xi^{(n)} \nabla \mathcal{L}_{\mu}\big(\boldsymbol{s}^{(n-1)}, \boldsymbol{\lambda}\big)\right), \tag{A.10}$$

where Π is the projector on the N-dimensional unit-modulus torus (i.e., $\Pi(\boldsymbol{s}) = \boldsymbol{\omega} \in \mathbb{C}^N$, with $\omega_i = s_i/|s_i|$, for $i = 1, \ldots, N$), $\xi^{(n)}$ is the stepsize at the n-th iteration, and

$$\nabla \mathcal{L}_{\mu}(\boldsymbol{s}, \boldsymbol{\lambda}) = \nabla f(\boldsymbol{s}) + \sum_{i=1}^{M} \big(\lambda_i + \mu q_i(\boldsymbol{s})\big)^{+} \nabla q_i(\boldsymbol{s}), \tag{A.11}$$

is the gradient of $L_{\mu}(\boldsymbol{s}, \boldsymbol{\lambda})$. From (4.18), (A.2), and (A.3),

$$\nabla f(\boldsymbol{s}) = -\sum_{\boldsymbol{\phi} \in \bar{\mathcal{F}}_{\mathrm{t}}} \begin{bmatrix} \frac{\partial \mathrm{A}_{\mathrm{ris}}(\boldsymbol{\phi}; \boldsymbol{s}_{\mathrm{tr}}, \boldsymbol{s}_{\mathrm{re}})}{\partial \boldsymbol{s}_{\mathrm{tr}}} \mathrm{A}_{\mathrm{rad}}(\boldsymbol{\phi}; \boldsymbol{s}_{\mathrm{rad}}) \\ \frac{\partial \mathrm{A}_{\mathrm{ris}}(\boldsymbol{\phi}; \boldsymbol{s}_{\mathrm{tr}}, \boldsymbol{s}_{\mathrm{re}})}{\partial \boldsymbol{s}_{\mathrm{re}}} \mathrm{A}_{\mathrm{rad}}(\boldsymbol{\phi}; \boldsymbol{s}_{\mathrm{rad}}) \\ \mathrm{A}_{\mathrm{ris}}(\boldsymbol{\phi}; \boldsymbol{s}_{\mathrm{tr}}, \boldsymbol{s}_{\mathrm{re}}) \frac{\partial \mathrm{A}_{\mathrm{rad}}(\boldsymbol{\phi}; \boldsymbol{s}_{\mathrm{rad}})}{\partial \boldsymbol{s}_{\mathrm{tr}}} \end{bmatrix}, \tag{A.12a}$$

$$\nabla q_i(\boldsymbol{s}) = \begin{cases} \frac{1}{\zeta_c} \begin{bmatrix} \frac{\partial \mathrm{A}_{\mathrm{ris}}(\boldsymbol{\phi}_i; \boldsymbol{s}_{\mathrm{tr}}, \boldsymbol{s}_{\mathrm{re}})}{\partial \boldsymbol{s}_{\mathrm{tr}}} \mathrm{A}_{\mathrm{rad}}(\boldsymbol{\phi}_i; \boldsymbol{s}_{\mathrm{rad}}) \\ \frac{\partial \mathrm{A}_{\mathrm{ris}}(\boldsymbol{\phi}_i; \boldsymbol{s}_{\mathrm{tr}}, \boldsymbol{s}_{\mathrm{re}})}{\partial \boldsymbol{s}_{\mathrm{re}}} \mathrm{A}_{\mathrm{rad}}(\boldsymbol{\phi}_i; \boldsymbol{s}_{\mathrm{rad}}) \\ \mathrm{A}_{\mathrm{ris}}(\boldsymbol{\phi}_i; \boldsymbol{s}_{\mathrm{tr}}, \boldsymbol{s}_{\mathrm{re}}) \frac{\partial \mathrm{A}_{\mathrm{rad}}(\boldsymbol{\phi}_i; \boldsymbol{s}_{\mathrm{rad}})}{\partial \boldsymbol{s}_{\mathrm{tr}}} \end{bmatrix}, \text{ if } i \leq M_{\mathrm{c}}, \\ -\frac{1}{\zeta_u} \begin{bmatrix} \frac{\partial \mathrm{A}_{\mathrm{ris}}(\boldsymbol{\phi}_i; \boldsymbol{s}_{\mathrm{tr}}, \boldsymbol{s}_{\mathrm{re}})}{\partial \boldsymbol{s}_{\mathrm{tr}}} \\ \frac{\partial \mathrm{A}_{\mathrm{ris}}(\boldsymbol{\phi}_i; \boldsymbol{s}_{\mathrm{tr}}, \boldsymbol{s}_{\mathrm{re}})}{\partial \boldsymbol{s}_{\mathrm{re}}} \\ \mathbf{0}_{N_{\mathrm{rad}}} \end{bmatrix}, \text{ if } i \geq M_{\mathrm{c}} + 1, \end{cases} \tag{A.12b}$$

where, from (4.6), (4.7a), (4.7b), and (4.9),

$$\begin{aligned} \frac{\partial \mathrm{A}_{\mathrm{ris}}(\boldsymbol{\phi}; \boldsymbol{s}_{\mathrm{tr}}, \boldsymbol{s}_{\mathrm{re}})}{\partial \boldsymbol{s}_{\mathrm{tr}}} &= \frac{2}{\|\boldsymbol{g}\|_1^2} (\boldsymbol{u}_{\mathrm{ris}}^{\mathsf{T}}(\boldsymbol{\phi}) \mathrm{diag}\{\boldsymbol{g}\} \boldsymbol{s}_{\mathrm{tr}}) \\ &\quad \times \mathrm{diag}\{\boldsymbol{g}^*\} \boldsymbol{u}_{\mathrm{ris}}^*(\boldsymbol{\phi}) \mathbb{1}_{\{\boldsymbol{\phi} \in \mathcal{F}_{\mathrm{tr}}\}}, \end{aligned} \tag{A.13a}$$

$$\begin{aligned} \frac{\partial \mathrm{A}_{\mathrm{ris}}(\boldsymbol{\phi}; \boldsymbol{s}_{\mathrm{tr}}, \boldsymbol{s}_{\mathrm{re}})}{\partial \boldsymbol{s}_{\mathrm{re}}} &= \frac{2}{\|\boldsymbol{g}\|_1^2} (\boldsymbol{u}_{\mathrm{ris}}^{\mathsf{T}}(\boldsymbol{\phi}) \mathrm{diag}\{\boldsymbol{g}\} \boldsymbol{s}_{\mathrm{re}}) \\ &\quad \times \mathrm{diag}\{\boldsymbol{g}^*\} \boldsymbol{u}_{\mathrm{ris}}^*(\boldsymbol{\phi}) \mathbb{1}_{\{\boldsymbol{\phi} \in \mathcal{F}_{\mathrm{tr}}\}}, \end{aligned} \tag{A.13b}$$

$$\frac{\partial \mathrm{A}_{\mathrm{rad}}(\boldsymbol{\phi}; \boldsymbol{s}_{\mathrm{rad}})}{\partial \boldsymbol{s}_{\mathrm{rad}}} = \frac{2}{N_{\mathrm{rad}}^2} (\boldsymbol{u}_{\mathrm{rad}}^{\mathsf{H}}(\boldsymbol{\phi}) \boldsymbol{s}_{\mathrm{rad}}) \boldsymbol{u}_{\mathrm{rad}}(\boldsymbol{\phi}). \tag{A.13c}$$

Algorithm 1 Sub-optimal solution to Problem (A.4)

choose $\boldsymbol{s} \in \mathbb{C}^N$, $\boldsymbol{\lambda} \in \mathbb{R}^M$, $\eta^{\bigstar} \in \mathbb{R}$, and $\omega^{\bigstar} \in \mathbb{R}$
Set $\mu = 10$, $\omega = 0.1$, and $\eta = 0.1$
repeat
  $\omega = \max\{\omega^{\bigstar}, \omega/2^{0.5}\}$
  repeat
    compute $\nabla \mathcal{L}_{\mu}(\boldsymbol{s}, \boldsymbol{\lambda})$
    set the stepsize ξ
    $\boldsymbol{s} = \Pi\big(\boldsymbol{s} - \xi \nabla \mathcal{L}_{\mu}(\boldsymbol{s}, \boldsymbol{\lambda})\big)$
  until $\|\boldsymbol{s} - \Pi\big(\boldsymbol{s} - \xi \nabla \mathcal{L}_{\mu}(\boldsymbol{s}, \boldsymbol{\lambda})\big)\|_{\infty} \leq \omega$
  if $\max_{i=1,\ldots,M} \big|\max\big\{q_i(\boldsymbol{s}), -\lambda_i/\mu\big\}\big| \leq \eta$ **then**
    $\lambda_i = \big(\lambda_i + \mu q_i(\boldsymbol{s})\big)^{+}$, for $i = 1, \ldots, M$,
    $\eta = \max\{\eta^{\bigstar}, \eta/(1 + \mu^{0.5})\}$
  else
    $\mu = 10\mu$
    $\eta = \max\{\eta^{\bigstar}, 0.1/(1 + \mu^{0.1})\}$
  end if
until $\max_{i=1,\ldots,M} \max\big|\big\{g_i(\boldsymbol{s}), -\lambda_i/\mu\big\}\big| \leq \eta^{\bigstar}$ and
$\|\boldsymbol{s} - \xi\Pi\big(\boldsymbol{s} - \nabla \mathcal{L}_{\mu}(\boldsymbol{s}, \boldsymbol{\lambda})\big)\|_{\infty} \leq \omega^{\bigstar}$
return $\boldsymbol{s}$

In summary, the augmented Lagrangian method proceeds as follows [106]. Given the multipliers $\boldsymbol{\lambda}^{(k)}$ and the penalty $\mu^{(k)}$ at epoch k, Problem (A.8) is approximately solved, thereby obtaining $\boldsymbol{s}^{(k)}$. Then, the multipliers are updated as

$$\lambda_i^{(k+1)} = \Big(\lambda_i^{(k)} + \mu^{(k)} q_i\big(\boldsymbol{s}^{(k)}\big)\Big)^{+}, \quad i = 1, \ldots, M, \tag{A.14}$$

a new penalty parameter $\mu^{(k+1)} \geq \mu^{(k)}$ is chosen, and the process is repeated. Alg. 1 summarizes the procedure.

Appendix B

Derivation of the decoding rule in (4.35)

Let $\boldsymbol{\beta} \in \mathbb{C}^J$, with $J \in \mathcal{J} = \{1, \ldots, L_{\text{tr,u}}\}$ be the vector containing the non-zero entries of the channel taps $\{\beta_{\text{tr},u}(\ell)\}_{\ell=0}^{L_{\text{tr},u}-1}$, and $\{d_j\}_{j=1}^{J}$ be the corresponding indexes, whereby $\beta_{\text{tr},u}(d_j - 1) = \beta_j$, for $j = 1, \ldots, J$. Then, the samples in Eq. (4.23a) can be organized in the matrix $\boldsymbol{Y} \in \mathbb{C}^{M \times J}$, with $[\boldsymbol{Y}]_{p,\ell} = y_{\text{tr},u}(p-1, \ell-1)$, and

$$\boldsymbol{Y} = \boldsymbol{c} \sum_{j=1}^{J} \beta_j \boldsymbol{e}_{d_j}^{\mathsf{T}} + \boldsymbol{Z}, \tag{B.1}$$

where $\boldsymbol{c} = [c_{\text{tr},u}(0) \ \cdots \ c_{\text{tr},u}(M-1)]^{\mathsf{T}} \in \mathcal{C}_{\text{tr}}$ is the codeword sent in $[0, MT]$, $\boldsymbol{e}_i \in \mathbb{R}^J$ is a vector whose entries are all zero, except the i-th one that equals 1, and $\boldsymbol{Z} \in \mathbb{C}^{M \times J}$ is the noise matrix, with $[\boldsymbol{Z}]_{p,\ell} = z_{\text{tr},u}(p-1, \ell-1)$.

The user is faced with the problem of estimating $\boldsymbol{c}$ based on $\boldsymbol{Y}$, when J and $\{(\beta_j, d_j)\}_{j=1}^{J}$ are unknown, and the entries of $\boldsymbol{Z}$ are i.i.d. complex circularly-symmetric Gaussian random variables with variance σ_{com}^2. Next, we use the GIC rule to estimate the number of non-zero channel taps [70]. To proceed, write the log-likelihood under the hypothesis that J entries are

non-zero, namely

$$\mathcal{L}_J\left(\boldsymbol{Y};\boldsymbol{c},\{\beta_j\}_{j=1}^J,\{d_j\}_{j=1}^J\right) = -\frac{1}{\sigma_{\text{com}}^2}\left\|\boldsymbol{Y}-\boldsymbol{c}\sum_{j=1}^J\beta_j\boldsymbol{e}_{d_j}^{\mathsf{T}}\right\|_F^2 - MJ\ln(\pi\sigma_{\text{com}}^2). \tag{B.2}$$

Under this hypothesis, the ML estimators of the codeword and of the tap amplitudes and indexes, $\hat{\boldsymbol{c}}$ and $\{(\hat{\beta}_j,\hat{d}_j)\}_{j=1}^J$, respectively, are found by solving

$$\max_{\substack{\boldsymbol{c}\in\mathcal{C}_{\text{tr}},\{\beta_j\}_{j=1}^J\in\mathbb{C},\\ \{d_j\}_{j=1}^J\in\mathcal{J}}}\mathcal{L}_J\left(\boldsymbol{Y};\boldsymbol{c},\{\beta_j\}_{j=1}^J,\{d_j\}_{j=1}^J\right). \tag{B.3}$$

Then, the number of non-zero entries, say $\hat{J}$, is obtained with a GIC rule, i.e., by solving

$$\min_{J\in\mathcal{J}}\left\{J\eta'_{\text{com}}-\mathcal{L}_J\left(\boldsymbol{Y};\hat{\boldsymbol{c}},\{\hat{\beta}_j\}_{j=1}^J,\{\hat{d}_j\}_{j=1}^J\right)\right\}, \tag{B.4}$$

where η'_{com} is a penalty factor. Finally, the codeword is decoded by taking the ML estimator $\hat{\boldsymbol{c}}$ when $J=\hat{J}$.

Combining (B.3) and (B.4), the GIC rule is

$$\min_{J\in\mathcal{J}}\left\{J\eta'_{\text{com}}-\max_{\substack{\boldsymbol{c}\in\mathcal{C}_{\text{tr}},\{\beta_j\}_{j=1}^J\in\mathbb{C},\\ \{d_j\}_{j=1}^J\in\mathcal{J}}}\mathcal{L}_J\left(\boldsymbol{Y};\boldsymbol{c},\{\beta_j\}_{j=1}^J,\{d_j\}_{j=1}^J\right)\right\}, \tag{B.5}$$

which is equivalent to

$$\max_{J\in\mathcal{J}}\max_{\substack{\boldsymbol{c}\in\mathcal{C}_{\text{tr}},\{\beta_j\}_{j=1}^J\in\mathbb{C},\\ \{d_j\}_{j=1}^J\in\mathcal{J}}}\left\{\mathcal{L}_J\left(\boldsymbol{Y};\boldsymbol{c},\{\beta_j\}_{j=1}^J,\{d_j\}_{j=1}^J\right)-J\eta'_{\text{com}}\right\}. \tag{B.6}$$

Since the maximization in (B.3) is equivalent to the inner maximization in (B.6), the optimum $\boldsymbol{c}$ obtained by solving (B.6) is also equal to the ML estimator $\hat{\boldsymbol{c}}$ when $J=\hat{J}$, i.e., to the decoded codeword. We, therefore, proceed by solving Problem (B.6). Upon denoting $\eta_{\text{com}}=\sigma_{\text{com}}^2\eta'_{\text{com}}$, Problem (B.6)

is equivalent to

$$\max_{\boldsymbol{c}\in\mathcal{C}_{\text{tr}}}\max_{J\in\mathcal{J}}\max_{\substack{\{\beta_j\}_{j=1}^J\in\mathbb{C},\\ \{d_j\}_{j=1}^J\in\mathcal{J}}}\left\{-\left\|\boldsymbol{Y}-\boldsymbol{c}\sum_{j=1}^{J}\beta_j\boldsymbol{e}_{d_j}^{\mathsf{T}}\right\|_F^2-J\eta_{\text{com}}\right\}. \tag{B.7}$$

Let us start by tackling the minimization over $\{\beta_j\}_{j=1}^J$, and let $\boldsymbol{A}_j=\boldsymbol{c}\boldsymbol{e}_{d_j}^{\mathsf{T}}$, $j=1,\ldots,J$. Then, conditions for the minimum over $\{\beta_j\}_{j=1}^J$ are

$$\begin{aligned}0&=\frac{\partial}{\partial\beta_j}\left\{-\left\|\boldsymbol{Y}-\sum_{i=1,i\neq j}^{J}\alpha_i\boldsymbol{A}_i-\beta_j\boldsymbol{A}_j\right\|_F^2-J\eta_{\text{com}}\right\}\\&=2\,\text{Tr}\left(\left(\boldsymbol{Y}-\sum_{i=1,i\neq j}^{J}\alpha_i\boldsymbol{A}_i\right)\boldsymbol{A}_j^{\mathsf{H}}\right)-2\beta_j\,\text{Tr}(\boldsymbol{A}_j\boldsymbol{A}_j^{\mathsf{H}})\\&=2\boldsymbol{c}^{\mathsf{H}}\boldsymbol{Y}\boldsymbol{e}_{d_j}-2\|\boldsymbol{c}\|^2\beta_j,\quad j=1,\ldots,J,\end{aligned} \tag{B.8}$$

where the last equality follows from the fact that $\text{Tr}(\boldsymbol{A}_i\boldsymbol{A}_j^{\mathsf{H}})=\|\boldsymbol{c}\|^2$, if $i=j$, and zero, otherwise. Therefore

$$\beta_j=\frac{\boldsymbol{c}^{\mathsf{H}}\boldsymbol{Y}\boldsymbol{e}_{d_j}}{\|\boldsymbol{c}\|^2},\quad j=1,\ldots,J, \tag{B.9}$$

and Problem (B.7) becomes

$$\max_{\boldsymbol{c}\in\mathcal{C}_{\text{tr}}}\max_{J\in\mathcal{J}}\max_{\{d_j\}_{j=1}^J\in\mathcal{J}}\left\{-\left\|\boldsymbol{Y}-\frac{\boldsymbol{c}\boldsymbol{c}^{\mathsf{H}}}{\|\boldsymbol{c}\|^2}\boldsymbol{Y}\sum_{j=1}^{J}\boldsymbol{e}_{d_j}\boldsymbol{e}_{d_j}^{\mathsf{T}}\right\|_F^2-J\eta_{\text{com}}\right\}. \tag{B.10}$$

Notice now that $\boldsymbol{E}=\sum_{j=1}^J\boldsymbol{e}_{d_j}\boldsymbol{e}_{d_j}\in\mathbb{R}^{J\times J}$ appearing in (B.10) is a square matrix whose entries are all zero, except those in positions $\{(d_j,d_j)\}_{j=1}^J$ that

equals 1. Then, the Frobenius norm in (B.10) can also be written as

$$\begin{aligned}\left\|\boldsymbol{Y}-\frac{\boldsymbol{c}\boldsymbol{c}^{\mathsf{H}}}{\|\boldsymbol{c}\|^2}\boldsymbol{Y}\boldsymbol{E}\right\|_F^2 &= \mathrm{Tr}(\boldsymbol{Y}\boldsymbol{Y}^{\mathsf{H}}) - \frac{2}{\|\boldsymbol{c}\|^2}\Re\left(\mathrm{Tr}\left(\boldsymbol{Y}\boldsymbol{E}\boldsymbol{Y}^{\mathsf{H}}\boldsymbol{c}\boldsymbol{c}^{\mathsf{H}}\right)\right) \\ &\quad + \frac{1}{\|\boldsymbol{c}\|^4}\mathrm{Tr}(\boldsymbol{c}\boldsymbol{c}^{\mathsf{H}}\boldsymbol{Y}\boldsymbol{E}\boldsymbol{E}\boldsymbol{Y}^{\mathsf{H}}\boldsymbol{c}\boldsymbol{c}^{\mathsf{H}}) \\ &= \mathrm{Tr}(\boldsymbol{Y}\boldsymbol{Y}^{\mathsf{H}}) - \frac{\boldsymbol{c}^{\mathsf{H}}\boldsymbol{Y}\boldsymbol{E}\boldsymbol{Y}^{\mathsf{H}}\boldsymbol{c}}{\|\boldsymbol{c}\|^2} \\ &= \mathrm{Tr}(\boldsymbol{Y}\boldsymbol{Y}^{\mathsf{H}}) - \frac{\|\boldsymbol{c}^{\mathsf{H}}\boldsymbol{Y}\boldsymbol{E}\|^2}{\|\boldsymbol{c}\|^2} \\ &= \mathrm{Tr}(\boldsymbol{Y}\boldsymbol{Y}^{\mathsf{H}}) - \sum_{\ell\in\{d_j\}_{j=1}^{J}} \frac{\left|(\boldsymbol{c}^{\mathsf{H}}\boldsymbol{Y})_\ell\right|^2}{\|\boldsymbol{c}\|^2} \\ &= \mathrm{Tr}(\boldsymbol{Y}\boldsymbol{Y}^{\mathsf{H}}) - \sum_{\ell\in\{d_j\}_{j=1}^{J}} T_{\mathrm{tr}}(\boldsymbol{c},\ell-1), \end{aligned} \tag{B.11}$$

whereby Problem (B.10) is equivalent to

$$\max_{\boldsymbol{c}\in\mathcal{C}_{\mathrm{tr}}}\max_{J\in\mathcal{J}}\max_{\{d_j\}_{j=1}^{J}\in\mathcal{J}}\left\{\sum_{\ell\in\{d_j\}_{j=1}^{J}} T_{\mathrm{tr}}(\boldsymbol{c},\ell-1) - J\eta_{\mathrm{com}}\right\}. \tag{B.12}$$

The maximization over $\{d_j\}_{j=1}^{J}$ amounts to taking the J indexes with largest statistic. If some prior information is available regarding the potential support of the non-zero channel taps (e.g., expected delay range or previously learned support), the estimation of their number can be simplified by restricting the candidate positions in the maximization. This may lead to a reduction in complexity and more reliable model selection under the GIC rule. If we compute the order statistics $\{T_{\mathrm{tr}}^{\mathrm{sort}}(\boldsymbol{c},\ell)\}_{\ell=0}^{L_{\mathrm{tr},u}-1}$ by sorting $\{T_{\mathrm{tr}}(\boldsymbol{c},\ell)\}_{\ell=0}^{L_{\mathrm{tr},u}-1}$ in decreasing order, Problem (B.12) reduces to

$$\begin{aligned}&\max_{\boldsymbol{c}\in\mathcal{C}_{\mathrm{tr}}}\max_{J\in\mathcal{J}}\left\{\sum_{\ell=0}^{J-1} T_{\mathrm{tr}}^{\mathrm{sort}}(\boldsymbol{c},\ell) - J\eta_{\mathrm{com}}\right\} \\ &= \max_{\boldsymbol{c}\in\mathcal{C}_{\mathrm{tr}}}\left\{T_{\mathrm{tr}}^{\mathrm{sort}}(\boldsymbol{c},0) - \eta_{\mathrm{com}} + \sum_{\ell=1}^{L_{\mathrm{tr},u}-1}\left(T_{\mathrm{tr}}^{\mathrm{sort}}(\boldsymbol{c},\ell) - \eta_{\mathrm{com}}\right)^+\right\}. \end{aligned} \tag{B.13}$$

which is equivalent to (4.35).

Bibliography

[1] T. Huang, W. Yang, J. Wu, J. Ma, X. Zhang, and D. Zhang, "A survey on green 6G network: Architecture and technologies," *IEEE Access*, vol. 7, pp. 175 758–175 768, 2019. DOI: 10.1109/ACCESS.2019.2957648.

[2] B. Rong, "6G: The next horizon: From connected people and things to connected intelligence," *IEEE Wireless Communications*, vol. 28, no. 5, pp. 8–8, 2021. DOI: 10.1109/MWC.2021.9615100.

[3] M. Latva-aho and K. Leppänen, *Key drivers and research challenges for 6G ubiquitous wireless intelligence*, https://www.6gflagship.com/white-papers/, 2023.

[4] W. Saad, M. Bennis, and M. Chen, "A vision of 6G wireless systems: Applications, trends, technologies, and open research problems," *IEEE Network*, vol. 34, no. 3, pp. 134–142, 2020. DOI: 10.1109/MNET.001.1900287.

[5] F. Tariq, M. R. A. Khandaker, K.-K. Wong, M. A. Imran, M. Bennis, and M. Debbah, "A speculative study on 6G," *IEEE Wireless Communications*, vol. 27, no. 4, pp. 118–125, 2020. DOI: 10.1109/MWC.001.1900488.

[6] Q. Wu and R. Zhang, "Towards smart and reconfigurable environment: Intelligent reflecting surface aided wireless network," *IEEE Communications Magazine*, vol. 58, no. 1, pp. 106–112, 2020. DOI: 10.1109/MCOM.001.1900107.

[7] M. Di Renzo et al., "Smart radio environments empowered by reconfigurable intelligent surfaces: How it works, state of research, and the road ahead," *IEEE Journal on Selected Areas in Communications*, vol. 38, no. 11, pp. 2450–2525, 2020. DOI: 10.1109/JSAC.2020.3007211.

[8] C. L. Holloway, E. F. Kuester, J. A. Gordon, J. O'Hara, J. Booth, and D. R. Smith, "An overview of the theory and applications of metasurfaces: The two-dimensional equivalents of metamaterials," *IEEE Antennas and Propagation Magazine*, vol. 54, no. 2, pp. 10–35, 2012. DOI: 10.1109/MAP.2012.6230714.

[9] C. Huang et al., "Holographic MIMO surfaces for 6G wireless networks: Opportunities, challenges, and trends," *IEEE Wireless Communications*, vol. 27, no. 5, pp. 118–125, 2020. DOI: 10.1109/MWC.001.1900534.

[10] W. Tang et al., "Wireless communications with reconfigurable intelligent surface: Path loss modeling and experimental measurement," *IEEE Transactions on Wireless Communications*, vol. 20, no. 1, pp. 421–439, 2021. DOI: 10.1109/TWC.2020.3024887.

[11] M. Dajer et al., *Reconfigurable intelligent surface: Design the channel – a new opportunity for future wireless networks*, 2020. arXiv: 2010.07408 [eess.SP]. [Online]. Available: https://arxiv.org/abs/2010.07408.

[12] Z. Zhang et al., "Active RIS vs. passive RIS: Which will prevail in 6G?" *IEEE Transactions on Communications*, vol. 71, no. 3, pp. 1707–1725, Mar. 2023.

[13] Y. Liu et al., "STAR: Simultaneous transmission and reflection for 360° coverage by intelligent surfaces," *IEEE Wireless Communications*, vol. 28, no. 6, pp. 102–109, 2021. DOI: 10.1109/MWC.001.2100191.

[14] S. Basharat, M. Khan, M. Iqbal, U. Hashmi, S. A. R. Zaidi, and I. Robertson, "Exploring reconfigurable intelligent surfaces for 6G: State-of-the-art and the road ahead," *IET Communications*, vol. 16, Jun. 2022. DOI: 10.1049/cmu2.12364.

[15] S. Li, B. Duo, X. Yuan, Y.-C. Liang, and M. Di Renzo, "Reconfigurable intelligent surface assisted UAV communication: Joint trajectory design and passive beamforming," *IEEE Wireless Communications Letters*, vol. 9, no. 5, pp. 716–720, 2020. DOI: 10.1109/LWC.2020.2966705.

[16] G. Singh, A. Srivastava, and V. A. Bohara, "Visible light and reconfigurable intelligent surfaces for beyond 5G V2X communication

networks at road intersections," *IEEE Transactions on Vehicular Technology*, vol. 71, no. 8, pp. 8137–8151, 2022. DOI: 10.1109/TVT.2022.3174131.

[17] Y. Cui, F. Liu, X. Jing, and J. Mu, "Integrating sensing and communications for ubiquitous IoT: Applications, trends, and challenges," *IEEE Network*, vol. 35, no. 5, pp. 158–167, 2021. DOI: 10.1109/MNET.010.2100152.

[18] R. Chen, M. Liu, Y. Hui, N. Cheng, and J. Li, "Reconfigurable intelligent surfaces for 6G IoT wireless positioning: A contemporary survey," *IEEE Internet of Things Journal*, vol. 9, no. 23, pp. 23 570–23 582, 2022. DOI: 10.1109/JIOT.2022.3203890.

[19] Z. Tang, T. Hou, Y. Liu, J. Zhang, and C. Zhong, "A novel design of RIS for enhancing the physical layer security for RIS-Aided NOMA networks," *IEEE Wireless Communications Letters*, vol. 10, no. 11, pp. 2398–2401, 2021. DOI: 10.1109/LWC.2021.3101806.

[20] L. Zhang et al., "Space-time-coding digital metasurfaces," *Nature Communications*, vol. 9, no. 2041-1723, 2018. DOI: 10.1038/s41467-018-06802-0.

[21] M. Mizmizi, D. Tagliaferri, and U. Spagnolini, "Wireless communications with space–time modulated metasurfaces," *IEEE Journal on Selected Areas in Communications*, vol. 42, no. 6, pp. 1534–1548, 2024. DOI: 10.1109/JSAC.2024.3389124.

[22] L. Zhang, M. Rossi, X. Q. Chen, G. Castaldi, T. J. Cui, and V. Galdi, "Some emerging concepts in the design of space-time-coding digital metasurfaces," in *2024 Eighteenth International Congress on Artificial Materials for Novel Wave Phenomena (Metamaterials)*, 2024, pp. 1–3. DOI: 10.1109/Metamaterials62190.2024.10703321.

[23] H. Wymeersch, J. He, B. Denis, A. Clemente, and M. Juntti, "Radio localization and mapping with reconfigurable intelligent surfaces: Challenges, opportunities, and research directions," *IEEE Vehicular Technology Magazine*, vol. 15, no. 4, pp. 52–61, Oct. 2020. DOI: 10.1109/MVT.2020.3023682.

[24] J. He, H. Wymeersch, L. Kong, O. Silvén, and M. Juntti, "Large intelligent surface for positioning in millimeter wave MIMO systems," in *2020 IEEE 91st Vehicular Technology Conference (VTC2020-Spring)*, 2020, pp. 1–5. DOI: 10.1109/VTC2020-Spring48590.2020.9129075.

[25] A. Elzanaty, A. Guerra, F. Guidi, and M.-S. Alouini, "Reconfigurable intelligent surfaces for localization: Position and orientation error bounds," *IEEE Transactions on Signal Processing*, vol. 69, pp. 5386–5402, 2021. DOI: 10.1109/TSP.2021.3101644.

[26] F. Liu et al., "Integrated sensing and communications: Toward dual-functional wireless networks for 6G and beyond," *IEEE Journal on Selected Areas in Communications*, vol. 40, no. 6, pp. 1728–1767, 2022. DOI: 10.1109/JSAC.2022.3156632.

[27] J. A. Zhang et al., "Enabling joint communication and radar sensing in mobile networks—a survey," *IEEE Communications Surveys & Tutorials*, vol. 24, no. 1, pp. 306–345, 2022. DOI: 10.1109/COMST.2021.3122519.

[28] E. Grossi, H. Taremizadeh, and L. Venturino, "Radar target detection and localization aided by an active reconfigurable intelligent surface," *IEEE Signal Processing Letters*, vol. 30, pp. 903–907, 2023, ISSN: 1558-2361. DOI: 10.1109/LSP.2023.3296372.

[29] J. Huang and J. A. Encinar, *Reflectarray antennas*. John Wiley & Sons, 2007.

[30] S. V. Hum and J. Perruisseau-Carrier, "Reconfigurable reflectarrays and array lenses for dynamic antenna beam control: A review," *IEEE Transactions on Antennas and Propagation*, vol. 62, no. 1, pp. 183–198, Jan. 2014.

[31] P. Nayeri, F. Yang, and A. Z. Elsherbeni, "Beam-scanning reflectarray antennas: A technical overview and state of the art.," *IEEE Antennas and Propagation Magazine*, vol. 57, no. 4, pp. 32–47, 2015.

[32] Q. He, S. Sun, and L. Zhou, "Tunable/reconfigurable metasurfaces: Physics and applications," *Research*, 2019.

[33] O. Tsilipakos et al., "Toward intelligent metasurfaces: The progress from globally tunable metasurfaces to software-defined metasurfaces with an embedded network of controllers," *Advanced optical materials*, vol. 8, no. 17, p. 2 000 783, 2020.

[34] R. Long, Y.-C. Liang, Y. Pei, and E. G. Larsson, "Active reconfigurable intelligent surface-aided wireless communications," *IEEE Transactions on Wireless Communications*, vol. 20, no. 8, pp. 4962–4975, Aug. 2021, ISSN: 1558-2248. DOI: 10.1109/TWC.2021.3064024.

[35] K. Liu, Z. Zhang, L. Dai, S. Xu, and F. Yang, "Active reconfigurable intelligent surface: Fully-connected or sub-connected?" *IEEE Communications Letters*, vol. 26, no. 1, pp. 167–171, Jan. 2022, ISSN: 1558-2558. DOI: 10.1109/LCOMM.2021.3119696.

[36] Y. Liu et al., "Reconfigurable intelligent surfaces: Principles and opportunities," *IEEE Communications Surveys & Tutorials*, vol. 2, no. 3, pp. 1546–1577, 2021.

[37] E. Björnson, H. Wymeersch, B. Matthiesen, P. Popovski, L. Sanguinetti, and E. de Carvalho, "Reconfigurable intelligent surfaces: A signal processing perspective with wireless applications," *IEEE Signal Processing Magazine*, vol. 39, no. 2, pp. 135–158, 2022. DOI: 10.1109/MSP.2021.3130549.

[38] Q. Wu and R. Zhang, "Joint active and passive beamforming optimization for intelligent reflecting surface assisted SWIPT under QoS constraints," *IEEE Journal on Selected Areas in Communications*, vol. 38, no. 8, pp. 1735–1748, 2020. DOI: 10.1109/JSAC.2020.3000807.

[39] C. Pan et al., "Intelligent reflecting surface aided MIMO broadcasting for simultaneous wireless information and power transfer," *IEEE Journal on Selected Areas in Communications*, vol. 38, no. 8, pp. 1719–1734, 2020. DOI: 10.1109/JSAC.2020.3000802.

[40] C. Pan et al., "Multicell MIMO communications relying on intelligent reflecting surfaces," *IEEE Transactions on Wireless Communications*, vol. 19, no. 8, pp. 5218–5233, 2020. DOI: 10.1109/TWC.2020.2990766.

[41] W. Tang et al., "MIMO transmission through reconfigurable intelligent surface: System design, analysis, and implementation," *IEEE Journal on Selected Areas in Communications*, vol. 38, no. 11, pp. 2683–2699, Nov. 2020, ISSN: 1558-0008. DOI: 10.1109/JSAC.2020.3007055.

[42] Y.-C. Liang, Q. Zhang, J. Wang, R. Long, H. Zhou, and G. Yang, "Backscatter communication assisted by reconfigurable intelligent surfaces," *Proceedings of the IEEE*, vol. 110, no. 9, pp. 1339–1357, 2022. DOI: 10.1109/JPROC.2022.3169622.

[43] S. Buzzi, E. Grossi, M. Lops, and L. Venturino, "Radar target detection aided by reconfigurable intelligent surfaces," *IEEE Signal Processing Letters*, vol. 28, pp. 1315–1319, 2021, ISSN: 1558-2361. DOI: 10.1109/LSP.2021.3089085.

[44] A. Aubry, A. De Maio, and M. Rosamilia, "Reconfigurable intelligent surfaces for N-LOS radar surveillance," *IEEE Transactions on Vehicular Technology*, vol. 70, no. 10, pp. 10 735–10 749, Oct. 2021, ISSN: 1939-9359. DOI: 10.1109/TVT.2021.3102315.

[45] S. Buzzi, E. Grossi, M. Lops, and L. Venturino, "Foundations of MIMO radar detection aided by reconfigurable intelligent surfaces," *IEEE Transactions on Signal Processing*, vol. 70, pp. 1749–1763, 2022. DOI: 10.1109/TSP.2022.3157975.

[46] H. Zhang, H. Zhang, B. Di, K. Bian, Z. Han, and L. Song, "MetaRadar: Multi-target detection for reconfigurable intelligent surface aided radar systems," *IEEE Transactions on Wireless Communications*, vol. 21, no. 9, pp. 6994–7010, Sep. 2022, ISSN: 1558-2248. DOI: 10.1109/TWC.2022.3153792.

[47] M. Rihan, E. Grossi, L. Venturino, and S. Buzzi, "Spatial diversity in radar detection via active reconfigurable intelligent surfaces," *IEEE Signal Processing Letters*, vol. 29, pp. 1242–1246, 2022.

[48] J. Lee, J. Lee, and K. Yang, "Reflection-type RTD low-power amplifier with deep sub-mw DC power consumption," *IEEE Microwave and Wireless Components Letters*, vol. 24, no. 8, pp. 551–553, Aug. 2014.

[49] J. Lee and K. Yang, "RF power analysis on 5.8 GHz low-power amplifier using resonant tunneling diodes," *IEEE Microwave and Wireless Components Letters*, vol. 27, no. 1, pp. 61–63, Jan. 2017.

[50] F. Amato, C. W. Peterson, B. P. Degnan, and G. D. Durgin, "Tunneling RFID tags for long-range and low-power microwave applications," *IEEE Journal of Radio Frequency Identification*, vol. 2, no. 2, pp. 93–103, Jun. 2018.

[51] J. Rao, Y. Zhang, S. Tang, Z. Li, C.-Y. Chiu, and R. Murch, "An active reconfigurable intelligent surface utilizing phase-reconfigurable reflection amplifiers," *IEEE Transactions on Microwave Theory and Techniques*, 2023.

[52] M. Iwamura, H. Takahashi, and S. Nagata, "Relay technology in LTE-advanced," *NTT DOCOMO Techical Journal*, vol. 12, no. 2, pp. 29–36, 2022.

[53] H. Guo et al., "A comparison between network-controlled repeaters and reconfigurable intelligent surfaces," 2022. arXiv: 2211.06974 [cs.NI].

[54] G. Leone, E. Moro, I. Filippini, A. Capone, and D. De Donno, "Towards reliable mmWave 6G RAN: Reconfigurable surfaces, smart repeaters, or both?" In *2022 20th International Symposium on Modeling and Optimization in Mobile, Ad hoc, and Wireless Networks (WiOpt)*, Sep. 2022, pp. 81–88.

[55] R. A. Ayoubi, M. Mizmizi, D. Tagliaferri, D. De Donno, and U. Spagnolini, "Network-controlled repeaters vs. reconfigurable intelligent surfaces for 6G mmW Coverage Extension: A simulative comparison," in *2023 21st Mediterranean Communication and Computer Networking Conference*, 2023, pp. 196–202. DOI: 10.1109/MedComNet58619.2023.10168854.

[56] H. L. Van Trees, *Detection, Estimation, and Modulation Theory, Part IV: Optimum Array Processing*. New York, NY, USA: John Wiley & Sons, 2002.

[57] M. A. Richards, *Fundamentals of radar signal processing*, 2nd ed. New York, NY, USA: McGraw-Hill, 2005.

[58] M. I. Skolnik, *Introduction to radar systems*, 3rd ed. New York, NY, USA: McGraw-Hill Higher Education, 2015.

[59] J. Joung, C. K. Ho, K. Adachi, and S. Sun, "A survey on power-amplifier-centric techniques for spectrum- and energy-efficient wireless communications," *IEEE Communications Surveys & Tutorials*, vol. 17, no. 1, pp. 315–333, 2015.

[60] Z. Zhang et al., "Active RIS vs. passive RIS: Which will prevail in 6G?" *IEEE Transactions on Communications*, vol. 71, no. 3, pp. 1707–1725, 2023. DOI: 10.1109/TCOMM.2022.3231893.

[61] H. L. Van Trees, *Detection, Estimation, and Modulation Theory, Part I: Detection, Estimation, and Linear Modulation Theory*. New York, NY, USA: John Wiley & Sons, 2001.

[62] E. Grossi, M. Lops, A. M. Tulino, and L. Venturino, "Opportunistic sensing using mmWave communication signals: A subspace approach," *IEEE Transactions on Wireless Communications*, vol. 20, no. 7, pp. 4420–4434, Jul. 2021.

[63] E. Grossi, H. Taremizadeh, and L. Venturino, "STAR-RIS-based pulse-Doppler radars," in *Proc. of the 32nd European Signal Processing Conference*, Lyon, France, Aug. 2024. [Online]. Available: https://arxiv.org/pdf/2406.11321.

[64] M. Di Renzo et al., "Reconfigurable intelligent surfaces vs. relaying: Differences, similarities, and performance comparison," *IEEE Open Journal of the Communications Society*, vol. 1, pp. 798–807, 2020. DOI: 10.1109/OJCOMS.2020.3002955.

[65] M. Ahmed et al., "A survey on STAR-RIS: Use cases, recent advances, and future research challenges," *IEEE Internet of Things Journal*, vol. 10, no. 16, pp. 14 689–14 711, Aug. 2023, ISSN: 2327-4662. DOI: 10.1109/JIOT.2023.3279357.

[66] X. Mu, Y. Liu, L. Guo, J. Lin, and R. Schober, "Intelligent reflecting surface enhanced indoor robot path planning: A radio map-based approach," *IEEE Transactions on Wireless Communications*, vol. 20, no. 7, pp. 4732–4747, 2021. DOI: 10.1109/TWC.2021.3062089.

[67] S. Buzzi, E. Grossi, M. Lops, and L. Venturino, "Radar target detection aided by reconfigurable intelligent surfaces," *IEEE Signal Processing Letters*, vol. 28, pp. 1315–1319, 2021. DOI: 10.1109/LSP.2021.3089085.

[68] J. Xu, Y. Liu, X. Mu, and O. A. Dobre, "STAR-RISs: Simultaneous transmitting and reflecting reconfigurable intelligent surfaces," *IEEE Communications Letters*, vol. 25, no. 9, pp. 3134–3138, 2021. DOI: 10.1109/LCOMM.2021.3082214.

[69] X. Mu, Y. Liu, L. Guo, J. Lin, and R. Schober, "Simultaneously transmitting and reflecting (STAR) RIS aided wireless communications," *IEEE Transactions on Wireless Communications*, vol. 21, no. 5, pp. 3083–3098, May 2022, ISSN: 1558-2248. DOI: 10.1109/TWC.2021.3118225.

[70] P. Stoica and Y. Selen, "Model-order selection: A review of information criterion rules," *IEEE Signal Processing Magazine*, vol. 21, no. 4, pp. 36–47, Jul. 2004, ISSN: 1558-0792. DOI: 10.1109/MSP.2004.1311138.

[71] Z. Zhang, Y. Liu, Z. Wang, and J. Chen, "STARS-ISAC: How many sensors do we need?" *IEEE Transactions on Wireless Communications*, vol. 23, no. 2, pp. 1085–1099, 2024. DOI: 10.1109/TWC.2023.3285795.

[72] G. C. Alexandropoulos, N. Shlezinger, I. Alamzadeh, M. F. Imani, H. Zhang, and Y. C. Eldar, "Hybrid reconfigurable intelligent metasurfaces: Enabling simultaneous tunable reflections and sensing for 6G wireless communications," *IEEE Vehicular Technology Magazine*, 2023, ISSN: 1556-6080. DOI: 10.1109/MVT.2023.3332580.

[73] Q. Li, M. Wen, and M. Di Renzo, "Single-RF MIMO: from spatial modulation to metasurface-based modulation," *IEEE Wireless Communications*, vol. 28, no. 4, pp. 88–95, Aug. 2021, ISSN: 1558-0687. DOI: 10.1109/MWC.021.2000376.

[74] C. T. Capraro, G. T. Capraro, A. De Maio, A. Farina, and M. Wicks, "Demonstration of knowledge aided STAP using measured airborne data," in *2006 International Waveform Diversity & Design Conference*, Jan. 2006. DOI: 10.1109/WDD.2006.8321442.

[75] J. Guerci and E. Baranoski, "Knowledge-aided adaptive radar at DARPA: An overview," *IEEE Signal Processing Magazine*, vol. 23, no. 1, pp. 41–50, Jan. 2006, ISSN: 1558-0792. DOI: 10.1109/MSP.2006.1593336.

[76] P. Stoica, P. Babu, and J. Li, "New method of sparse parameter estimation in separable models and its use for spectral analysis of irregularly sampled data," *IEEE Transactions on Signal Processing*, vol. 59, no. 1, pp. 35–47, Jan. 2011, ISSN: 1941-0476. DOI: 10.1109/TSP.2010.2086452.

[77] X. Zhu, J. Li, and P. Stoica, "Knowledge-aided space-time adaptive processing," *IEEE Transactions on Aerospace and Electronic Systems*, vol. 47, no. 2, pp. 1325–1336, Apr. 2011, ISSN: 1557-9603. DOI: 10.1109/TAES.2011.5751261.

[78] E. Grossi and L. Venturino, "Beampattern design for radars with reconfigurable intelligent surfaces," in *2023 IEEE Radar Conference*, May 2023. DOI: 10.1109/RadarConf2351548.2023.10149631.

[79] H. Taremizadeh, E. Grossi, and L. Venturino, "STAR-RIS transceivers: Integrated sensing and communication with pulsed signals," in *Proc. of the 33nd European Signal Processing Conference*, Isola delle Femmine, Palermo, Italy, Sep. 2025. [Online]. Available: https://arxiv.org/pdf/2507.02346.

[80] H. Taremizadeh, E. Grossi, L. Venturino, and M. Lops, "ISAC STAR-RIS transceivers with space-time coded pulsed signals," *IEEE Open Journal of the Communications Society*, vol. 6, pp. 9569–9586, 2025. DOI: 10.1109/OJCOMS.2025.3632145.

[81] Q. Wu, S. Zhang, B. Zheng, C. You, and R. Zhang, "Intelligent reflecting surface-aided wireless communications: A tutorial," *IEEE Transactions on Communications*, vol. 69, no. 5, pp. 3313–3351, 2021. DOI: 10.1109/TCOMM.2021.3051897.

[82] Y. Liu et al., "Reconfigurable intelligent surfaces: Principles and opportunities," *IEEE Communications Surveys & Tutorials*, vol. 23, no. 3, pp. 1546–1577, 2021. DOI: 10.1109/COMST.2021.3077737.

[83] C. Pan et al., "Reconfigurable intelligent surfaces for 6G systems: Principles, applications, and research directions," *IEEE Communications Magazine*, vol. 59, no. 6, pp. 14–20, 2021. DOI: 10.1109/MCOM.001.2001076.

[84] V. Jamali, A. M. Tulino, G. Fischer, R. R. Müller, and R. Schober, "Intelligent Surface-Aided transmitter architectures for Millimeter-Wave ultra massive MIMO systems," *IEEE Open Journal of the Communications Society*, vol. 2, pp. 144–167, 2021. DOI: 10.1109/OJCOMS.2020.3048063.

[85] C. D'Elia, E. Grossi, and L. Venturino, "Beampattern design for transmit architectures based on reconfigurable intelligent surfaces," *IEEE Transactions on Vehicular Technology*, 2025, ISSN: 1939-9359. [Online]. Available: https://arxiv.org/pdf/2306.15297.

[86] M. Di Renzo et al., "Smart radio environments empowered by reconfigurable intelligent surfaces: How it works, state of research, and the road ahead," *IEEE Journal on Selected Areas in Communications*, vol. 38, no. 11, pp. 2450–2525, 2020. DOI: 10.1109/JSAC.2020.3007211.

[87] K. Zhi, C. Pan, H. Ren, K. K. Chai, and M. Elkashlan, "Active RIS versus passive RIS: Which is superior with the same power budget?" *IEEE Communications Letters*, vol. 26, no. 5, pp. 1150–1154, 2022. DOI: 10.1109/LCOMM.2022.3159525.

[88] P. Saikia, A. Jee, K. Singh, W.-J. Huang, A.-A. A. Boulogeorgos, and T. A. Tsiftsis, "Hybrid-RIS empowered UAV-Assisted ISAC systems: Transfer learning-basedDRL," *IEEE Transactions on Communications*, pp. 1–1, 2025. DOI: 10.1109/TCOMM.2025.3548797.

[89] J. Xu, Y. Liu, X. Mu, R. Schober, and H. V. Poor, "STAR-RISs: a correlated T&R phase-shift model and practical phase-shift configuration strategies," *IEEE Journal of Selected Topics in Signal Processing*, vol. 16, no. 5, pp. 1097–1111, Aug. 2022, ISSN: 1941-0484. DOI: 10.1109/JSTSP.2022.3175030.

[90] M. Ahmed et al., "A survey on STAR-RIS: Use cases, recent advances, and future research challenges," *IEEE Internet of Things Journal*, vol. 10, no. 16, pp. 14 689–14 711, 2023. DOI: 10.1109/JIOT.2023.3279357.

[91] J. Xu et al., "Simultaneously transmitting and reflecting intelligent omni-surfaces: Modeling and implementation," *IEEE Vehicular Technology Magazine*, vol. 17, no. 2, pp. 46–54, 2022.

[92] Q. Li, M. El-Hajjar, Y. Sun, I. Hemadeh, A. Shojaeifard, and L. Hanzo, "Energy-efficient reconfigurable holographic surfaces operating in the presence of realistic hardware impairments," *IEEE Transactions on Communications*, vol. 72, no. 8, pp. 5226–5238, 2024.

[93] Q. Li, M. El-Hajjar, Y. Sun, and L. Hanzo, "Performance analysis of reconfigurable holographic surfaces in the near-field scenario of cell-free networks under hardware impairments," *IEEE Transactions on Wireless Communications*, vol. 23, no. 9, pp. 11 972–11 984, 2024.

[94] Q. Li, M. El-Hajjar, C. Xu, J. An, C. Yuen, and L. Hanzo, "Stacked intelligent metasurfaces for holographic MIMO-aided cell-free networks," *IEEE Transactions on Communications*, vol. 72, no. 11, pp. 7139–7151, 2024.

[95] Q. Li, M. El-Hajjar, K. Cao, C. Xu, H. Haas, and L. Hanzo, "Holographic metasurface-based beamforming for multi-altitude leo satellite networks," *IEEE Transactions on Wireless Communications*, vol. 24, no. 4, pp. 3103–3116, 2025.

[96] D. K. Pin Tan et al., "Integrated sensing and communication in 6G: Motivations, use cases, requirements, challenges and future directions," in *2021 1st IEEE International Online Symposium on Joint Communications & Sensing (JC&S)*, 2021, pp. 1–6. DOI: 10.1109/JCS52304.2021.9376324.

[97] A. Magbool, V. Kumar, Q. Wu, M. D. Renzo, and M. F. Flanagan, "A survey on integrated sensing and communication with intelligent metasurfaces: Trends, challenges, and opportunities," *arXiv:2401.15562*, 2024.

[98] S. Zhang, W. Hao, G. Sun, Z. Zhu, X. Li, and Q. Wu, "Joint beamforming design for the STAR-RIS-Enabled ISAC systems with multiple targets and multiple users," *IEEE Transactions on Communications*, vol. 73, no. 1, pp. 693–708, 2025. DOI: 10.1109/TCOMM.2024.3439446.

[99] Z. Liu, X. Li, H. Ji, H. Zhang, and V. C. M. Leung, "Exploiting STAR-RIS for covert communication in ISAC networks under imperfect CSI," *IEEE Transactions on Vehicular Technology*, vol. 74, no. 1, pp. 786–802, 2025. DOI: 10.1109/TVT.2024.3453389.

[100] Y. Wang et al., "Optimizing the fairness of STAR-RIS and NOMA assisted integrated sensing and communication systems," *IEEE Transactions on Wireless Communications*, vol. 23, no. 6, pp. 5895–5907, 2024. DOI: 10.1109/TWC.2023.3328872.

[101] Z. Wang, X. Mu, and Y. Liu, "STARS enabled integrated sensing and communications," *IEEE Transactions on Wireless Communications*, vol. 22, no. 10, pp. 6750–6765, 2023. DOI: 10.1109/TWC.2023.3245297.

[102] P. Saikia, A. Jee, K. Singh, C. Pan, W.-J. Huang, and T. A. Tsiftsis, "RIS-Aided integrated sensing and communication systems: STAR-RIS versus passive RIS?" *IEEE Open Journal of the Communications Society*, vol. 5, pp. 7954–7973, 2024. DOI: 10.1109/OJCOMS.2024.3515933.

[103] J. Zhang et al., "Intelligent waveform design for integrated sensing and communication," *IEEE Wireless Communications*, vol. 32, no. 1, pp. 166–173, 2025. DOI: 10.1109/MWC.003.2400044.

[104] Z. Yigit and E. Basar, "Hybrid STAR-RIS enabled integrated sensing and communication," *IEEE Transactions on Communications*, 2025. DOI: 10.1109/TCOMM.2025.3547800.

[105] D. P. Bertsekas, *Constrained Optimization and Lagrange Multiplier Methods*. Belmont, MA, USA: Athena Scientific, 1996.

[106] J. Nocedal and S. Wright, *Numerical Optimization*, 2nd ed. New York, NY, USA: Springer, 2006.

[107] L. Venturino, E. Grossi, M. Lops, J. Johnston, and X. Wang, "Radar-enabled ambient backscatter communications," *IEEE Transactions on Wireless Communications*, vol. 22, no. 12, pp. 8666–8680, Dec. 2023, ISSN: 1558-2248. DOI: 10.1109/TWC.2023.3264726.

[108] D. Chu, "Polyphase codes with good periodic correlation properties (corresp.)," *IEEE Transactions on Information Theory*, vol. 18, no. 4, pp. 531–532, 1972. DOI: 10.1109/TIT.1972.1054840.

[109] M. M. U. Gul, X. Ma, and S. Lee, "Timing and frequency synchronization for OFDM downlink transmissions using Zadoff-Chu sequences," *IEEE Transactions on Wireless Communications*, vol. 14, no. 3, pp. 1716–1729, 2015. DOI: 10.1109/TWC.2014.2372757.

[110] Y. Lai, L. Venturino, E. Grossi, and W. Yi, "Joint detection and localization in distributed MIMO radars employing waveforms with imperfect auto- and cross-correlation," *IEEE Transactions on Vehicular Technology*, vol. 72, no. 12, pp. 16 524–16 537, Dec. 2023, ISSN: 1939-9359. DOI: 10.1109/TVT.2023.3293023.